E-370

INCLUSIVE PARTICLE PRODUCTION IN

π^+p, K^+p, and pp INTERACTIONS AT 200 GeV/c

by

THOMAS ANSELM JOSEPH FRANK

S. B., Massachusetts Institute of Technology
(1977)

SUBMITTED TO THE DEPARTMENT OF PHYSICS IN PARTIAL
FULFILLMENT OF THE REQUIREMENTS
FOR THE DEGREE OF

DOCTOR OF PHILOSOPHY

at the

MASSACHUSETTS INSTITUTE OF TECHNOLOGY

(February 1985)

Signature of Author Thomas A. Frank
Department of Physics, February 1985

Certified by Richard K. Yamamoto
Richard K. Yamamoto, Thesis Supervisor

Accepted by Sam F. Koster
Chairman, Departmental Committee

INCLUSIVE PARTICLE PRODUCTION IN

π^+p, K^+p, AND pp INTERACTIONS AT 200 GeV/c

by

THOMAS ANSELM JOSEPH FRANK

Submitted to the Department of Physics on 15 February 1985
in partial fulfillment of the requirements of the degree of
Doctor of Philosophy

ABSTRACT

An experiment has been performed in a 200 Gev/c tagged positive beam at the Fermilab Hybrid Spectrometer. A total of 2804 π^+p, 1581 K^+p, and 3384 pp interactions have been reconstructed. The Downstream Particle Identifier has been used to statistically identify particles in the forward hemisphere of multiparticle final states. The quantum number dependence of the strong interaction has been studied in terms of the flavor flow from the initial to the final state.

Thesis Supervisor: Richard K. Yamamoto
Title: Professor of Physics

to my family

Contents

Chapter 1

INTRODUCTION

This work is undertaken as a study in the nature of the constituents and the dynamics in the interactions of hadrons. In this spirit we first comment on the history of such investigations. The remainder of the chapter is devoted to a brief chronicle of the development of apparatus used in the experiment.

1.1 LOW P_T PHYSICS

Since the time of Yukawa[1] small progress has been made in the understanding at a fundamental level of low momentum transfer hadronic interactions. To be certain great achievements have been made. Through the study of hadronic interactions at higher and higher energies a large spectrum of particles emerged. These were ultimately arranged into a periodic table of elementary particles by Gell-Mann[2] and Zweig[3] with the introduction of the quark model for hadronic structure. The color degree of freedom[4] along with the idea of color confinement filled out the quark model and gave it increasing legitimacy in the face of observations.

With the emergence of quantum chromodynamics (QCD) as the candidate theory of the strong interaction attention was turned to the investigation of high Q^2 phenomena. In addition advances were

---

[1] H. Yukawa, Proc. Math. Soc. Japan 17 (1935) 48.

[2] M. Gell-Mann, Phys. Lett. 8 (1964) 214.

[3] G. Zweig, CERN 8182/TH.401 and 8419/TH.412, 1964.

[4] O. W. Greenberg, Phys. Rev. Lett. 13 (1964) 598.

made using weak and electromagnetic probes. Each of these approaches to the study of hadrons sought to avoid or at least minimize the strong coupling of partons. In this way the fundamental structure and dynamics of the hadrons were hoped to become more evident.

As new data became available a surprising similarity was seen to develop between the so called hard and soft processes.[5,6] Although strict lines were drawn between the competing mechanisms the data did seem to indicate the direct participation of hadronic constituents in particle interactions.

In a recent review Fialkowski and Kittel delineate the evidence which seems to connect the quark model with low momentum transfer hadron dynamics. We quote from their report:

> "In the context of quarks and gluons (partons), three observations have recently drawn increased attention to soft hadronic collisions:
>
> 1. Resonance and particle yields in central and fragmentation regions can be understood from quark combinatorics.
>
> 2. Pion production in the nucleon fragmentation region of soft hadron-hadron collisions seems to reflect the valence quark distribution in the nucleon as observed in moderately deep inelastic lepton-nucleon collisions.
>
> 3. Quark fragmentation jets from e^+e^- annihilation and deep inelastic collisions seem to resemble soft hadronic particle production in longitudinal, transverse and multiplicity behavior of the produced hadrons."[7]

The third point above has been the subject of appreciable investigation. In this regard it has been speculated that the true connection between hadronic production in e^+e^-, lN, and hh reactions is due to the domination of this final step of hadronization by the available phase space.[8,9]

At the present time theoretical speculation remains at the level of *ad hoc* models. These models are naturally conceived with the intent of explaining existing data. They typically replace the strong interaction problem with assumptions regarding the precollisional structure of hadrons, the rearrangement of the partons into a final state, and the subsequent transformation of this system into hadrons.

---

[5] W. Ochs, "Hadron Fragmentation at High Energies and Quark Constituents," Nucl. Phys. B118 (1977) 397.

[6] B. Andersson, et. al., "A Quark Parton Model for Hadronic Fragmentation Distributions," Phys. Lett. 71B (1977) 337.

[7] K. Fialkowski and W. Kittel, "Parton Models of Low Momentum Transfer Processes," Univ. of Nijmegen preprint HEN 82-226, published in Rep. on Prog. in Phys.

[8] M. Barth, et. al., "Jet-Like Properties of Multiparticle Systems Produced in K^+p Interactions at 70 GeV/c," Nucl. Phys. B192 (1981) 289.

[9] D. Brick, et. al., "Comparison of 147 GeV/c π^-p Low Transverse Momentum Hadron Production with Deep-Inelastic Leptoproduction," Z. Phys. C11 (1982) 335.

This thesis investigates the second and third points above in a broader context. In particular the valence quark structure of the initial and final state will be related to the dynamics of the strong interaction. By isolating quarks common to particles in both the initial and final states we examine the *flavor flow* through the interaction.

In order to establish a basis for discussion we will chose to examine our results from the point of view of two distinct models, namely the hadron *dissociation* model and the LUND *fragmentation* model.

The basic concepts of the dissociation model were introduced in 1972 by Goldberg.[10] He contended that the final state spectrum of particles should reflect the initial state wave function of a colliding hadron. Consider the non-leading reactions $pp \rightarrow \pi^{\pm}X$ which contain a single valence quark common to the initial state baryon and the final state meson (u for the π^+ and d for the π^-). Goldberg deduced that the production of mesons in the limit $x_f \rightarrow 1$ should be related to the probability for the initial state quark to carry a momentum fraction equal to x_f within the baryon. That is to say the valence quark distribution functions $u(x)$ and $d(x)$ measured for the proton in deep inelastic scattering should describe the observed invariant differential cross section for the production of π^+ and π^- respectively. This idea was independently introduced by Ochs in 1977[11] under the name of hadron dissociation. Ochs' concept of dissociation, which was implicit in Goldberg's paper, refers to the view of the strong interaction process as a filtering of the initial wave function of each particle into a collection of independent constituents. The final state is then arrived at by the pairing of valence quarks with sea quarks to form mesons. It is important to understand in this picture that at least some component of the initial distribution of quarks passes through the interaction essentially undisturbed and subsequently materializes as mesons. In the following we will not consider extensions of the dissociation model such as the *recombination*[12] or *valon*[13] models.

The dissociation model was motivated by the similarity between the structure functions measured by deep inelastic scattering and the meson spectra. A similarity was also observed between the spectra of mesons produces in e^+e^- and hh scattering. In interpreting this the Lund model[14] was formulated in terms of a final state hadronization akin to the color confinement process in $e^+e^- \rightarrow q\bar{q} \rightarrow$ *hadrons*. In making this connection explicit the model removes any dependence on the initial state other than the

---

[10] Hyman Goldberg, "Predictions for Inclusive Reactions Based on a Parton Structure of Hadrons," Nucl. Phys. B44 (1972) 149.

[11] W. Ochs, Ibid.

[12] K. P. Das and R. C. Hwa, "Quark-Antiquark Recombination in the Fragmentation Region," Phys. Lett. 65B (1977) 459.

[13] L. Gatignon, et. al., "Determination of the Internal Structure of Valons," Z. Phys. C 16 (1983) 229.

[14] B. Andersson, et. al., Ibid.

identity of the valence quarks.

Both of the models reflect our inability to comment on the actual strong interaction process. The dissociation model emphasizes the initial state due to our understanding of lh scattering, while the LUND model is of the fragmentation type due to its basis in e^+e^- scattering. These models therefore represent two distinct and apparently opposing points of view.

1.2 DEVELOPMENT OF THE FERMILAB HYBRID SPECTROMETER

In order to determine the quantum numbers present in multiparticle final states we require a variety of detectors. The following describes the historical development of the apparatus necessary for such determination.

In the early years of particle physics photographic techniques were predominant. With the great advances in high speed electronics and other instrumentation over the past fifteen years electronic detectors of enormous proportions have been realized. During that time it was only natural to adapt the bubble chamber into a larger system of detectors.

In the early seventies the first hybrid spectrometer[15] was built in the combination of the 30″ hydrogen bubble chamber with upstream and downstream wire chambers at Fermilab. This technique exploited the effectiveness of the visible target with the accuracy of a magnetic spectrometer.

In the latter part of the decade work was begun on three large hybrid detector systems. At CERN the EPI[16] (External Particle Identifier) ran with BEBC in RF separated kaon beams. This experiment was concerned with the study of diffractive production. Subsequently the EHS[17] (European Hybrid Spectrometer) was built at CERN as a facility. A similar apparatus, the FHS (Fermilab Hybrid Spectrometer), was constructed in the U.S. This was a joint undertaking of the International Hybrid Spectrometer Consortium (IHSC) and Fermilab.

In order to undertake studies such as the present investigation of flavor flow each of the second generation hybrid spectrometers included large acceptance detectors for the identification of secondaries in the forward hemisphere. In the Fermilab apparatus this system of detectors came to be known as the Downstream Particle Identifier or DPI.

1.3 OVERVIEW OF FINAL STATE PARTICLE IDENTIFICATION

[15] D. Fong, et. al., "Cross Sections and Charged Multiplicity Distributions for π^-p and K^-p Interactions at 147 GeV/c," Nuclear Physics B102 (1976) 386. This detector was referred to as the proportional hybrid spectrometer or PHS.

[16] V. Baruzzi, et. al., "Use of a Large Multicell Ionization Detector – The External Particle Identifier in Experiments with the BEBC Hydrogen Bubble Chamber," NIM 207 (1983) 339.

[17] M. Aguilar-Benitez, et. al., NIM 205 (1983) 79.

The problem of particle identification has been and continues to be addressed in a variety of ways. The most detailed experiments to date have employed focusing spectrometers instrumented with Čerenkov counters to measure single particle inclusive spectra. These include the Fermilab Single Arm Spectrometer[18] (low p_t), the Chicago-Princeton collaboration[19] (high p_t), and a series of ISR experiments[20] (highest energy). One ISR experiment[21] in fact measured limited two particle distributions by the use of two asymmetrically placed spectrometer arms, while a second[22] employed a symmetric geometry.

While multicell threshold Čerenkov counters have found a natural place in the colliding beam detectors[23] they are severely limited for use in fixed target work. Due to the larger range of secondary momenta, the tight collimation of the forward jet, and the properties of segmented Čerenkov counters they have not made significant contributions to broad based fixed target experiments.

Ionization loss (or dE/dx) detectors have doubtless claim to being the most important type of high energy physics instrumentation. From photographic emulsion, the Geiger tube, bubble chambers, wire chambers, and solid state detectors the contributions have been too many to enumerate. Particle identification via dE/dx measurement has been used reliably at low momenta, most notably in bubble chambers. In 1967 Ramana-Murthy and Demeester[24] first discussed the use of proportional wire chambers as dE/dx detectors. This was in the context of deep ($\approx \frac{1}{2}$ m) chambers for single particle detection. This work nonetheless established the basic principles of operation and analysis in use today. In 1973 Lehraus[25] and coworkers at the EPI extended this idea to multi-particle identification by the use of many samples of the ionization along a track. By segmenting the counter along the particle's line of flight and one transverse dimension it was possible to associate individual ionization samples with their

[18] D. Cutts, et. al., "Experimental study of Low-p_t Hadron Fragmentation," Phys. Rev. Lett. 43 (1979) 319.

[19] J. W. Cronin, et. al., "Production of Hadrons at Large Transverse Momentum at 200, 300, and 400 GeV/c," Phys. Rev. D 11 (1975) 3105.

[20] J. Singh, et. al., "Production of High-Momentum Mesons at Small Angles at a CM Energy of 45 GeV/c at the CERN ISR," Nuclear Physics B140 (1978) 189.

[21] M. G. Albrow, et. al., "Correlations Between Two Identified Charged Hadrons at the CERN ISR," Phys. Lett. 65B (1976) 295.

[22] G. J. Bobbink, et. al. "Correlations Between High-Momentum Mesons in $p + p \rightarrow \pi + pi + X$ at $s^{1/2} = 63$ GeV," Phys. Rev. Lett. 44 (1980) 118.

[23] For example DELCO at SLAC/PEP and TASSO at DESY/PETRA.

[24] P. V. Ramana-Murthy and G. D. Demeester. "The use of Gas Proportional Counters to Distinguish Protons from Pions in the Cosmic Radiation at Energies of Near or Greater than 100 GeV/c", NIM 56 (1967) 93. P. V. Ramana-Murthy. "Relativistic Rise of the Most Probable Energy Loss in a Gas Proportional Counter", NIM 63 (1968) 77.

[25] D. Jeanne, et. al. "High Energy Particle Identification using Multilayer Proportional Counters", NIM 111 (1973) 287.

parent track. Allison[26] dramaticly improved upon this in 1974.

Allisons's scheme (ISIS: the identification of secondaries by ionization sampling) transformed EPI's MWPC cell array into a large drift chamber. Longitudinal segmentation was achieved by a simple structure of anode and cathode wires, while the transverse "segmentation" was arrived at by drift timing. The design for ISIS was used for the E570 CRISIS. It has also been applied to the SLAC TPC,[27] CEASAR's CLEO[28] as well as other existing and planned experiments.

This technique promises identification over a broad range of momenta. It is, however, limited by the statistics of ionizing collisions to a marginal utility. An improvement in resolution may soon be found in the development of longitudinal drift detectors using flash ADCs to sample the charge in sub-millimeter intervals.[29]

A brief comment on the most recent advance in multi-particle identifiers is in order. In 1976 Seguinot and Ypsilantis investigated the use of MWPC to image Čerenkov photons[30] and thereby accomplish particle identification at the highest energies. Since that time many such *ring imaging* detectors have been discussed. Recent single track results with one such device indicate a generally unambiguous identity with even just one Čerenkov photon detected.[31]

---

[26] W. W. M. Allison, et. al. "The Identification of Secondary Particles by Ionization Sampling (ISIS)", NIM 119 (1974) 499.

[27] H. Aihara, et. al., IEEE Trans. on Nucl. Sci. 30 (1983).

[28] R. Ehrlich, et. al., "Particle Identification by Ionization Measurements: Description of the CLEO dE/dx System," NIM 211 (1983) 17.

[29] T. Oshima, et. al., Proc. Int. Conf. on Instrumentation for Colliding Beam Physics, SLAC-250 (1982) p. 101.
R. Ara, et. al., KEK-P-82-24, submitted to NIM.
T. Ludlam, et. al., Proc. Int. Conf. on Instrumentation for Colliding Beam Physics, SLAC-250 (1982) p. 96.

[30] J. Seguinot and T. Ypsilantis, NIM 142 (1977) 377.

[31] M. Adams, et. al., "$\pi/K/p$ Identification with a Large-Aperture Ring-Imaging Čerenkov Counter," NIM 217 (1983) 237.

Chapter 2

APPARATUS

The Physics objectives of E570 dictated a great many experimental requirements. Among the most significant of these were:

- a variety of beams were necessary along with a system to identify each beam particle
- a large magnetic spectrometer was needed for track reconstruction with good momentum resolution
- detectors were needed to identify charged secondaries and to reconstruct neutral pions.

The equipment used to meet these goals is described in the following sections.

All of the beam line systems, including the Čerenkov counters and muon identifier, were provided by Fermilab. The laboratory provided the 30″ hydrogen bubble chamber and its crew of operators. They also provided the on-line computer, its CAMAC interface, and a variety of other control system interfaces. The PREP electronics facility provided the logic units used in gating and the majority of the ADCs used by the FGD. The IHSC fabricated all other detectors and their associated electronics.

2.1 BEAM LINE

The 30″ bubble chamber is the terminus of the N3 beamline in the Neutrino Department at Fermilab. This line as well as its parents (N0 and N7) underwent major renovations in order to prepare for E570

in a fashion consistent with the departmental goals for the Tevatron era.[1, 2]

What follows is a description of those beam line elements which impact the Physics content of E570. This brevity of treatment can in no way diminish the complexity of a mile long beam transport nor the talent of its designers.

2.1.1 Primary Beam

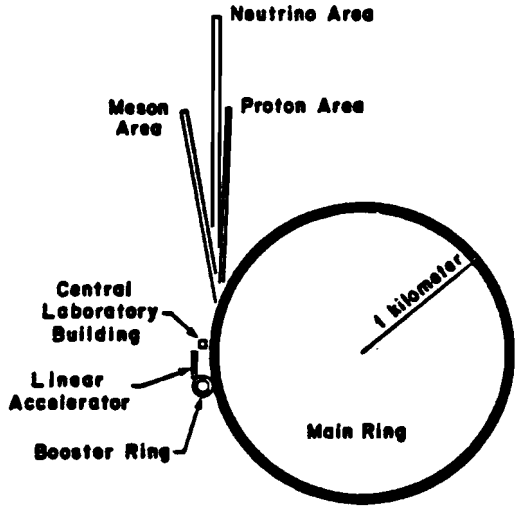

Figure 2.1 The Fermilab accelerator complex and external beam lines.

During the 1980-81 running period the Fermilab proton synchrotron (figure 2.1) was operated at an energy of 400 GeV/c with intensities in the range of 2 to $3 \cdot 10^{13}$ protons per pulse. After acceleration half of the beam was resonantly extracted over a period of one second. In the switchyard (figure 2.2) a fraction of this continuous stream of particles was chopped into the N0 line. The beam was broken into six packets (or *pings*) each containing roughly 10^{10} protons in a time slice of 500 microseconds. The individual pings spanned the slow spill at 200 millisecond intervals. This particular beam structure accommodated several performance factors. First multiple pings allowed the bubble chamber to be expanded and compressed six times per accelerator cycle giving acceptable data rates. Second the pings were short compared to the bubble growth time (5 ms) so that all the tracks in a ping had a uniform size on film. And finally the pings were long compared to the live times ($\leq 6\,\mu s$) of all the electronic

[1] R. Stefanski, "400 GeV/c Proton Transport to a Modified Neutrino Area," Fermilab TM-937.

[2] A. Malensek, "New N3 Beamline Design," Fermilab TM-940, (1980).

detectors so that it was rare for two beam particles to overlap one electronic time slot. (The reader should bear in mind that at the bubble chamber a ping contained on average six particles).

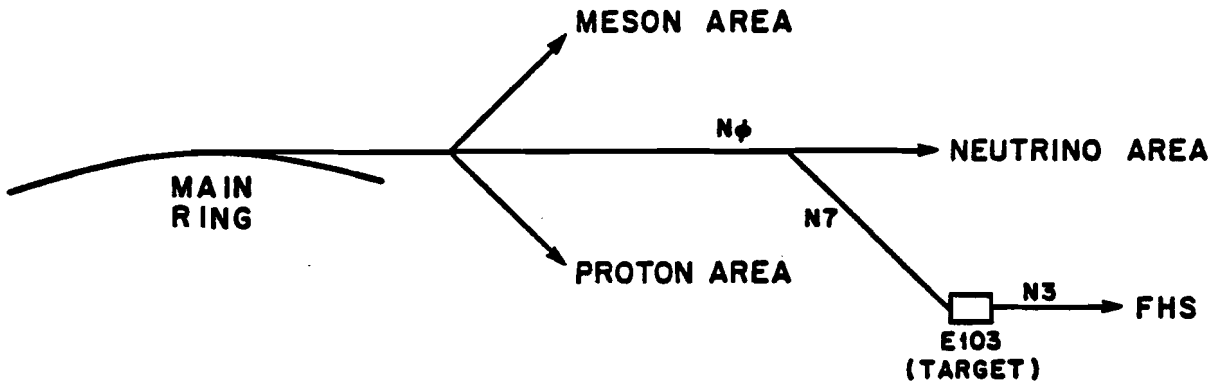

Figure 2.2 Primary beam was extracted from the main ring and fed to the FHS via the N0, N7, and N3 beamlines.

2.1.2 Secondary Beam

In order to achieve a mixed beam of pions, kaons, and protons the primary beam was brought to fall on a target. The produced secondaries were then momentum selected to define the experimental beam of 200 GeV/c. E570 used a target of copper which measured 1″ in height by $\frac{3}{8}$″ in width by 4″ in length.

Along the primary beam direction one expects the secondaries to be dominated by high momentum protons and pions with only a small admixture of kaons. The Chicago-Princeton data[3] provide some insight here. They show that in energetic proton-nucleus collisions the ratios of kaons to pions and of protons to pions increase with increasing p_t. They further demonstrate that at a beam momentum of 200 GeV/c these ratios saturate by a p_t of 3 GeV/c. In order to capitalize on the relatively large number of kaons at higher p_t the secondary beam line viewed the primary line at a production angle of 3 milliradians in the horizontal plane and zero degrees vertically. Further control over this angular matching was accomplished by a vertical bend directly after the target. This allowed the production angle to be varied in the range of 3 to 3.7 mr.

After the beam line and Čerenkov counters were operational a study was undertaken to find the production angle which yielded the largest fraction of kaons in the beam consistent with a small muon contamination. This effort was also constrained by the amount of primary beam which could be delivered

[3] J.W. Cronin, et. al., "Production of hadrons at large transverse momentum at 200, 300, and 400 GeV/c," Phys. Rev. D 11 (1975) 3105.

to the target for safety reasons. The optimum value of the production angle (3.1 mr) yielded 17% of all beams as kaons. It was, however, not possible to maintain this fraction during the entire run for a variety of reasons.

2.1.3 Particle Filter

Various techniques are know which will diminish the fraction of protons in a beam relative to the fractions of pions and kaons.[4] In line with Neale's original concept for the N3 beamline E570 used a cylinder of polyethylene 15″ in diameter by 20′ in length as a differential particle filter. This method of filtering is easily understood when one examines the various absorption cross sections. One finds that $\sigma_p^{abs} > \sigma_\pi^{abs} > \sigma_K^{abs}$ in collisions with nuclear targets.[5] That is to say the protons scatter out of the beam more frequently than the pions and in turn the kaons.

2.1.4 Momentum Selection

After having struck the target and passed through the filter the beam was bent and dispersed (figure 2.3) such that an on-momentum particle would pass through a distant collimator. The N3 beamline geometry produced a momentum byte of $\Delta p/p = 1.9\%$.

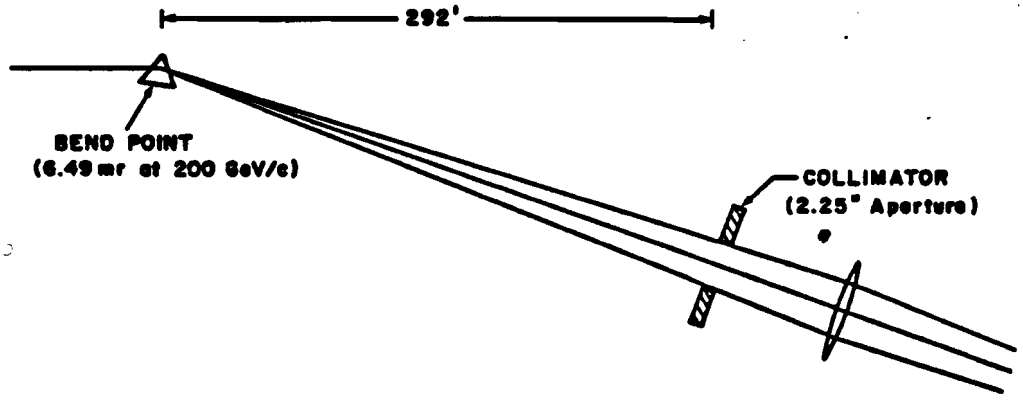

Figure 2.3 The beam was bent and collimated in order to define a precise beam momentum.

2.1.5 Final Transport

[4] W.W. Neale, "Enriched Particle Beams for the Bubble Chambers at the Fermi National Accelerator Laboratory," FN-259, 1974.

[5] S.P. Denisov, et. al., Nuclear Physics B61 (1973) 62.

The remainder of the N3 beamline was designed to deliver on-momentum particles to the bubble chamber. The E570 beam tune provided for particle trajectories which were parallel to the optic axis for the entire length of the E116 Čerenkov counter and trajectories with an angular RMS of 0.25 mr in the shorter E118 counter.[6]

The final elements in the line were a quadripole and a series of 68″ diameter toroidal magnets totalling 22′ in length. The quad fanned the beam out so that it was 8 cm high by 1 cm deep in the focal plane of the bubble chamber cameras. The toroids had a 3″ hole bored through their length in order to admit the beam. The magnetized iron served to sweep muons out of the space surrounding the beam in order to reduce this background in the bubble chamber and DPI.

2.2 BEAM TELESCOPE

Having achieved a beam of mixed particle content it becomes necessary to identify (or *tag*) each beam particle as it enters the apparatus. During each ping an average of six particles entered the FHS. As each particle entered the upstream system a short gate was generated to record all data relevant to that track. Thus the beam arrivals were recorded in *time slots* (120 ns) which were short compared to the time interval expected between two beams (roughly 80 μs). Each time slot must contain sufficient information to determine the identity of the beam particle. At the same time the particles trajectory must be determined for two reasons. The first being the non-zero divergence of the beam at the target and the second and more important being the fact that all the tracks in a ping appear on one bubble chamber picture. It is therefore necessary to reconstruct the event vertex in space before the correct time slot and its Čerenkov tag can be associated with it.

The logging of upstream beam parameters was accomplished using a series of Čerenkov counters and proportional wire chambers (PWCs) under the supervision of the experimental trigger.

2.2.1 Čerenkov Counters

The original expectations for the experiment included the use of two differential Čerenkov counters to tag the beam particles. A mechanical instability in the mirror mounting for one of the counters would, however, not allow operation in the differential mode at 200 GeV/c. For this reason a third counter was pressed into service allowing for one differential and two threshold counters.

The differential head is illustrated in figure 2.4. One sees that these were typical of differential counters.

After the counters had been optically aligned, and before data taking had started in earnest, pressure

[6] A. Malensek, op. cit.

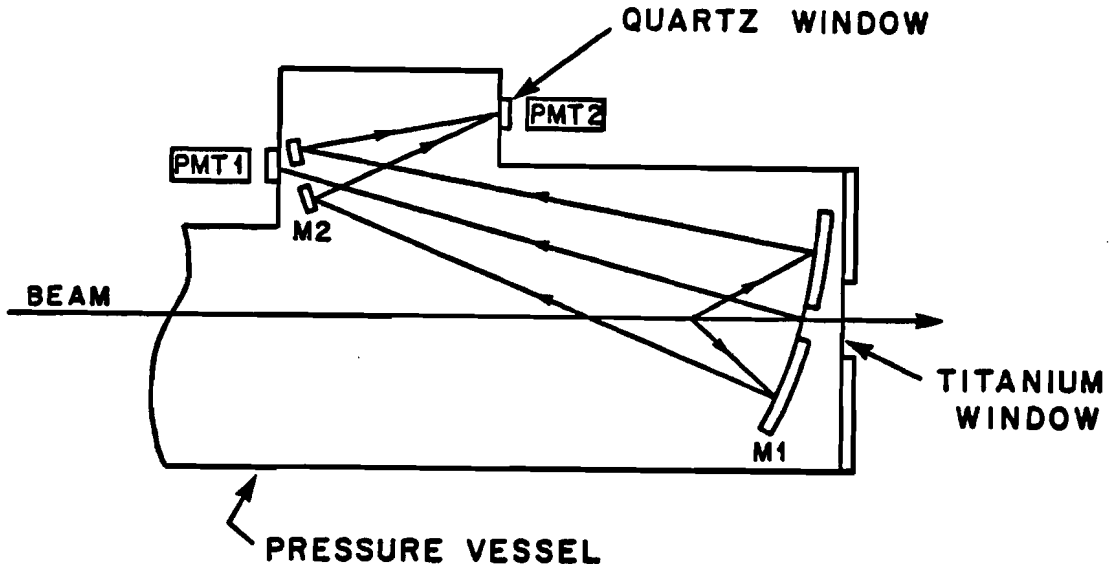

Figure 2.4 The system of mirrors and photomultiplier tubes used in the differential Čerenkov heads.

curves were taken for the Čerenkov counters.

2.2.2 Beam Definition Chambers

A series of three PWC triplets were used to determine the beam trajectory as it entered the FHS. (This system will be referred to as PWU and can be seen schematicly in figure 2.5). Each wire plane had an active area of 10 cm × 10 cm and the individual planes were staggered by 120° within a triplet. The sense wire spacing was 2 mm. These same chambers had been used in E154 and E299 and their full description lies in the reports of these experiments[7]. For E570 the wire planes were rewound. In order to achieve low mass the cathode planes were typically formed by planes of wires set at 90° to the anode wires. As an experiment the A triplet was outfitted with cathode planes of thin aluminum sheet bonded to polystyrene. This led to their somewhat reduced efficiency.

2.2.3 Master Gate

Unlike many of its contemporary hybrid experiments[8] E570 was run without an interaction trigger.

[7] The unpublished Proportional Hybrid Spectrometer Consortium (PHSC) Newsnotes describe both the hardware and software used in E154 and E299. In regard to PWU one should consult R. Downing, et. al., "Upstream PWC Chambers and Amplifiers," notes #6, Aug. 1971, and #14, Oct. 1971.

[8] For example NA16, the LEBC-EHS experiment (M. Aguilar-Benitez, et. al., NIM 205 (1983) 79), used a simple scintillator arrangement, while NA23, the RCBC-EHS (J. L. Bailly, et. al., Z. Phys. C 23 (1984) 205), ran with a

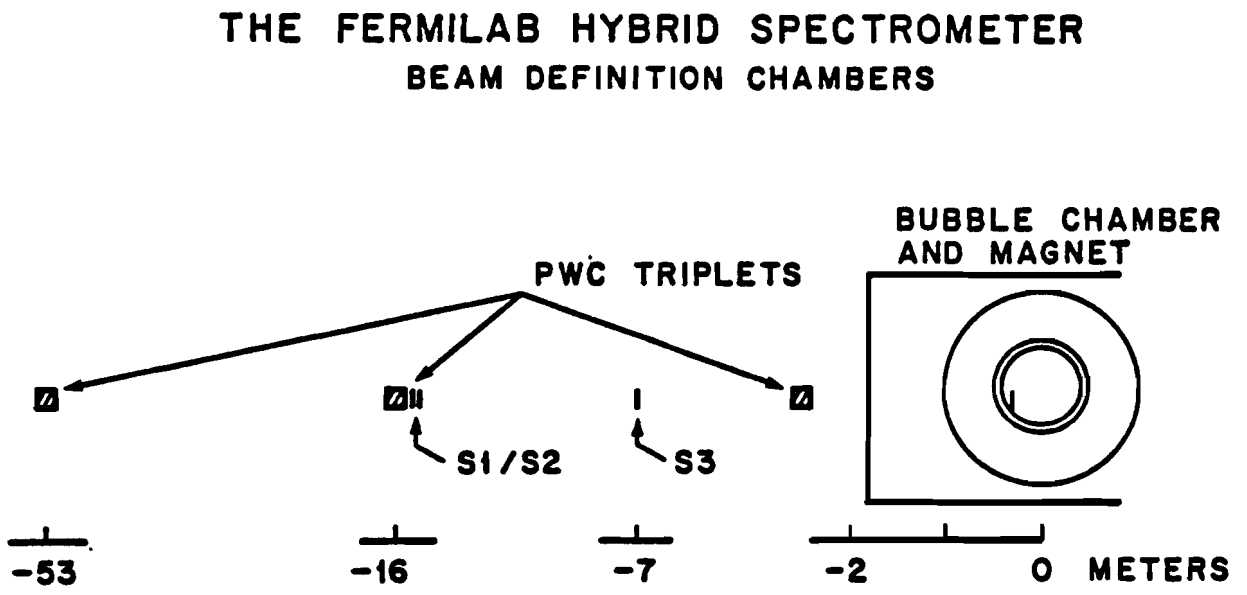

Figure 2.5 The upstream wire chamber system was composed of three PWC triplets. Also shown are the locations of the scintillators used in defining the beam trigger.

That is it was run in the classical minimum bias fashion — a picture was taken for each beam ping. In order to initiate a data taking cycle one therefore needed only to determine the presence of a particle in the beamline. As the Fermilab Accelerator Division provided the pings at precise intervals based on the accelerator clock this was a simple matter. Referring to figure 2.6, two logic levels BOP and EOP (respectively beginning and end of ping) were formed using the bipolar, encoded accelerator clock. These levels formed the gate for PING TIME valid. This was ANDed with the discriminated outputs of the three beam scintillators (figure 2.5). The coincidence thus formed (MASTER GATE) initiated the data taking for all detectors for one time slot. Furthermore the bubble chamber functions of expansion, camera flash, film advance, and recompression were all driven by the accelerator clock.

Although it was a rare occurrence it was possible for two beams to enter the tagging system within a single time slot. The MASTER GATE one-shot was therefore operated in an updating mode so that both of the beams and their eventual products would be faithfully recorded. The only non-recoverable information in this case would be due to certain ambiguities in the Čerenkov tag.

2.2.4 Muon Identifier

As a muon gave the same signal as a pion in the Čerenkov counters their presence in the beam had to be flagged by another technique. A beam dump was formed behind the FGD to stop any hadrons and

somewhat more sophisticated scintillator hodoscope.

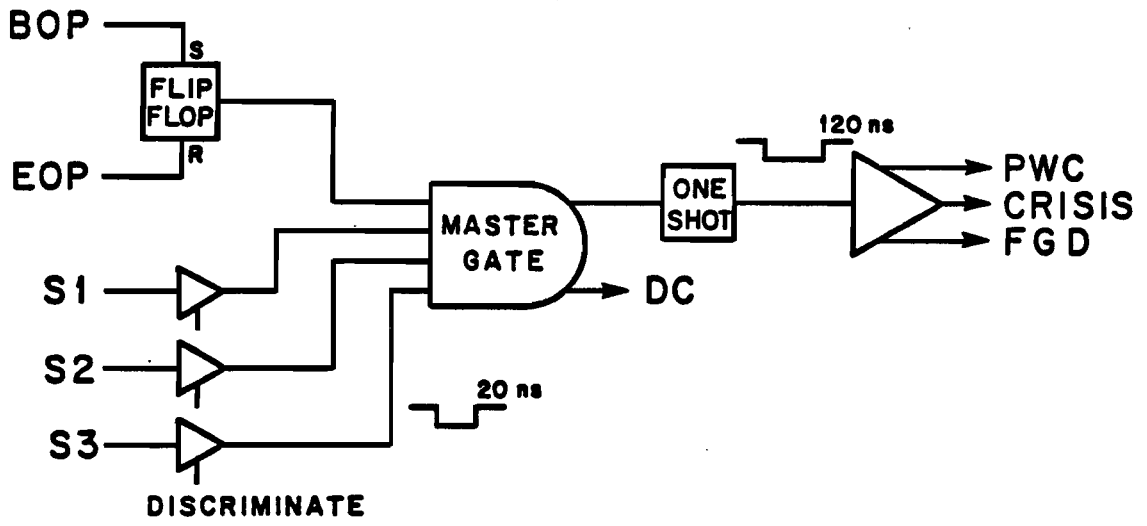

Figure 2.6 Trigger logic for the MASTER GATE.

pass the muons. The dump consisted of 12′ of steel followed by 6′ of concrete. Large scintillator paddles were placed before and after the concrete to flag the muons.

Although the muons comprised a rather small fraction of the beam it is of course necessary to remove them from the data sample in order to obtain correct pion cross sections.

2.3 TARGETS

E570 employed an active liquid hydrogen target in the form of the 30″ hydrogen bubble chamber (most often referred to simply as the 30″). E565 was approved for concurrent running with E570. This experiment used a series of metal foils mounted inside the bubble chamber as targets. Taken together these experiments investigate sixteen combinations of beam (π^+, π^-, K^+, p) and target (p, Mg, Ag, Au) under identical circumstances.

2.3.1 30″ Hydrogen Bubble Chamber

The 30″ has had a long history of service. The chamber was originally built by MURA for use at the Argonne ZGS and took its first Physics pictures in 1964. In 1972 the chamber was moved to Fermilab. E570 was the final experiment in which the chamber would be used as it was officially decommissioned by Fermilab in June, 1982.

The bubble chamber embodies apparatus necessary for three distinct functions. First there are the refrigeration and expansion systems which provide track sensitivity. Second there is the optical system including the cameras for the recording of track images. And third there is the large Helmholtz coil

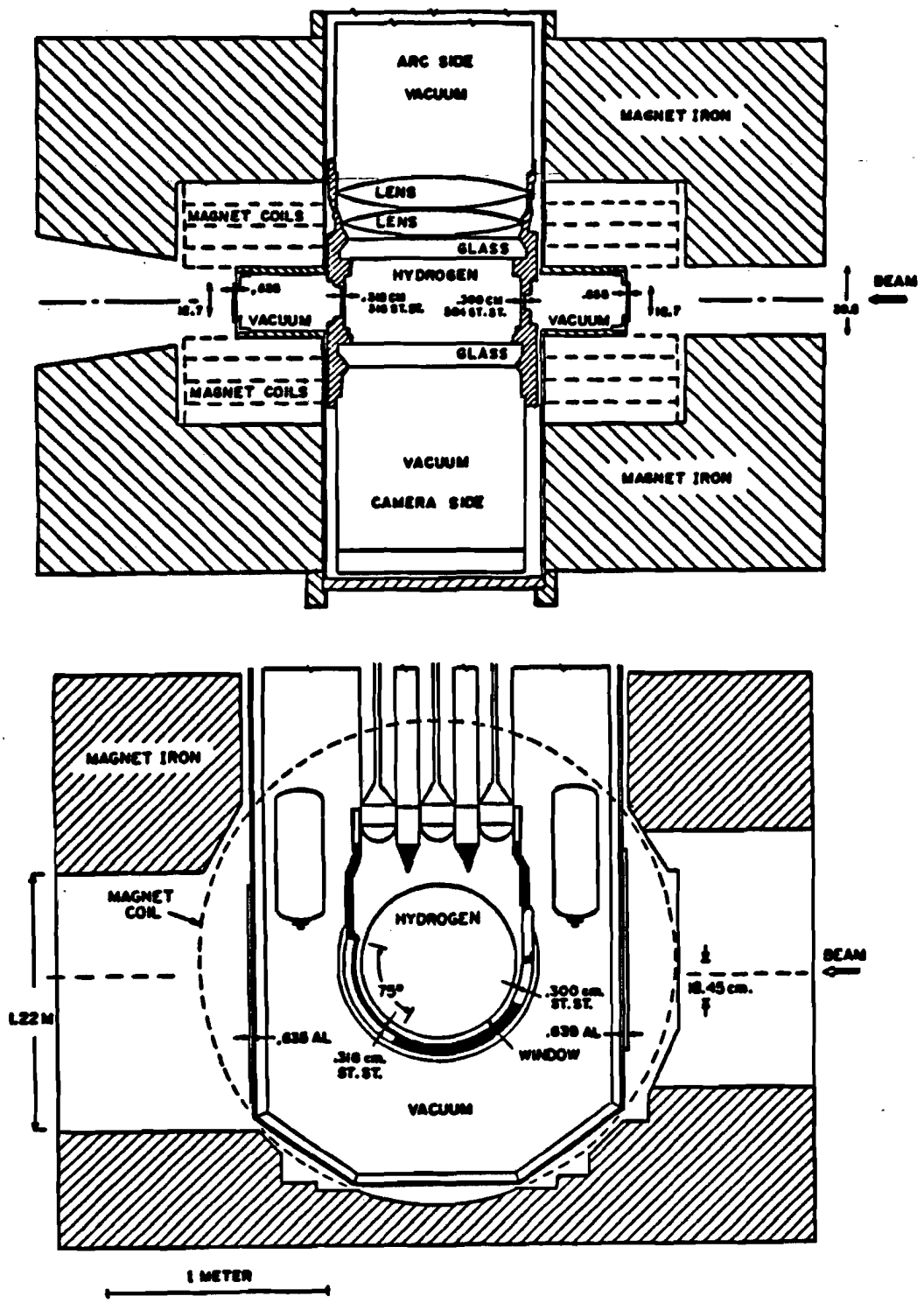

Figure 2.7 Plan (upper) and elevation (lower) views of the 30" hydrogen bubble chamber.

magnet which surrounds the active volume of the chamber.

Figures 2.7 and 2.8 show the chamber in elevation, plan and cross section. The chamber body hangs from the frame which bears the expansion and control systems. On either side of the chamber are the large water cooled copper magnet coils. Each coil is supported by a forty ton iron return yoke. The coil aperture accommodate 36″ diameter glass windows on each side of the chamber.

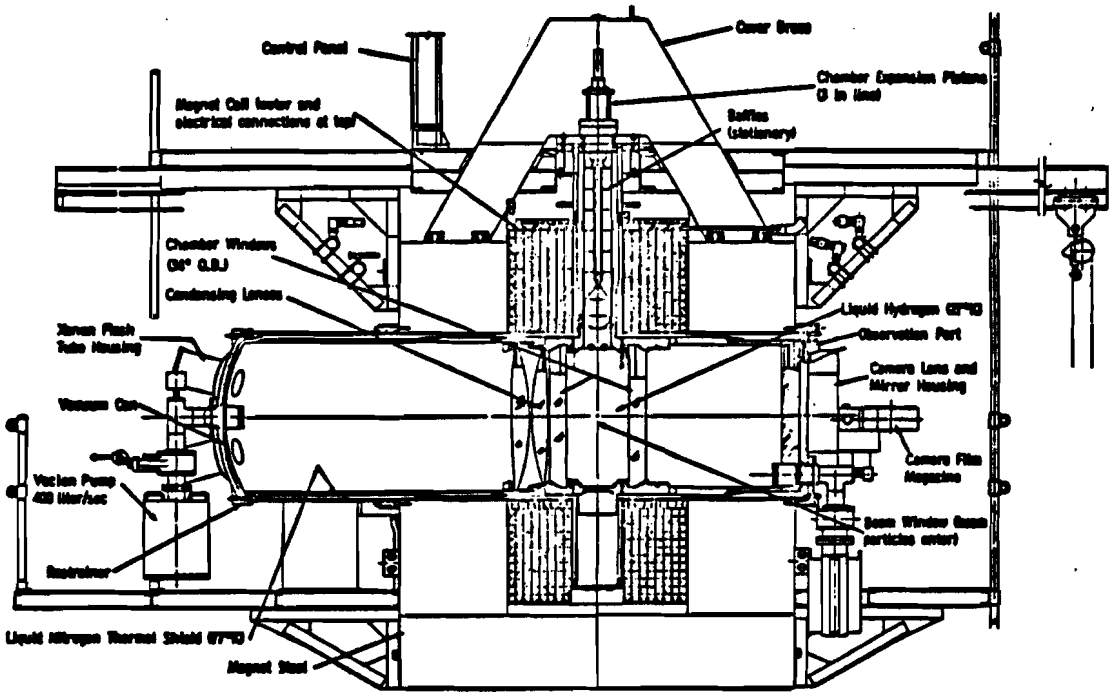

Figure 2.8 Cross section view of the 30″ chamber showing details of the mechanical, expansion, optical, and magnetic systems.

Control over the chamber was maintained at all times by a crew of four trained operators.

The various chamber parameters were maintained so as to provide a bubble size of 400 μm and a density of 18 bubbles per centimeter.

Tracks were photographed using the dark field illumination technique. Light from an elliptical xenon flash tube (hence the name *arc side*) was focused so that as it passed through the chamber it would form a ring about its corresponding camera aperture on the other (*camera*) side. In this way only scattered light (as from a bubble) would reach the film. E570 employed four cameras mounted in a square grid $\frac{1}{2}$ m on a side located $1\frac{2}{4}$ m from the chamber center. Three of these cameras were standard to the bubble chamber. The film transports were fitted with magazines containing three thousand frames of

35 mm film. A fourth camera was situated with its optic axis in the plane of the nuclear target holder. This camera was especially developed[9] to record with better resolution a limited area just downstream of the E565 targets.

The magnet had a supply voltage of 200 V and was operated at a current of 11.4 kA. The radially symmetric field produced by the magnet is shown in figure 2.9. The peak value of the field was 20 kG and $\int B \cdot dl$ was 34 kG · m.

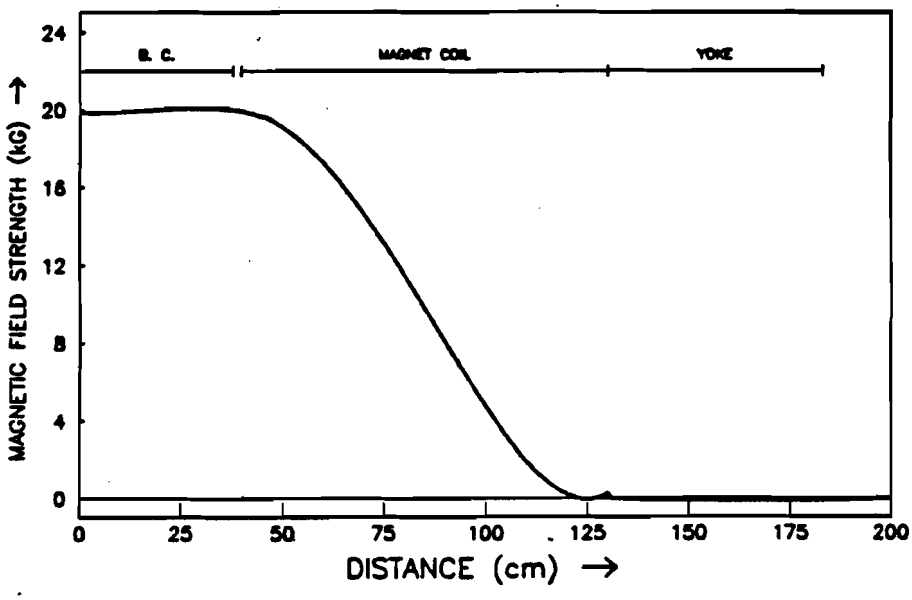

Figure 2.9 Magnetic field strength along the z direction as a function of distance from the center of the bubble chamber.

Particles entered and exited the chamber through windows in the chamber body. The entrance window was 0.300 cm of type 304 stainless steel, while the exit was 0.318 cm of type 316 stainless steel. Of less significance an additional $\frac{1}{8}''$ of aluminum was presented to each track which traversed the cryogenic vacuum tank surrounding the chamber.

2.3.2 Nuclear Targets

The target materials selected for E565 were magnesium, silver, and gold. Each material was present in two thicknesses in order to assess the affects of multiple interactions in the target material.

[9] P. Haridas and S. Noguchi, "Data Box Modifications for E565/570," APC Engineering Note 81-9.
P. Haridas and S. Noguchi, "The IHSC High Resolution Camera at the Fermilab 30" H_2 Bubble Chamber," APC Engineering Note 82-7.

The individual target *plates* were soldered to a specially fabricated holder,[10] which was in turn welded into the upstream end of the chamber in line with the lower beam window.

2.4 THE DOWNSTREAM PARTICLE IDENTIFIER

The Downstream Particle Identifier (DPI) is illustrated schematicly in figure 2.10. There were a total of four independent detectors used in the E570 DPI: seven planes of proportional wire chambers (PWD), nine planar drift chambers (DC), a large volume drift chamber (CRISIS), and a lead glass electromagnetic calorimeter (FGD). Along with the bubble chamber these detectors functioned to reconstruct the momentum, mass, and production angles of charged secondaries as well as the energy and production angles of final state γ-rays. [11] The DPI was designed to provide good acceptance for particles produced in the forward hemisphere of high energy collisions.[12]

The following paragraphs will describe the major mechanical properties of the detectors.

2.4.1 Proportional Wire Chambers

The downstream PWC system contained a total of 3300 wires configured in 7 planes. Two planes measured 60 cm × 50 cm while the remaining five were 1 m × 1 m. Because of their large size each chamber used sheets of HEXEL painted with silver as cathode planes. This afforded a rigid, flat surface for the cathodes with a minimum of mass. The sense planes were wound with a wire spacing of 2 mm.

These chambers used so called *magic gas*, which was mixed on-line.[13]

The two smaller planes were mounted on the downstream magnet face with their wires parallel to the magnetic field and offset with respect to each other by 1 mm to allow a precise measurement of the magnetic deflection of particles which entered the DPI.

2.4.2 Drift Chambers

The two sections related specifically to DC (this and §3.1.2) contain a greater level of detail than those describing the other detectors. This unevenness of treatment is required to provide historical documentation for the drift system.

2.4.2.1 Mechanical details

[10] This target was constructed under the supervision of W. Smart of the Fermilab Bubble Chamber Staff.

[11] For another experiment (E597) the FGD was replaced by a segmented Čerenkov counter (OSIRIS) and a lead-scintillator hadron calorimeter. See Fermilab P597 for details.

[12] T. B. Stoughton, et. al., "Acceptance and Resolution Studies for the Fermilab ISIS," DPI Note #5. (unpublished)

[13] D. Goloskie, et. al., "Operating Procedures for the E565/570 PWC Gas System," APC Engineering Note 82-2.

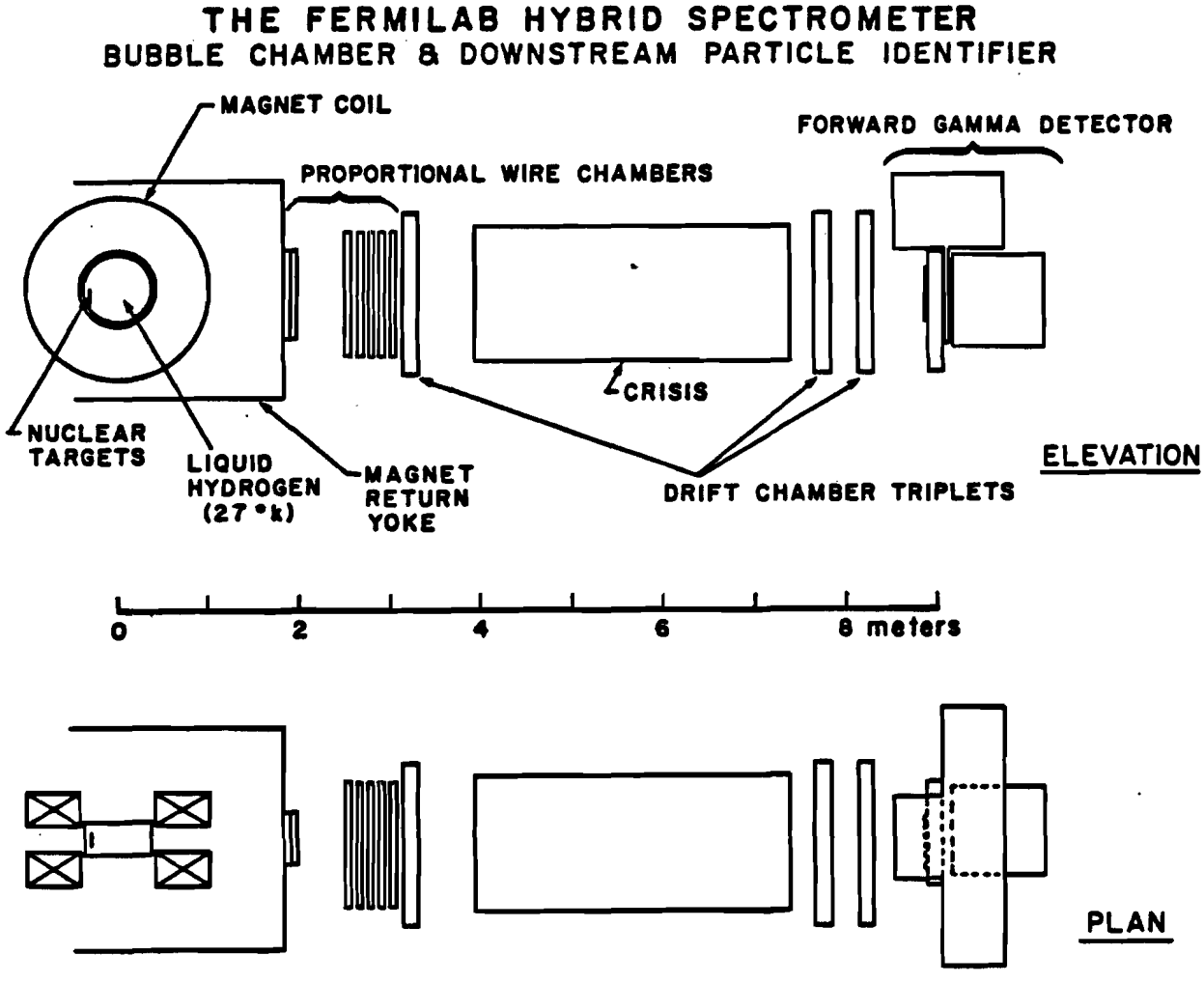

Figure 2.10 Elevation and plan views of the Downstream Particle Identifier.

The E570 drift chambers closely resemble those of Breskin, et. al. [14] The basic cell is illustrated in figure 2.11. The sense (anode) wire was surrounded by a series of field (cathode) wires. The field wire voltages were graded in steps from ground near the sense wire to the cathode high voltage at the inter-cell boundary. Each cell had a total drift space of 2" and a total of 24 such cells were incorporated into each 1.2m × 1.2m plane.

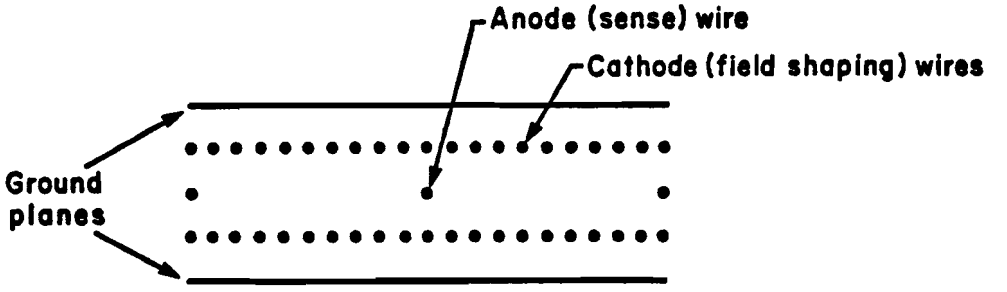

IHSC E565/570 Drift Chamber Cell

Drift volume: 2" x 3/8" x 48"

	ANODE	CATHODE
WIRE DIAMETER	20μm	100μm
OPERATING VOLTAGE	1.25 kV	2.25 kV

Figure 2.11 A cross sectional view of a drift chamber cell.

The planes were formed by alternately stacking wire wound frames of printed circuit board and G-10 spacers. A G-10 U-channel frame formed the overall structural support. High voltage and signal circuits were accommodated on the printed circuit boards. Channels for gas distribution were cut into the various frames. O-rings were placed between each layer of the stack providing gas tight chambers when the stack was bolted to its frame. Aluminized mylar windows covered the two chamber faces. The planes were configured into 120° triplets supported by large aluminum frames.

Gas flowed through the chambers of a triplet connected in series at a rate of $\frac{1}{2}$ cubic foot per hour. A head of $\frac{1}{4}$" vacuum pump oil was maintained at the exhaust side of the final plane in the triplet.

2.4.2.2 Electric field and electron drift

[14] A. Breskin, et. al., "Further Results on the Operation of High-Accuracy Drift Chambers," NIM 119 (1974) 9.

When a minimum ionizing particle traversed the $\frac{3}{8}''$ gap between the cathode planes 80 to 100 electron-ion pairs were produced from the gas.[15] In the electric field of the cell electrons were drawn toward the anode and the positive ions toward the cathode at the inter-cell boundary. At sufficiently high field strength the electron's motion is characterized by a constant *drift velocity.* This is due to its atomic collision cross section reaching a value where the energy gained from the field is balanced by that lost into thermal excitation of the gas. The electrons reach their terminal velocity essentially at creation. Hence, the location of a track is simply proportional to the time it takes the electrons to drift to the anode.

It is possible to accomplish track reconstruction using non-saturated drift. The added complexity of a non-linear, experimentally derived relationship between distance and time is, however, a major drawback. In order to insure a linear time to distance relationship the electric field produced at various chamber voltages was investigated for the E570 cell.

The scalar potential produced within a cell was calculated using a technique described in appendix A. Figures 2.12 and 2.13 illustrate the solution achieved at the nominal chamber operating voltages. In regard to figure 2.13 it is interesting to note that the surface describing the potential is identical mathematically to the result of pushing rods into a stretched sheet of ideal elastic, the displacement (radius) of each rod determined by the voltage (radius) of the corresponding wire. Figure 2.14 serves to show the uniformity of the field by the parallel structure of the equipotentials.

We also note that near the cell edge it is possible for electrons to be ejected from the active volume of the cell. A guard (cathode) wire was located at the cell boundary in the sense wire plane. This wire was held at the same voltage as the two adjacent field wires. The resulting potential is seen to be radial about each wire, but with a larger extent about the guard wire. As a result there are gradients which push electrons away from the central plane and out into the space between the field wires and the ground plane. This results in an observed reduction in efficiency within a few millimeters of the inter-cell boundary.

Bringing our attention back to saturated drift velocity we see in figure 2.14 a plot of the electric field strength produced along the central plane of the chamber. For most of the drift space the field has a constant value of roughly 800 V/cm. This value is well suited to the saturation characteristics of the HRS gas[16] used for the majority of running. We also note that near the surface of the anode wire the field rises to $\approx 10^4$ V/cm in order to provide gas gain.

---

[15] F. Sauli, "Principles of Operation of Multiwire Proportional and Drift Chambers," lectures given in the Academic Training Programme of CERN 1975–1976, CERN 77-09, May 1977.

[16] G. Baranko, et. al., "The Drift Velocity Monitor," HRS-198, Dec. 1980.

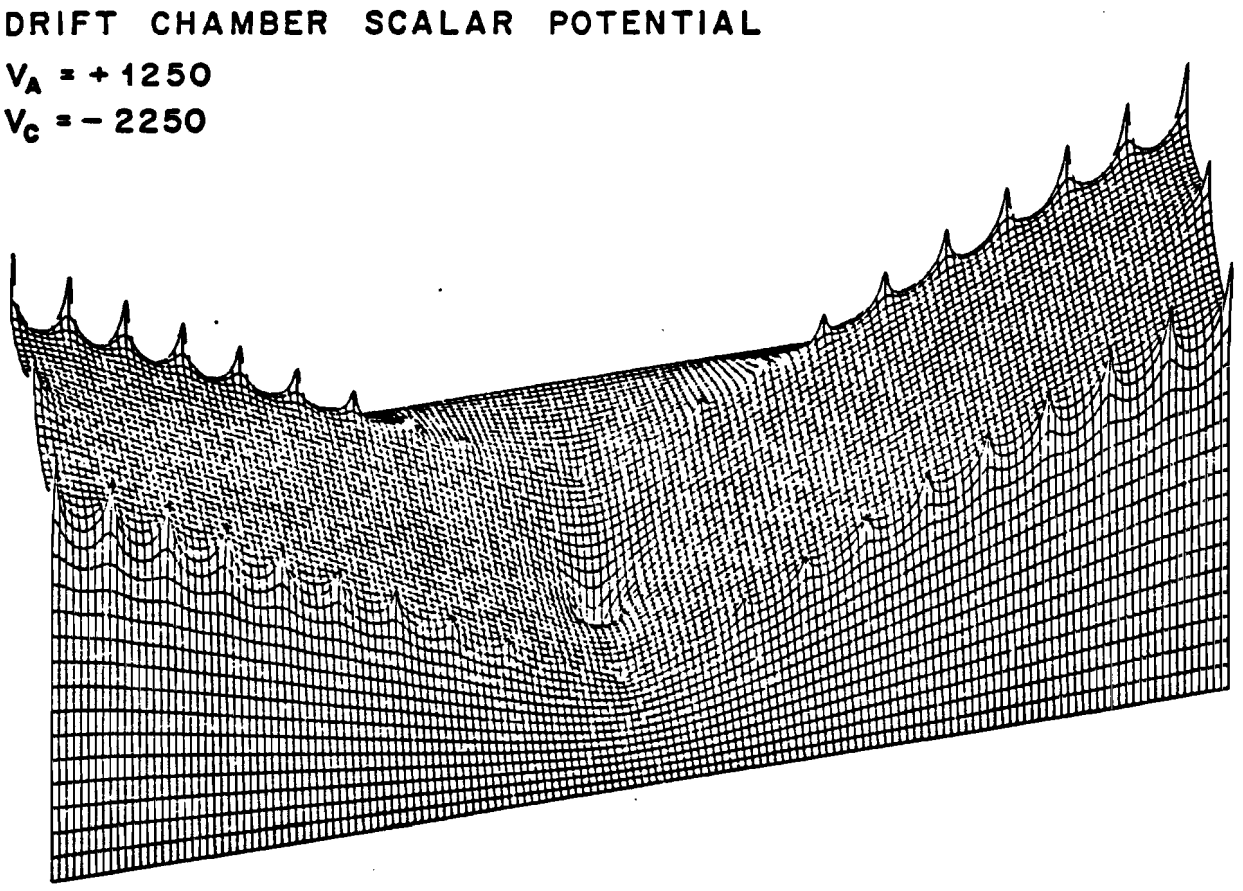

Figure 2.12 Three dimensional representation of the scalar potential in a drift cell. Note that the sign of the potential has been inverted in order to provide a clear view of the field.The spikes are due to the $1/r$ behavior near each of the field wires. Electrons literally *roll* down the slope at constant velocity and are collected at the anode wire (center). The ground planes force the potential to be zero at the front and back of the cell.

2.4.2.3 Operational characteristics

During the early running of E570 the chambers were filled with a 50/50 mix of Argon-Ethane. Due to the possibility of explosion (particularly in light of the nearby source of hydrogen) great care had to be exercised in using this gas. A worse problem proved to be the formation of polymer chains on the wires. The accumulation of small black particles on the wires degraded the high voltage which the chamber could hold before discharge. As a result it was decided to change to the gas developed and used by the High Resolution Spectrometer collaboration at SLAC.[17] This 89% Argon, 10%, carbon dioxide, 1% methane mixture had the benefits of being virtually explosion proof and of operating at voltages roughly 80% of those used for the Argon-Ethane mixture.

[17] D. Koltick, "Gas Studies in the Prototype Outer Drift Chambers," HRS-197, Dec. 1980.

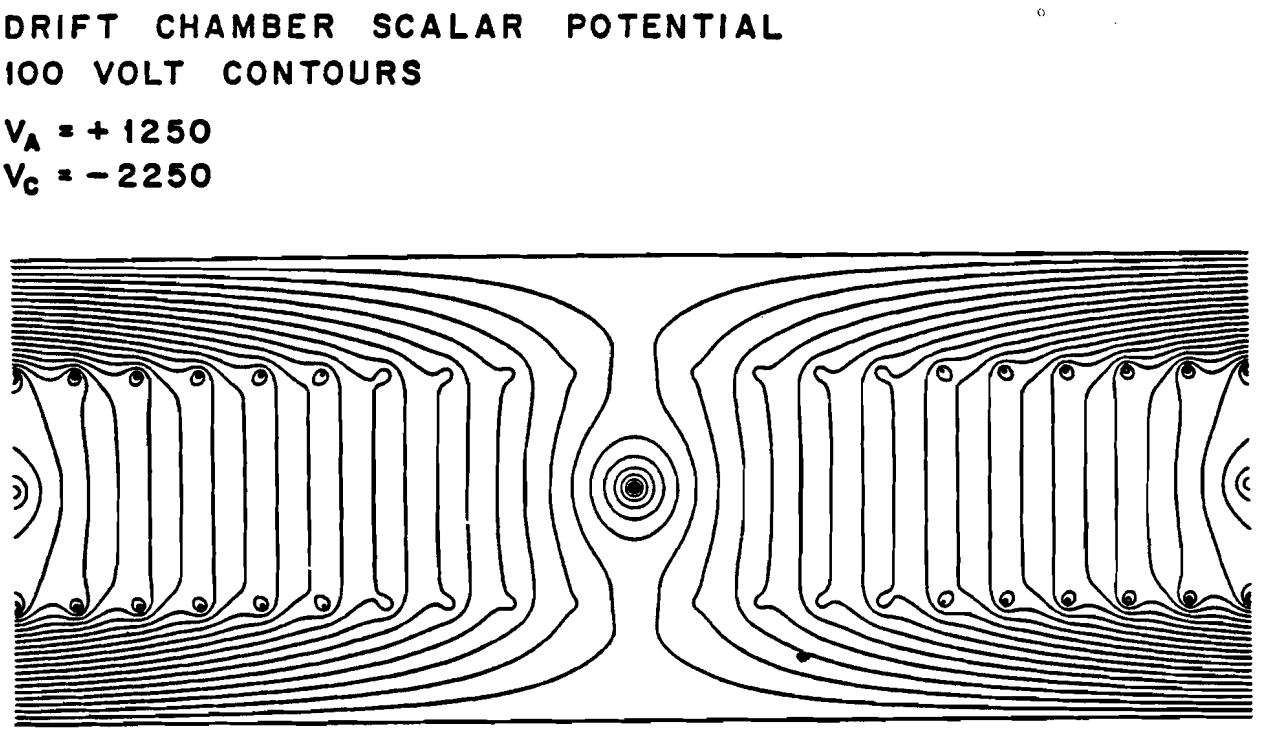

Figure 2.13 Equipotentials for the field configuration produced inside the E570 drift chamber cell. This is a contour plot of the field solution show in figure 2.12

In order to operate a drift chamber a balance must be found in a space defined by the chamber high voltages V_A and V_C, and the discriminator threshold for signal detection V_{TA}.. For a properly functioning chamber V_C is not a constraint and can simply be set to a voltage which will provide the proper drift field. V_A and V_{TA}. are however related in that they both concern the signal pulse hight: V_A governs directly the gas gain and V_{TA}. regulates what is called a hit and what is not.

A high voltage plateau curve for a single plane is shown in figure 2.15. This curve was obtained by illuminating a single drift cell with a test beam. A signal from an upstream beam telescope similar to MASTER GATE described above was ANDed with the discriminated output of a scintillator located just behind the active cell in the drift chamber plane. This coincidence was used to generate a gate of length 820 ns. This was ANDed with the chamber outputs and applied to a scaler to count the arrival of hits within the maximum drift time of the cell. The gate was operated in an updating mode in order to accept multiple beams within a maximum drift time. By also counting the total number of gates generated one was able to measure the efficiency of the plane.

While various effects limit the ultimate resolution of this measurement it is nonetheless sufficient for our purposes. We see in the curve that the chamber became highly sensitive at 1500 volts using

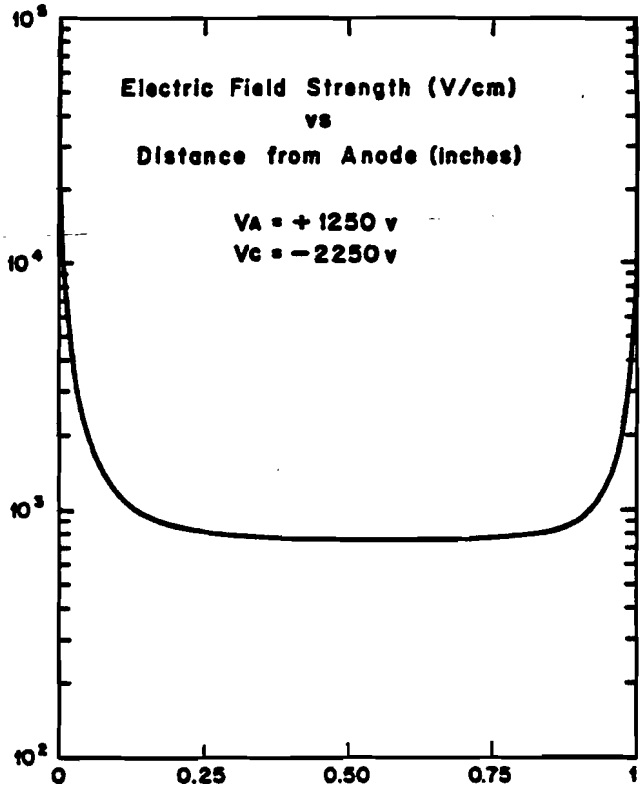

Figure 2.14 Electric field strength produced along the chamber center line.

Argon-Ethane (1200 volts for HRS gas). This sensitivity is seen to persist over a range of voltages.

In figure 2.16 we see a scan of the efficiency over a range of threshold voltages. At very low $V_{Th.}$ both chamber and amplifier noise are accepted as data giving rise to efficiencies larger than 1. Too large a threshold rejects valid pulses which fall bellow $V_{Th.}$. We observe a wide range of $V_{Th.}$ which accommodate efficient operation of the chamber. The $\epsilon(V_A)$ and $\epsilon(V_{Th.})$ curves shown are two orthogonal slices of the efficiency surface in $(V_A, V_{Th.})$ space. These particular curves are shown because their intersection was deemed to be the optimal point for operation.

2.4.3 The E570 dE/dx Detector

CRISIS presented an area of 1 m × 1 m to the beam and had a length of 3 m. Figure 2.17 shows a cross section of the chamber. We note that four distinct drift spaces were created by the interleaving of two sense planes with three cathode planes. The upper and lower cathode planes were solid sheets of metal, while the central plane was strung with wires to afford low mass. Figure 2.18 shows the details of the sense wire plane. Anode wires were separated by cathode wires in order to isolate the charge samples as they drifted toward the anodes. There were a total of 384 anodes in each sense plane. These were ganged in pairs to form 192 cells in each of the two planes.

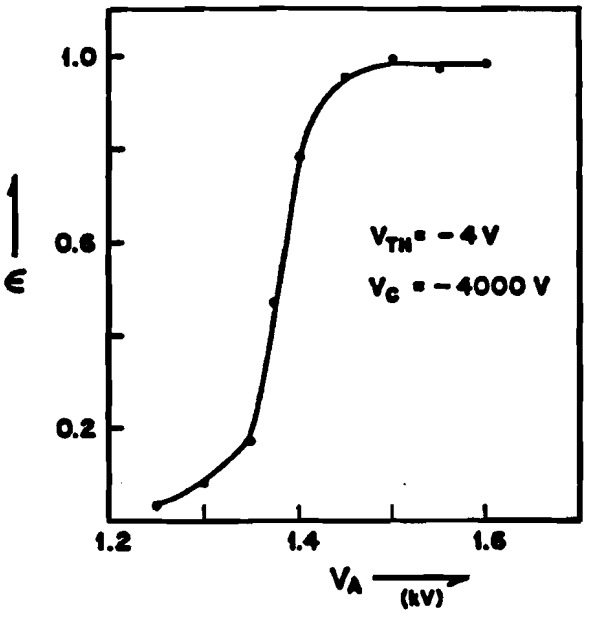

Figure 2.15 Efficiency of a drift chamber cell as a function of the impressed anodic voltage. The values ϵ are derived as is explained in the text.

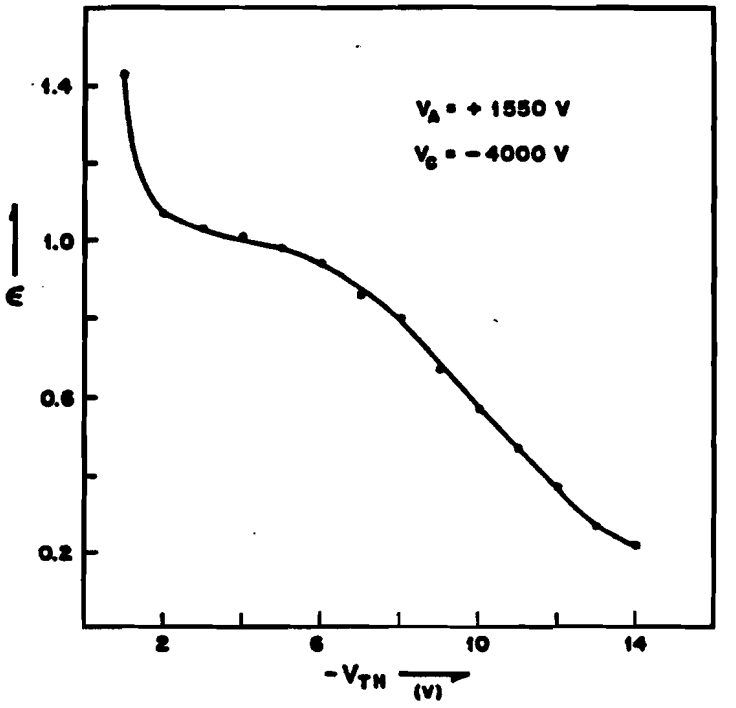

Figure 2.16 The variation of pulse detection efficiency with the threshold programming voltage V_{TH}.

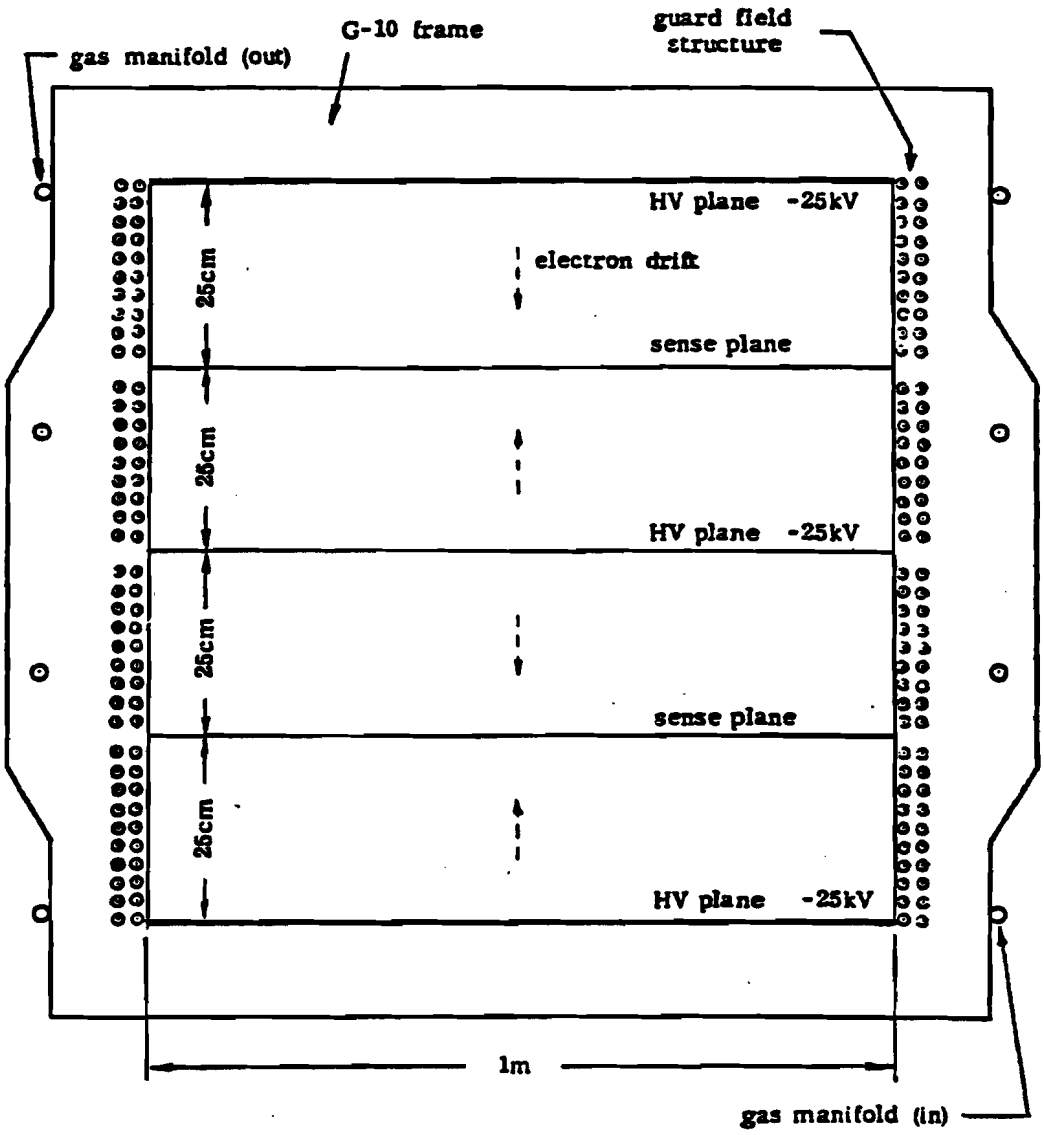

Figure 2.17 A cross sectional view of the dE/dx detector. (This figure and the next have been reproduced from B. F. Wadsworth, et. al., IEEE Trans. on Nucl. Sci. NS-26 (1979) 120).

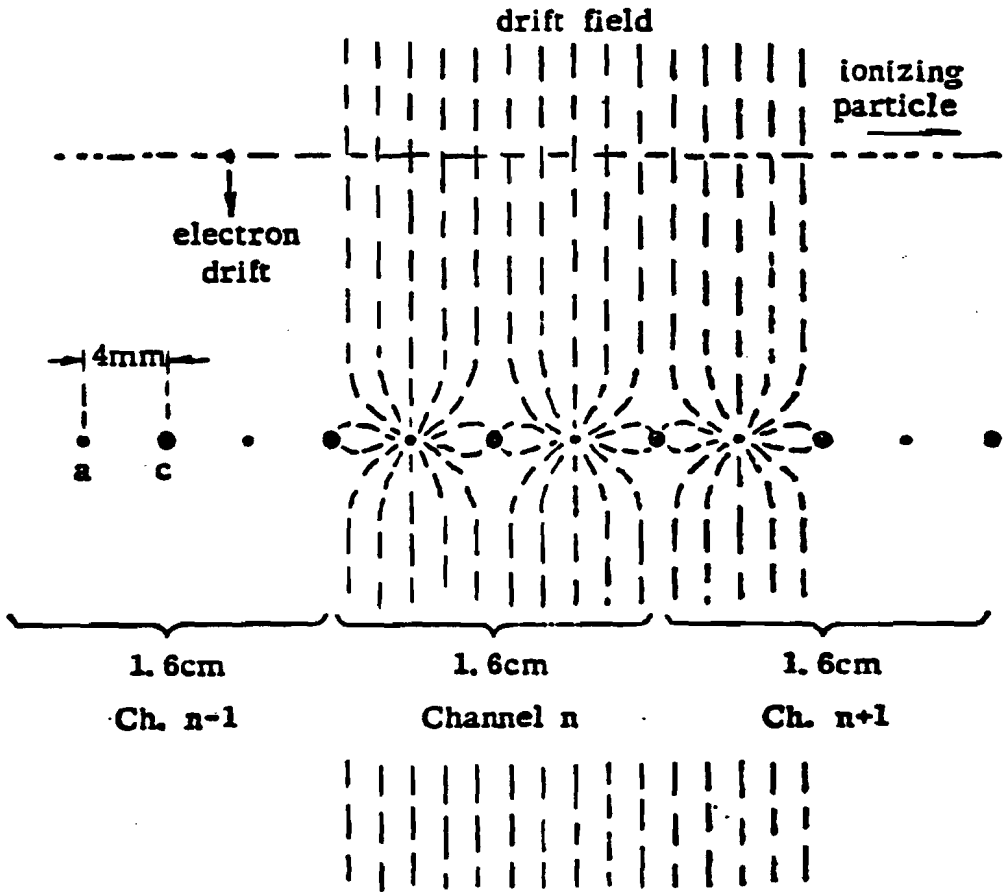

Figure 2.18 The sense plane structure of CRISIS. Note the affect of the alternating anodes and cathodes on the separation of the charge samples as they drift toward the wires.

The chamber was operated with a drift field of 890 V/cm. The gas was an 80/20 mix of Argon-CO_2 at atmospheric pressure. The gas was recycled and cleaned of oxygen[18] in order to prevent electron attachment during drift. The detector and its sub-systems are described at length elsewhere.[19]

2.4.4 The Forward Gamma Detector

The final element in the DPI was the Forward Gamma Detector (FGD). This device incorporated three distinct detector modules as well as a dedicated calibration system.[20] Photons initiated an electromagnetic shower in an active converter. A scintillator hodoscope was positioned at the apex of the shower in order to determine the impact point of the original γ-ray. The shower was then dissipated in a total absorption calorimeter.

The FGD is illustrated in an elevation view in figure 2.19.

2.4.4.1 Converter

The converter consisted of an array of 12 vertically and 12 horizontally positioned $2\frac{1}{2}'' \times 2\frac{1}{2}'' \times 30''$ lead glass (SF-2) bars. Each glass bar was viewed by a 56AVP photomultiplier. The two converter layers represented a total of 5 radiation lengths. The total energy deposition in the converter was 10% of the total.

2.4.4.2 Hodoscope

The hodoscope consisted of three planes of $1\frac{1}{2}$ cm $\times$ 1 cm scintillating rods set at the vertical and $\pm 45°$. Each of the 190 scintillators was viewed through a light guide by an RCA 931A phototube. Pulse hight analysis of the channels in each of three planes allowed determination of the shower centroid to within 4 mm in each view.

2.4.4.3 Absorber

The absorber consisted of a 5 $\times$ 5 array of $5'' \times 5'' \times 24''$ lead glass (SF-5) ingots. Each 24 radiation length bar was viewed end-on by an EMI 9628-R photomultiplier.

---

[18] D. Goloskie and T. Stoughton. "The CRISIS Detector: The Gas System," Rev. Sci. Instrum. 54 (1983) 60.

[19] A. Shapiro, et. al., "The CRISIS Detector: Characteristics and Performance," 53 (1982) 393.

[20] M. Heller, et. al., "Test Results of a 31 cm $\times$ 31 cm Lead Glass Electromagnetic Shower Detector," NIM 152 (1978) 379.
J. T. Bober and T. A. J. Frank, S. B. thesis, M. I. T., June 1977.
J. T. Bober, PhD. thesis, M. I. T., Aug. 1984.

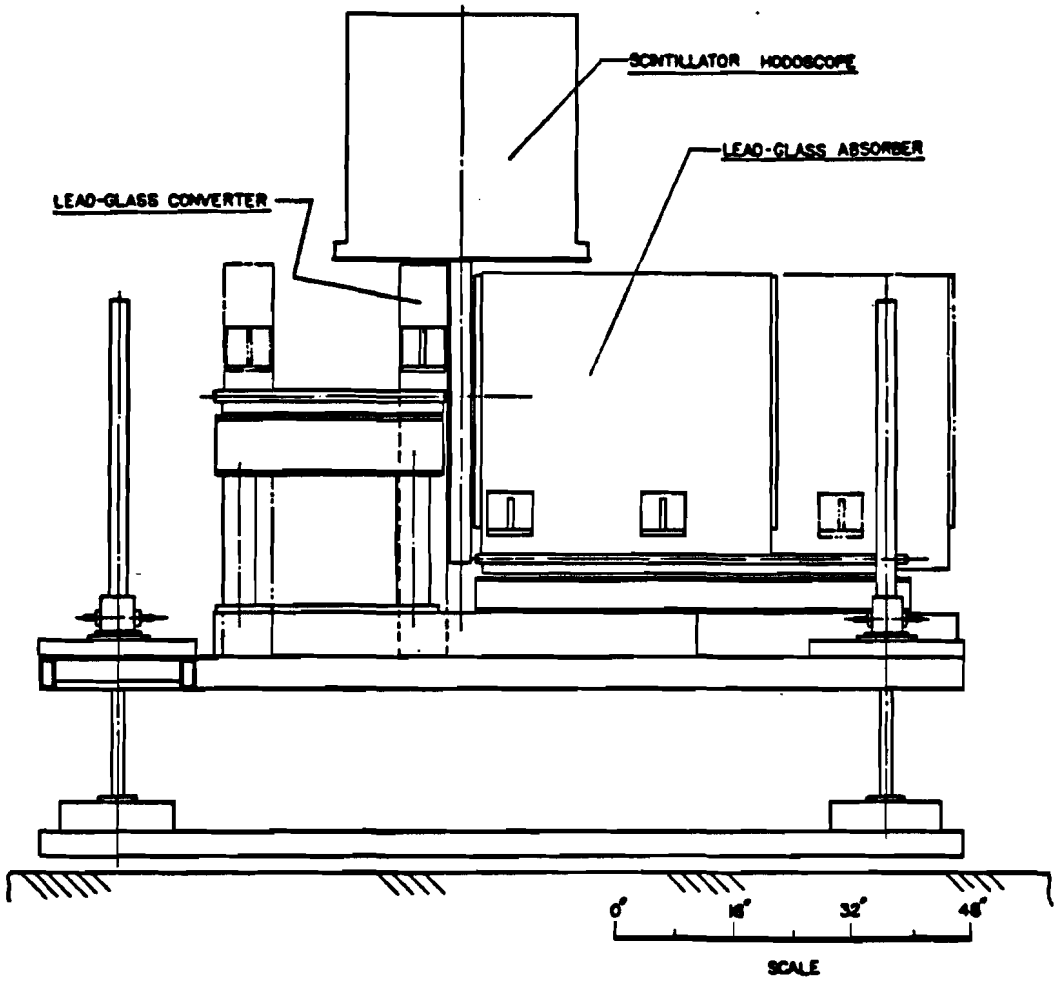

Figure 2.19 Elevation view of the three FGD components and their supporting frame. The broken lines indicate the module locations when pulled back for servicing.

Chapter 3

DATA ACQUISITION

E570 was able to capitalize on the results of other investigators to the extent that no detector physics development work was required to meet the experimental goals. With the exception of a recent formulation of ionization loss in gases this document will as a consequence forego any discussion of detector physics.

This chapter is devoted to a description of how detector outputs were recorded for later analysis. There is a fundamental dichotomy in the techniques available for the storage and transmission of information. At any given stage of transfer a signal may be in an analog or digital form. From the point of view of robust analysis the best form of storage for large amounts of data is in digital form due to its compatibility with high speed computers. With the exception of the bubble chamber information each of the detector signals was converted from its original form (be that time, charge, pulse height, or otherwise) to a final digital representation. The means of detection, transformation, and storage of these signals form the bulk of this chapter. Relevant details of the data acquisition electronics for each of the detector systems are presented. This is followed by a description of the integration of all the detectors into a standard on-line environment. Finally the system timing is presented.

3.1 DETECTOR ELECTRONICS

The inclusion of a bubble chamber in an otherwise electronic spectrometer had a strong impact on the overall data acquisition scheme. In particular the familiar sequence of triggered data logging was not possible. As a result the data generated by each beam in a ping had to be recorded whether it interacted or not. In such an environment the electronics were required to store the data for each time slot in a

ping and then transfer it to a host computer during the time between pings.

3.1.1 Proportional Wire Chambers

PWC wire hits were amplified and discriminated[1] at the chambers and differentially driven to a remote readout. Each wire was outfitted with a memory to record the presence or absence of a hit in each of up to sixteen time slots. At the end of a data taking cycle the memories were scanned for wire hits which were then passed to the host computer.

3.1.1.1 Latching wire hits

Hits were recorded by so called gating/storage/readout (or GSR) boards. Each GSR board served 32 wires. D type flip-flops were used to latch the wire hits. The trigger MASTER GATE was applied to the inputs Q and was advanced to the output D upon receipt of a hit pulse at the clock input C for active channels. The latch outputs were frozen in RAMs with the trailing edge of MASTER GATE. This resulted in a dead time of 120 ns, being the width of MASTER GATE.

3.1.1.2 Sparse data scan

Only a relatively few of the thousands of wires were struck during an event. Therefore a sparse data scan was undertaken at the end of each ping. A series of four CAMAC modules were used to perform the scan.

In its original implementation[2] the readout used only two modules to accomplish the scan under the direct supervision of the host via the CAMAC LAM function. Upon receipt of a start scan command a *control module* would begin a scan of the RAM file for data. The RAM outputs from sets of 8 GSR boards were multiplexed via *common buffer* (or CB) boards to form groups of 256 addressable wires. Each CB contributed one bit to one of two 24 bit *plane words*. In this way the plane word contained the hit/no hit state of a specified wire in each of the planes. (We note that certain of the plane word bits were used to record the discriminated outputs of the Čerenkov counter photomultipliers). The plane word bits were all ORed together by a *data module*. As the control module stepped through the wire addresses and time slots a LAM[3] would be generated if any plane word bit was asserted indicating at least one wire hit. The scan was then temporarily halted and the host would fetch the time slot, wire

---

[1] R. Downing, et. al., "Upstream PWC Chambers and Amplifiers," PHSC Newsnote #6, Aug. 1971 and #14, Oct. 1971.

[2] B. Wadsworth, "Upstream PWC Readout Electronics Group: Hardware design Approach," PHSC Newsnote #1, July 1971.
B. Wadsworth, "Upstream PWC Readout Electronics Group: Dataway Commands Required for Readout Electronics," Newsnote # 17, Nov. 1971.

[3] LAM is the CAMAC acronym for *look-at-me*. It is used to generate a computer interrupt for the user side of the interface. The response of the host was then determined by a (dynamically defined) graded LAM word.

address, and plane words from the control and data modules in order to uniquely identify the wire hit(s). The scan would continue in this fashion until each wire and time slot had been tested for data.

The use of interrupt driven data transfers from the PWC readout was not possible in E570 due both to the volume and variety of data to be handled. This difficult mismatch in hardware constraints was solved by the use of distributed intelligence. A microprocessor[4] assumed the former role of the host in off-loading plane words from the control and data modules.

At the end of a ping the PWCRO μPROC was instructed to perform the data scan. Thus leaving the host free to service the other detectors. As data was located by the μPROC it was stored in a Type 5700 memory module and the scan continued. Upon completion of the scan a DATA VALID flag was set in the memory. This *handshake* allowed the host to read the PWC data as soon as it was ready to do so. The transfer was performed by direct memory access (DMA) at a rate of 2MHz. Hence the entire PWC data could be retrieved by the host in less than 1ms.

3.1.2 Drift Chambers

As pertains to the problem of digitizing drift chamber time data there is more at play than the time measurement problem. The most prominent consideration being the requirement of hundreds of channels of time data which must be serviced simultaneously. This single constraint when converted into total system cost limits one to a temporal resolution in the area of one to ten nanoseconds. Fortunately this resolution proves to be adequate when we consider the drift velocity and longitudinal diffusion characteristics of even the best gases.

The requirements of fixed target experiments demand many other features of the electronics design. Due to the interaction multiplicity and the center of mass motion in the lab frame the density of tracks in the *forward jet* can become rather high. Hence each channel must be able to record the passage of several tracks through its drift cell. The TDC (for Time to Digital Converter) recovery time must allow successive hits to be resolved even at small spatial separations. The nature of the bubble chamber beam spill also adds to this multi-hit requirement as many beam tracks will enter the spectrometer during a bubble chamber expansion.

The above considerations lead one to a design with two basic timing or memory cycles. The first (data taking) cycle is the rapid recording of wire hit data as it arrives from the chambers. At this stage it is important that the TDC can store data and recover for the next input with a minimum of delay. The electronics at this phase of operation are under the control of the experimental trigger. The second (read out) cycle is in fact a play back at a slower rate of the data which was stored during the

[4] The PWCRO microprocessor was configured much the same as the DCRO microprocessor. This as well as the memory module referred to in the text are described at length in §3.1.2.4

data taking cycle. This stage will necessarily be concerned with the reformatting and transmission of information stored with such haste during the data taking cycle. During this phase the electronics may be supervised by a host computer or some other intelligent controller.

It is interesting to note in advance that the design to be discussed below takes data at a rate more than one hundred times faster than is used for reading out.

3.1.2.1 Choice of time digitization technique

In an early study of the use of drift chambers in the FHS Wadsworth and Marcato[5] suggested a new approach to handling digitized information from drift chambers, which they called Beam Time Encoding (BTE). This scheme is characterized by the recording of all drift times using a real time clock referenced to the beginning of the beam spill, and an additional channel of electronics to record the arrival time of each beam within the spill. These authors concluded that along with a proper sorting algorithm BTE could provide useful drift time information even at high beam rates.

In a study of the specific form of the TDC[6] two possible techniques in each of two distinct designs were considered. Each design involved a relatively slow system clock ($\nu = 40\,\mathrm{MHz}$) combined with an interpolation scheme to achieve 2 ns time resolution. The interpolation schemes studied were[7]

- straight counting
- vernier
- capacitor with linear discharge
- capacitor with direct encoding.

The authors recommended the digital straight counting design for reasons of simplicity, cost, and circuit homogeneity.

The major drawback of this design is the necessity of a 500 MHz interpolation clock and associated scalers. The final design benefitted from the modularity of the original design study. The use of delayed phases of the system clock to establish a Gray code for interpolation was, however, ultimately chosen

---

[5] B. Wadsworth and P. Marcato, "A Drift Chamber Scheme for High Event Rate, High Multiplicity Applications," APC Engineering Note 76-1.

[6] P. Marcato and B. Wadsworth, "Implementation of Beam Time Encoding for Drift Chambers Using Various Digitizing Schemes," APC Engineering Note 76-2.

[7] The reader who is unfamiliar with these circuits will find their full documentation in the previously mentioned report. As an alternative the basic concepts involved are to be found on pp. 621-623 of P. Horiwitz and W. Hill, "The Art of Electronics," (Cambridge: Cambridge University Press, 1980).

for production.

If one need not consider practical matters the digitization of isolated time events is very simple. One gates a clock wave train into a scaler for the time period in question and the final count is the time. When many intervals need be recorded one strobes the scaler outputs into a memory file and bumps the address each time an event takes place. Later interrogation of the memory will reveal the sequence of time events. This simple approach is in fact quite acceptable for slow speed applications. But when the required least count is 2 ns the clock frequency is 500 MHz and problems arise due to the significant amount of RF noise produced by the electronics. The accepted design had the benefit of much lower clock frequency (62.5 MHz) and consequently fewer worries about radiant energy. Furthermore this design was compatible with the availability of components. Most importantly the idea of writing data directly into RAM had to be replaced as no available memories could achieve sub-nanosecond write set-up times. One was capable, however, of latching data *on the fly*. This asynchronous storage was used to hold data only long enough to write synchronously into the best RAMs available. This write cycle introduced the limiting dead time of the TDC.

3.1.2.2 Chamber electronics

We move now to the topic of signal extraction from the drift chambers. As is illustrated in figure 3.1 the planes were configured so that the pair of grounded field shaping wires and their intervening sense wire formed a simple three wire transmission line. (The reader may also wish to refer to figure 2.11). Both ends of this system were terminated by RC networks which had been adjusted to minimize signal reflection. Pulses were capacitively coupled out into a shielded 18″ twisted pair. Upon reaching the amplifier the line was clamped and terminated. A 100 Ω terminating resistor was used to both match the impedance of the short cable and develop a voltage at the high impedance amplifier input. The bipolar diode clamp used two 1N4005 to provide peak surge protection to 30 amps. This was required by intermittent arcing and discharge of the high voltage.

Pulse detection was accomplished with a commercially available monolithic amplifier/ discriminator.[8] The overall design is shown in figure 3.2. We note that the MVL100 was used in conjunction with exclusively passive components. The fully differential amplifier had a fixed gain of one hundred. After amplification the signal pair passed through matched pulse shaping networks which differentiated the signal and presented it to a programmable comparator. The pulse shaping was useful in that the resulting bipolar wave form had both an increased rate of rise and a more rapid recovery from the point of view of pulse pairs. With the threshold programming voltage as determined in §2.4.2.3 the discriminator fired for pulse heights greater than 800 μV at the amplifier input. The discriminator output was fed to a non-retriggerable monostable which was configured to produce a fixed 20 ns output

[8] Model MVL100 from LeCroy Research Systems Corporation, 700 South Main Street, Spring Valley, New York 10977.

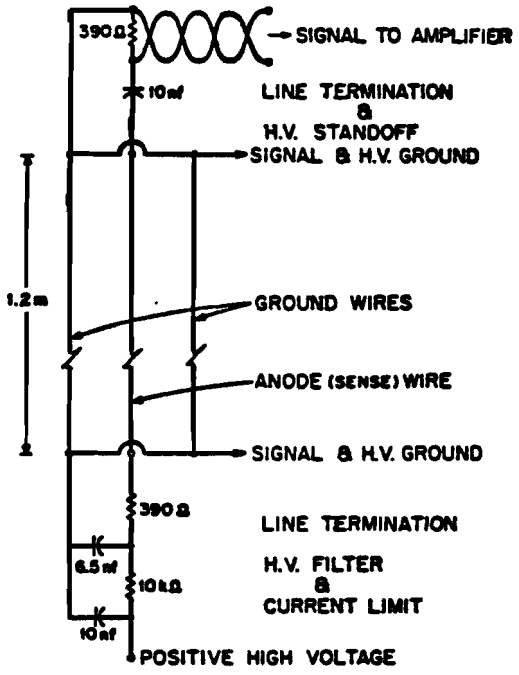

Figure 3.1 Drift chamber signal circuit.

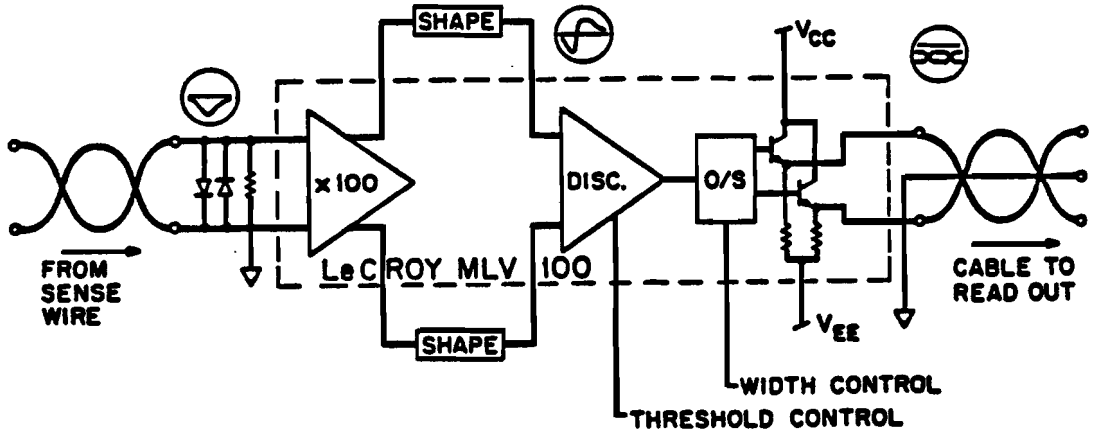

Figure 3.2 Configuration of the drift chamber AMPSEND.

pulse. The differential output drivers provided standard ECL levels.

The MVL100 has an input-output time slew of less than 1.5 ns.

In the design implementation care was taken to protect the MVL100 from external noise. This is especially so as early testing showed it prone to uncontrolled oscillation due to a local FM radio station. To this end the entire power supply system was designed to have a well defined, unique ground. The

ground point was chosen to be the read out relay racks in the electronics port-a-kamp. The chamber high voltages as well as the amplifier power were cabled out to the experimental floor from this point. Amplifier power was distributed and regulated[9] locally at each drift chamber plane. Each amplifier channel was provided with inductive and reactive filtering at each power input to reduce feed through.

Each AMPSEND channel drove a 140′ (nominal) length of twisted pair with drain wire. Each plane had its own cable of 27 pairs accommodating the twenty four cells, leaving three spares. Within the cable each twisted pair was wrapped in a conducting foil. Each of the 9×27 pairs was timed, trimmed, and timed again in order to achieve among the channels a uniform propagation time delay to better than ± 100 picoseconds.

Although twisted pair cable has excellent common mode rejection properties its time resolution capabilities are impaired by its limited band width. Figure 3.3 reproduces signal scope traces taken at the input and output of a typical cable. We observe noticeable distortion of the signal due to loss of high frequency components. The dispersion of the cable does not prove to be a major cause for concern as its contribution to time slew is estimated to be less than ± 400 ps.

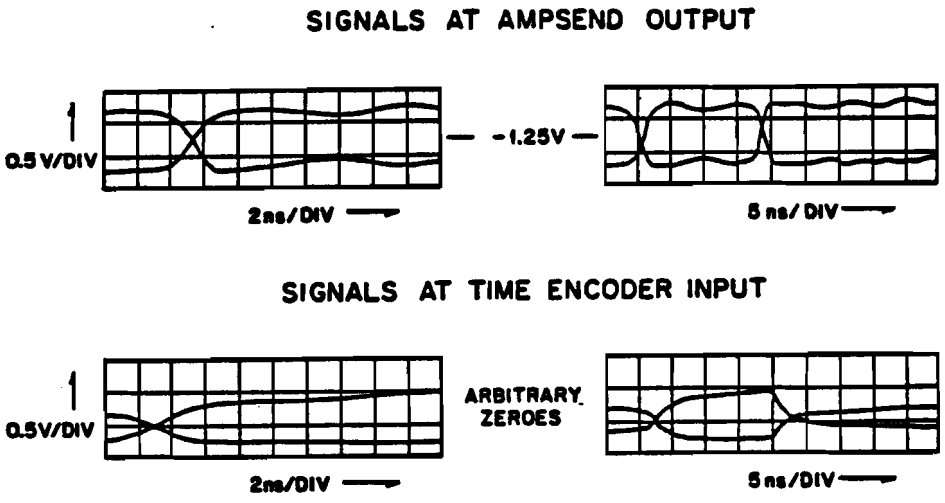

Figure 3.3 The affects of limited cable bandwidth on drift chamber signal pulses.

3.1.2.3 Conversion and fast storage

The heart of the TDC system was a set of 57 circuit boards referred to as time encoders. The time encoder cards were fabricated using the multi-wire technique in order to achieve circuit interconnections

[9] Using hybrid voltage regulators of the LAS-2000 series from Lambda Electronics, 515 Broad Hollow Road, Melville, New York 11746.

with 50 Ω impedance. The reason for this extreme care is apparent when one realizes that typical rise times on this board have spatial extent comparable to the length of wires between ICs! In point of fact each wire run on the board is considered to be a transmission line with an impedance that is matched by a single pull down resistor at the end of the line.

Each encoder was capable of storing 32 data hits. The on-board memory section was addressed in common by the four data channels serviced by an encoder.

The front end of the time encoders used ECL circuits of the 100*K* family in order to exploit their sub-nanosecond rise time. Signal inputs to the time encoders were capacitively coupled in from the cable. Aside from DC isolation this scheme allowed the adjustment of the differential cross over point by a resistive divider controlling the baseline on one side of the complementary line receiver inputs. This freedom of adjustment became invaluable during data taking. Due to an unresolved cause the AMPSEND voltage swing became skew when driven to a time encoder. In order to overcome this problem each channel was balanced in an effort too achieve the least time slew and greatest noise immunity. This procedure and in fact any adjustment of the input cross over point has as a consequence a change in the overall propagation delay time. These effects were not accurately measured at the time the inputs were balanced and although the shifts could in theory be found by software no effort to do so has been undertaken. The size of such delay shifts are in any case insignificant compared to other sources of dispersion.

Once on the board and regenerated the wire hit signals were sent in a single-ended fashion to the phase latches to be described shortly. Two other signals were presented to the time encoders during a data taking cycle, both of which were generated by the system clock. Of these signals ENCODE simply indicated that the data inputs were valid and should therefore be recorded in the RAMs. The other signal CLOCK was the system clock itself. Both of these signals were generated by MASTER GATE and fanned out to each of the encoders via matched coaxial cables. The clock was started by synching MASTER GATE to a continuously running crystal oscillator. CLOCK was straddled by ENCODE so that the encoders were reset and active prior to the arrival of the first clock pulse. The train of clock pulses (referred to as a burst) was fixed to a number of cycles which equaled the maximum drift time expected from a cell ($\approx$ 500 ns) plus a margin. The clock burst operated within an updating scheme so that data for two beams arriving within an ENCODE cycle would be fully recorded.

The encoders used another differential line receiver and resistive divider in order to remove any skewness induced in the clock waveform in its transmission. Once on-board the 16 ns clock was delayed in intervals of 2 ns in order to create a Gray code for interpolation. At design time active delay lines[10]

[10] Such as the fixed and programmable logic delay lines produced by Engineering Components Company, 3580 Sacramento Drive, San Luis Obispo, CA 93401. Various members of their PECL series of hybrid DIPs were used in test fixtures.

with sufficiently fine adjustment were not available. Thus in order to create the precise delays needed a special plug in module was created which contained a series of RG-178/U coaxial cables. This low profile module (called the delay line package or DLP) was fitted with pins compatible with the hole-tites[11] used on the rest of the board. This set of pins provided both the electrical contact and sole physical support for the $3'' \times 4\frac{5}{8}'' \times \frac{3}{8}''$ G-10 DLP. Each encoder had its delay lines trimmed to provide the correct delays at its own latches. This procedure removed chip dependent time delays and guaranteed the phases were correct to ± 100 ps at their most critical point.

The concept of interpolation using a Gray code is illustrated in figure 3.4. The four clock phases create a revolving bit pattern (...,0000,0001,0011,0111,1111,1110,1100,1000,0000,...) at the inputs of a fast latch. Also present at the latch was a train HCF of 32 ns period derived by dividing the clock by two. The final signal which was latched (DF) was derived from ENCODE and served to identify the channel with data present. The latch was a hex D type flip-flop (100151). The data signal formed the flip-flop Common Clock input. Consequently a hit would freeze the state of the inputs Q_n on the outputs D_n.

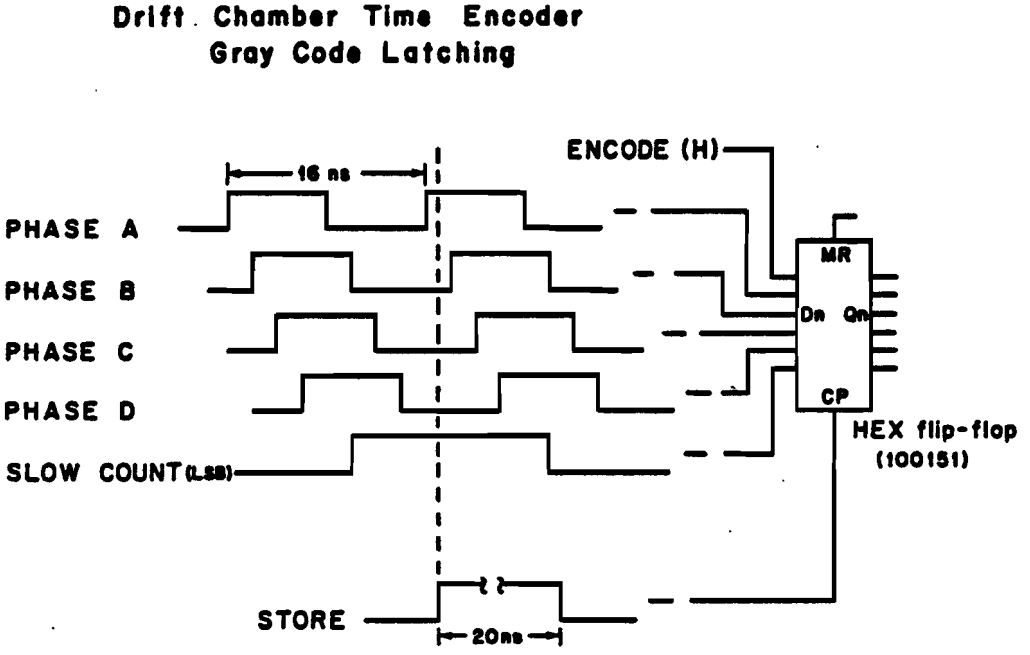

Figure 3.4 The time encoder function of Gray code latching.

On Phase C of the clock cycle the OR of the latch DF outputs was tested to determine if any of the four channels had data recorded. If so a write was initiated to the RAM file and the latches reset. Phase

[11] A hole-tite is the miniature contact assembly which is press fit into the plated through holes of a multi-wire board. These contacts allow the insertion and removal of ICs as well as other components on the board.

C was used as this timing guaranteed the clock scaler outputs SLOW to be quiescent during the write strobe. Due to finite rise times and cross chip propagation delays it is possible that a STORE pulse could arrive at the latch just prior to Phase C and have the data present test fail. In this case the clock count stored in the rams would be incorrect by the one clock cycle which had elapsed while waiting for the next Phase C test. This sort of error is compensated for by the latching of the least significant bit of SLOW, namely HCF. Since the latch is asynchronous it will always contain the correct LSB of SLOW. Later examination of the data will then allow one to reconstruct the correct time by comparing the LSB of SLOW and the latched HFC. If they match then the data was stored during the clock cycle in which it occurred. If, however, the two bits do not match then slow must be decremented by one to reflect the timing error.

Due to this RAM write cycle the common channel dead time falls in the range of $17\,\text{ns} \leq t_d \leq 33\,\text{ns}$. The minimum being determined by the time to latch reset after data detection and writing.

At the end of a data taking cycle ENCODE falls, locking out any further data from the chambers. This insured that only event related data was maintained in the RAMs.

In order to service the 216 drift chamber cells 54 time encoders were needed. An additional encoder was used to record the *beam time* (see §3.1.2.1). The signal BEAM TIME was created by delaying with cable MASTER GATE.

3.1.2.4 Data scan and transfer

After each bubble chamber expansion the data in the encoder RAM files were transmitted to the host computer for recording on magnetic tape. To achieve this transfer in an efficient manner distributed intelligence was used to effect a data scan which left the host free to oversee the other detector readouts. A microprocessor was used to contact each of the encoder cards and transmit their data to CAMAC memories. The use of these storage modules allowed the host to access the drift chamber data via CAMAC DMA at the end of a read out cycle.

An 8*X*300 microprocessor[12] was configured on a wire wrap board with program memory, a bidirectional 8-bit bus, and a system clock of 450 ns period. The 8*X*300 finds frequent application as an intelligent peripheral controller as it is capable during a single instruction cycle of reading an I/O register, operating on the data, and writing the result to a distinct I/O register.

Through its I/O registers the μPROC could address a total of 77 control and data lines (see figure 3.5). As the processor was implemented entirely in TTL contact with the ECL encoders was accomplished by special interface cards located in each of the readout crates. On the CAMAC side the μPROC could

[12] Manufactured by the Signetics Corporation, P. O. Box 9052, 811 East Arques Avenue, Sunnyvale, CA 94086.

sequentially write data into $2k \times 16$ bit RAM files, one for each DC plane. In addition the processor had two other important communications lines. One was used to initiate the data transfer while the other locked new data out of the encoders while the processor was busy during readout.

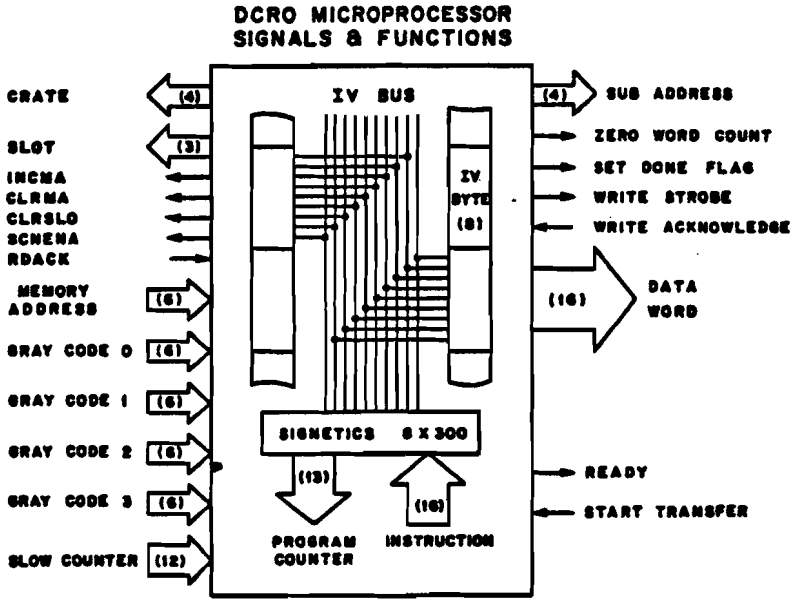

Figure 3.5 The drift chamber readout microprocessor configuration. Signals to the left are on the time encoder side. Those on the right are related to the CAMAC side and the trigger.

Upon receipt of a start transfer signal from the host the DCRO μPROC began a pass through its data acquisition program. Each crate and slot in the system was contacted in sequence. First the number of hits recorded by an encoder was retrieved. Then for each of the four wires serviced by the encoder the RAM file was scanned for hits on that wire. When data was found the SLOW clock and HFC were compared as described above. A corrected course count was then merged with the interpolation count and sent to the appropriate memory. After the entire scan was finished the CAMAC DATA VALID flags were set in each of the memories and the encoders cleared for the next data cycle

The 16 bit words written to CAMAC were of two types, namely *status* and *data words*. The status words were used to delimit the 15 bit data words. The status words contained information such as crate, slot, and wire number. They were further used to report hardware failures such as no response from an encoder or invalid Gray codes. The data words of course contained the clock count in units of the 2 ns least count.

A function diagram of the Type 5700 memory[13] is seen in figure 3.6. As far as data throughput from microprocessor to host was concerned it was a FILO memory. In addition it could be used as a RAM from the host side. Data could be written or read at rates up to two million 16 bit words per second.

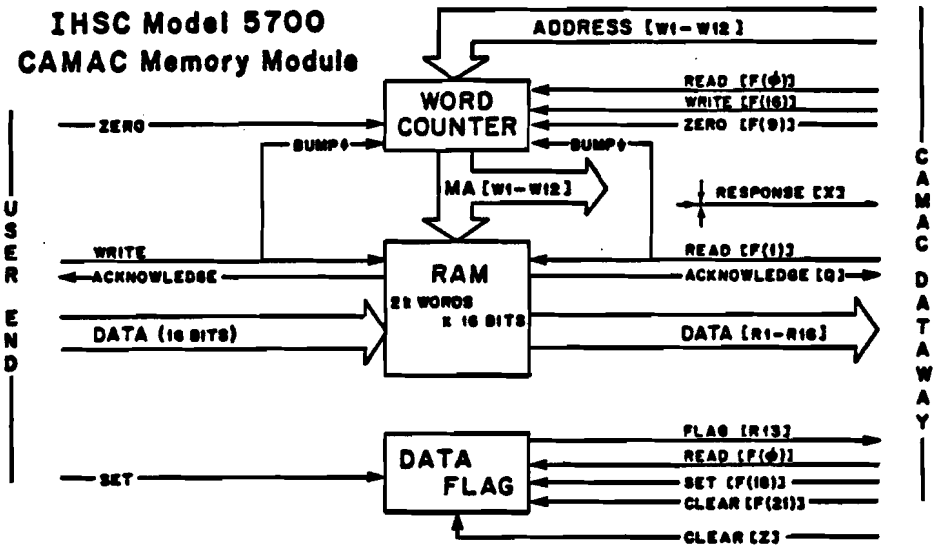

Figure 3.6 Signals and functions of the type 5700 CAMAC memory. The user side refers to the DCRO microprocessor. (redrawn from ref. 13).

3.1.2.5 System configuration

The readout electronics were organized at the level of the wire chamber plane. A total of nine electronics *crates* were used to hold the encoders for each plane separately. A tenth crate held the microprocessor. Communications were carried by a 64 conductor open collector TTL bus. Although the 35' bus was pulled-up at both ends it proved incapable of reliable operation. As all the signals were sent in a single ended fashion the edge sensitive lines (such as increment memory address) were highly susceptible to cross talk induced errors. In point of fact when an encoder was enabled for readout the noise generated by the turn on of up to forty one lines invariably corrupted the data by forcing the memory address to overflow. In order to compensate for this a series of one-shots were patched onto the the interface card. These monostables were used to both generate unique pulses when needed and to lock out the noisy lines when some other function was in progress. This as well as the application of simple timing considerations within the microprocessor program provided faultless communications with the encoders.

The Type 5700 memories were fabricated in double width CAMAC modules. Each unit contained

[13] Garry H. Shulze, "The IHSC Model 5700 CAMAC Memory Module," APC Engineering Note 83-2/DC, revised from Dec. 1981.

three independent RAM files as distinct sub-addresses. Three modules were used so that the data from a given plane could be stored in its own file. Communications were carried differentially by a 50′ twisted pair cable.

The various levels of integration of the drift chamber readout system are illustrated in figure 3.7.

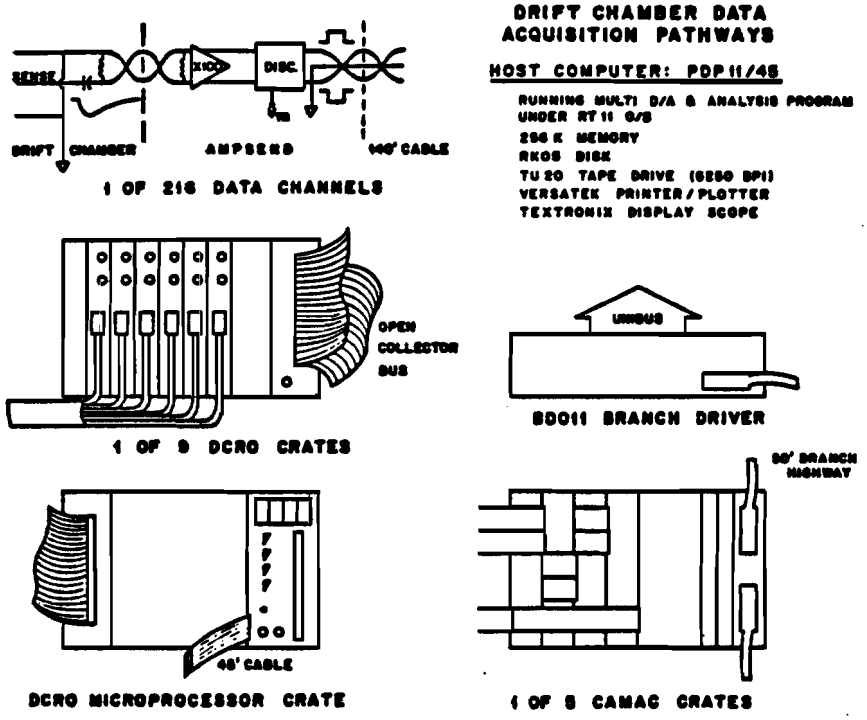

Figure 3.7 The various levels of integration of the drift chamber data from the wire signals to the host computer.

Gating and various other electronics were situated in a NIM bin mounted in the three relay rack system. the system clock and its fan out logic were distributed among the various readout crates.

The readout crate backplanes provided power as well as signal distribution. Each slot had its own hard wired address. All the ECL lines were pulled down with 100 Ω to −2 volts at either end of the bus in order to preserve signal quality.

3.1.2.6 Testing

Prior to their commissioning the encoder boards underwent a variety of tests. The microprocessor was used to test the RAM addressing at high rate from both the data and readout sides. A specially built test rig was used to certify the overall functioning of each board. Data hits of know time delay were deposited on the board and read back by an operator. All the data and status lines were visually displayed and

the data writing and read out were under manual control. This allowed for effective location and trouble shooting of defects.

With the full nine crate system in its running configuration a final high level test was performed. Under the control of the host computer data was generated, read out and recorded on magnetic tape. By using a FAD (fast analog delay) BOX[14] it was possible to deposit know time data in the encoder memories. The FAD BOX is a CAMAC programmable delay line with a least count of 250 picoseconds and a range of delays up to 1024 nanoseconds.

The testing scheme is illustrated in figure 3.8. Upon receipt of an interrupt the host toggled a CAMAC output register in order to start the drift clock and thereby initiate a standard data taking cycle. A phase of the clock was delayed by the preprogrammed FAD BOX and fanned out to the encoders as data hits. After a short delay the host instructed the processor to unload the data to the CAMAC memories. During the read out the host Q-polled the last type 5700 DATA FLAG until it was set valid by the processor. The data was then buffered to tape. The final step in the test cycle was to increment the FAD delay (in the present case by two of its least counts). In this way a series of interrupts swept through a range of time delays.

The lower part of figure 3.8 shows the result of just such a sweep for a typical encoder. We observe that the entire system has responded as expected. Note that this covers a range in delay of 32 ns (16 DC least counts, 128 FAD steps) or two full clock periods. Thus the processor has decoded the half cycle flag (HCF) information properly.

The type 5700 memories as well as the data pathways between the microcontroller and the PDP-11 were tested as follows. Under the overall control of the host a sequence of predetermined bit patterns was written into the CAMAC memory by the microprocessor. Upon completion the host read the data both by DMA and the random access feature. The retrieved data was then evaluated for bad bits. The processor was then instructed to write a second bit pattern sequence and so on. Once the system had been fully debugged this diagnostic test never failed, even when run for extended periods.

3.1.3 CRISIS

In order to be effective in the identification of particles CRISIS had not only to measure the charge deposition in each cell, but also the time of arrival of each charge sample within a cell. The reason for this is clear. Since many secondaries will in general enter the detector simultaneously one must have the ability to associate each charge sample uniquely with its parent track. The measurement of the arrival time of each packet of charge provides just this ability.

---

[14] The author expresses his gratitude to the Fermilab PREP staff for the extended loan of this in-house module. For details of the design see NAL drawing 2530-ED-47900, Nov. 1976.

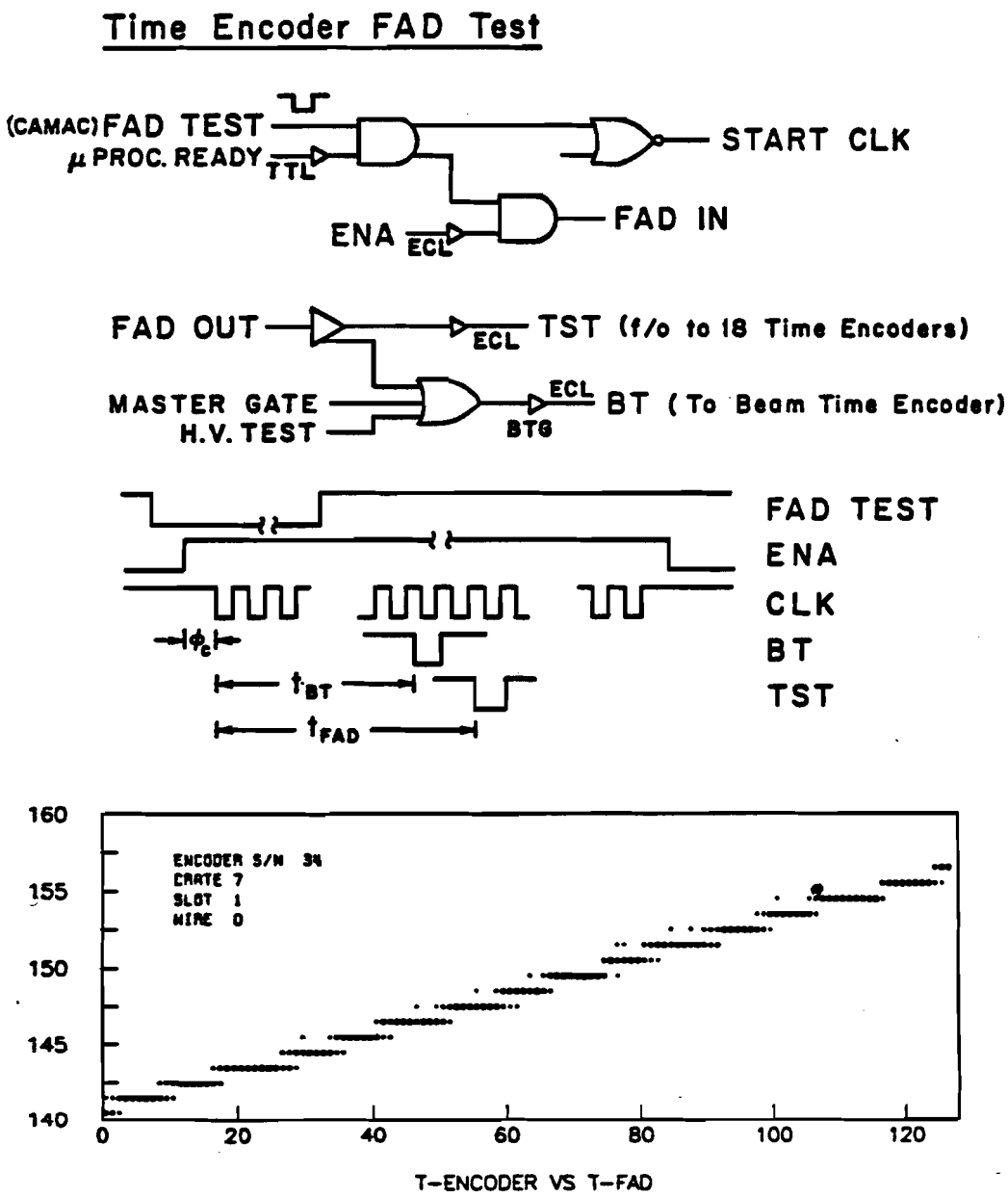

Figure 3.8 Gating used to store know time data in the time encoder memories. At the bottom we see a typical test result. The size of the data points indicates the frequency of occurrence.

Because its maximum drift time ($\approx 6.5\,\mu s$) was long compared to the time over threshold of a signal pulse ($\approx 250\,ns$) CRISIS was required to be a self triggered device. Further a multihit capability was required in order to store data for each of the several event related and spurious tracks arriving during the maximum drift time.

Given the choice of a Wilkenson ADC, as opposed to say a *flash* ADC[15], some form of analog storage was required. That is to say the charge samples for each channel had to be stored individually until the end of ping when they would be sequentially digitized.

3.1.3.1 Preamplifier

The preamplifier accomplished three important functions. A transresistance amplifier was used to enhance the low level wire signals. Pulses were then shaped to reduce the extent of the $1/t$ tail characteristic of the gas gain process. And finally the signals were differentially driven from the chamber to the remote storage and readout system.

3.1.3.2 Real time storage

The *drift clock* was operated at a frequency of 20 MHz. As a result the recording of drift times was simply a matter of strobing the outputs of a scaler into successive levels of a RAM file. The arrival times of beams were recorded in a special data channel. Beam times were recorded using the drift clock which would start and stop for each time slot during the course of a ping. Beam times were also recorded using a so called *run clock* which recorded the real time of arrival of beams within a ping. The electronics were designed to record the time over threshold as well as the arrival time of each pulse.

3.1.3.3 Data conversion and readout

Individual charge samples were stored on capacitors. In order to achieve a dead timeless system a dual analog bus was used. This allowed one bus to take data while the other was being restored to a quiescent state. The carefully matched capacitors were fed from the bus by FET analog switches (SD5000). The integrity of the switches as well as the elimination of stray capacitance along the data path were important to the faithful recording of the charge data. Of equal importance was the generation of a proper charge *integration gate*.

Once on the storage cards chamber signals were admitted to a lumped component analog delay line. This provided a 120 ns delay during which time a discriminator could detect the rising edge of the input signal. From this an integration gate was started. The gate admitted the delayed pulse to a capacitor. The integration gate was held valid until the discriminator input fell below an independent

[15] See for example p. 632 and pp. 415–16 of P. Horowitz and W. Hill, "The Art of Electronics," (Cambridge: Cambridge University Press), 1980.

turn-off threshold plus a fixed *post delay* of 120 ns. In this way the delayed pulse was cleanly bracketed by the integration gate.

3.1.4 Forward Gamma Detector

The problem of recording photomultiplier signals from the FGD is of a similar nature to that posed by CRISIS. The solution was, however, of a significantly different nature. This system used a series of distinct purpose modules rather than a single integrated storage and conversion system. The phototube signals were integrated on the capacitors of ABMs[16] (analog buffered memory). Each data channel was capable of recording a total of twelve pulses. At the end of each ping the ABM charges were multiplexed via a CADAC (CAMAC analog data acquisition control) to the inputs of commercial ADCs[17] to be digitized.

3.2 CAMAC INTERFACE

Each of the read out systems was ultimately interfaced to a CAMAC (computer automated measurement and control) system.[18] E570 used a five crate single branch configuration. The CAMAC system is capable of a variety of synchronous and asynchronous operations. Principle among these is the ability to transmit and receive 16 bit data words at a rate of 2 MHz.

Fermilab provided a BD011 branch driver[19] to interface the CAMAC branch highway with the PDP-11 Unibus. In addition they provided a BISON BOX[20] and its Unibus interface. This module provided the basic event related interrupt service. Moreover it made possible high level communications with the host during interrupt processing.

3.3 ON-LINE SOFTWARE

The PDP-11/45 was run under the RT-11 operating system. Data acquisition was performed using the

---

[16] The ABM/CADAC system is documented in S. Centro, et. al., "Fast AD Conversion of Pulse Sequences," NIM 150 (1978) 565 and B. Wadsworth, "Comments on an Implementation of Analog Storage for the Forward Gamma Detector," APC Engineering Note 78-2, March 1978. The operational characteristics of this system are described by J. T. Bober, Ph.D. thesis, M. I. T., Aug. 1984.

[17] LeCroy Research Systems Corporation Model 2250Q

[18] AEC Committee on Nuclear Instrumentation Modules, "CAMAC a Modular Instrumentation System for Data Handling," United States Atomic Energy Commission TID-25875, July 1972.
U. S. NIM Committee, "CAMAC Tutorial Articles," Energy Research and Development Administration TID-26618, Oct. 1976.

[19] R. G. Martin, "Engineering Specification: PDP-11/CAMAC Branch Driver," Fermilab ES-RM1000/2300.00, May 1976.

[20] A. E. Brenner and R. G. Martin, "BISON Interrupt and Gate Control," Fermilab BISON HN-3.2, Jan. 1977.

Fermilab developed MULTI system[21] as modified for E570.[22]

The major feature of MULTI is the RTDA system.[23] A data acquisition programming language and a translator are define within RTDA. This language allows a versatile set of CAMAC operations (referred to as a CAMAC *list*) to be executed from interrupt level based on trigger information. The CAMAC list controlled all data acquisition operations while the supervisor RTDA was responsible for logging data buffers to tape.

In a background capacity MULTI sampled the data buffers in order to keep the experimenters informed as to the performance of the detectors.

The computer was equipped with extended (256K) memory to accommodate the large volume of data produced by the spectrometer during the six bubble chamber expansions.

3.4 SYSTEM TIMING

Data acquisition was based on the accelerator clock. The detector readouts were active only during valid beam times. After each ping an interrupt was delivered via the BISON BOX. The CAMAC list typically finished data retrieval within 50 milliseconds.

During the ten to fifteen second interval between beam spills a distinct set of CAMAC instructions was executed under the direction of the BISON BOX. This interrupt was used to record electronic calibration data.

---

[21] J. F. Bartlett, et. al., "RT/RSX MULTI: Packages for Data Acquisition and Analysis in High Energy Physics," Fermilab PN-115, June 1979.

[22] H. Taft and R. Steiner, "E570 Online Multi Modifications," (internal memo), April 1981.

[23] L. Taff, et. al., "RTMULTI Data Acquisition System," Fermilab PN-110.1K, July 1979.

Chapter 4

DATA PROCESSING

Data taking for E570 occurred during the periods 6 February through 25 March and 6 May through 1 June of 1982. During that time more than 10^6 bubble chamber expansions were recorded in each of four camera views. In addition approximately $3 \cdot 10^{10}$ bytes of electronic event and calibration data were recorded. It is the intent of this chapter to detail the process of detector calibration necessary to use this data for event reconstruction and subsequent Physics analysis.

The data presented in this thesis are taken from the early part of the latter running period (hereafter run A) and the later part of the earlier period (run B).

4.1 BEAM IDENTIFICATION

Careful attention must be devoted to the Čerenkov counters as these detectors determine the initial state quantum numbers. In the following we will examine the properties of the counters, the modes in which they were operated, and the identification algorithm used in particle identification.

4.1.1 Pressure Curves

Pressure curves were taken for the three counters. The signals from the five photomultiplier tubes were recorded by scalers under the joint supervision of an upstream scintillator telescope and the beamline MAC computer system. Each of the counters was pumped down to hard vacuum and then filled in stages with helium gas. We will maintain for the purposes of this discussion the beamline naming convention. The signals will be referred to as 116I, 116O, 118I, 118O, and LDC. Beamline enclosure numbers such as 116, 118, and LDC referred to the location of the respective counter heads while the suffixes I and

O indicate the inner and outer mirrors of differential counters. One further signal bears mention. The beam gate used for these studies, referred to as 3SBCB4, was naturally used to normalize the various runs. 2000 beams were accumulated in a typical run.

Figures 4.1 and 4.2 show the recorded points for the 116 and 118 counters as a function of pressure. Also plotted are the statistical errors. The short LDC counter had a featureless pressure curve and was operated by dead reconning.

4.1.2 Identification Algorithm

The counters were operated during the run under the conditions listed in table 4.1. We see that the 116 and LDC counters were operated just below the kaon threshold in helium of 1.34 PSIA. As 116 was used in threshold mode the two signals 116I and 116O have been merged into 116OR in further use. The 118 counter was operated in differential mode above the proton threshold of 4.82 PSIA. The pressure was set such that photons produced by both pions and kaons would fall on the outer mirror, while only light from protons would fall on the inner phototube. The signal 118IO, being the and of 118I and 118O, was used to minimize the amount of overlap when choosing the running pressure (see figure 4.2).

As a result of the choice of operating modes there were four signals used in beam identification aside from the two muon flags. The sixteen possible bit patterns and their associated tags are listed in table 4.2. The two muon scintillators flagged the contamination in the beam due to on-momentum muons. This amounted to 5.1% of the beam.

TABLE 4.1	
ČHERENKOV PRESSURE	
counter	pressure (PSIA @ 0°C)
116	1.2
118	8.8
LDC	1.2

In all 83.4% of the beam was usefully identified and this was divided among the particle species as listed in table 4.3

4.1.3 Inter-sample Contamination

By examining the efficiencies of the counters we can estimate the level of misidentification present in the data. The following analysis is based on the entire sample of 10^6 beams from the A run.

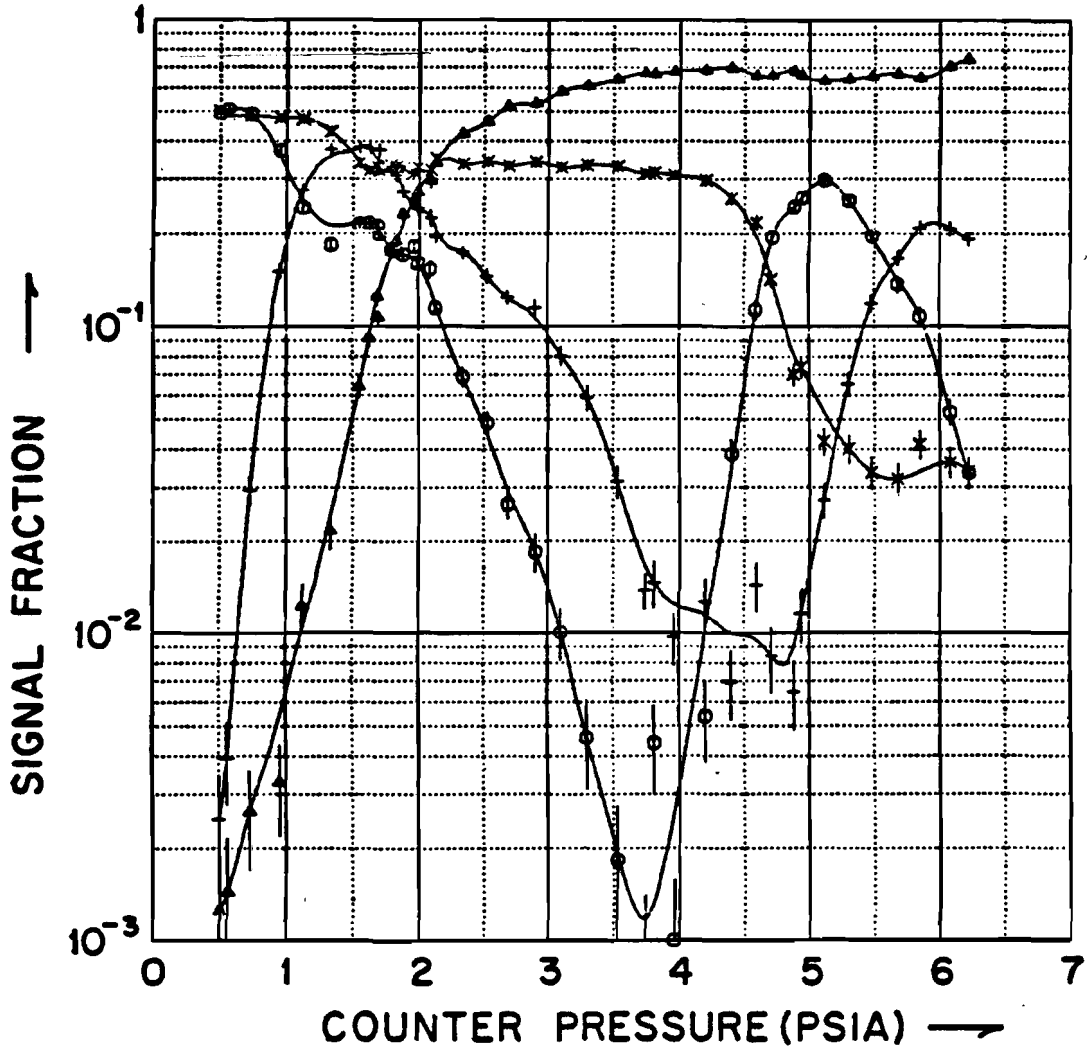

Figure 4.1 The pressure curve for the 116 Čerenkov counter. The measured fractions were: ○ 116I, △ 116O, + 116IO (both), × 116NN (neither).

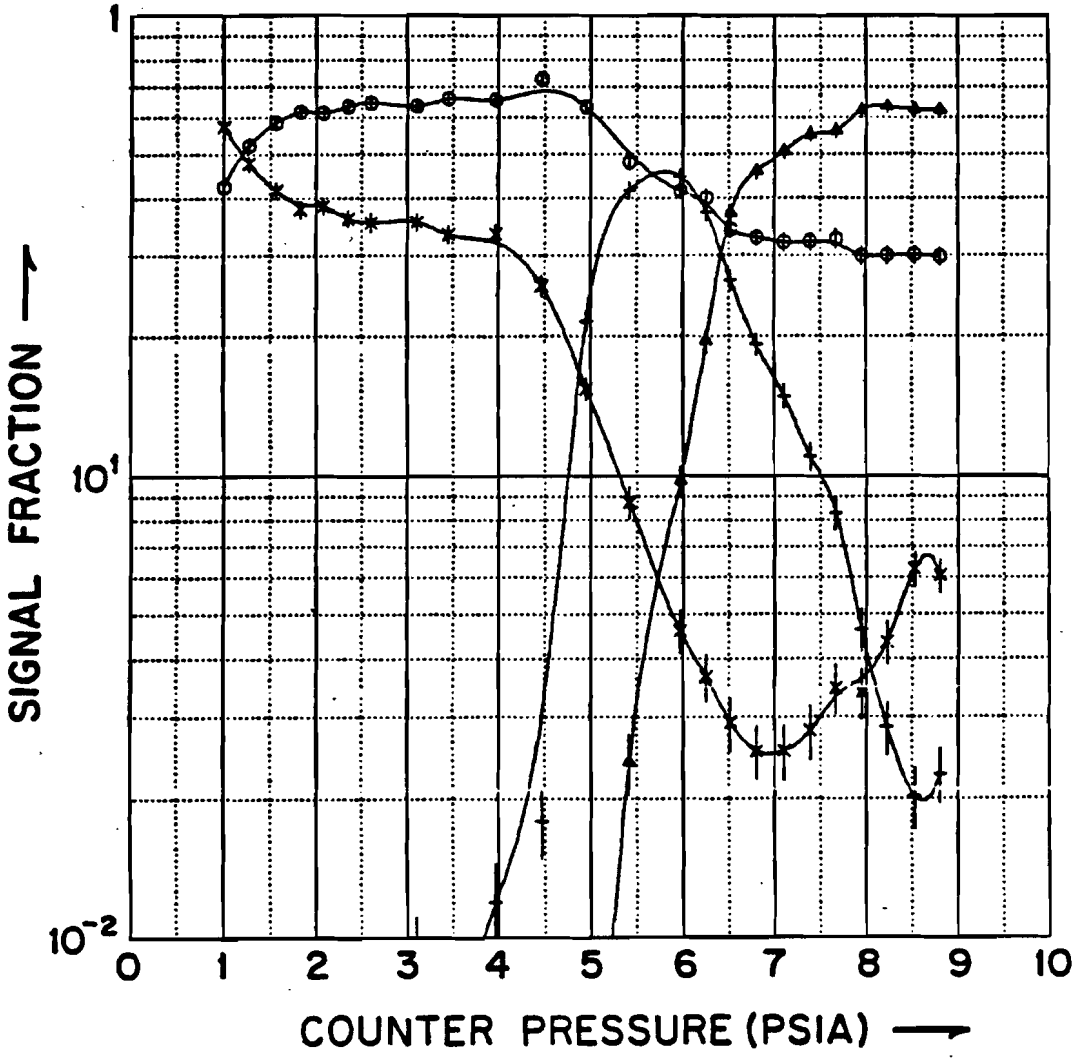

Figure 4.2 The pressure curve for the 118 Čerenkov counter. The measured fractions were ○ 118I, △ 118O, + 118IO (both), × 118NN (neither).

TABLE 4.2					
ČHERENKOV BIT PATTERNS					
118I	118O	116OR	LDC	tag	fraction†
0	0	0	0	—	0.051
0	0	0	1	π	.003
0	0	1	0	π	.004
0	0	1	1	π	.012
0	1	0	0	K	.138
0	1	0	1	π	.032
0	1	1	0	π	.067
0	1	1	1	π	.346
1	0	0	0	p	.304
1	0	0	1	—	.001
1	0	1	0	—	.003
1	0	1	1	—	.001
1	1	0	0	—	.026
1	1	0	1	—	.002
1	1	1	0	—	.002
1	1	1	1	—	.009

†excluding identified muons

TABLE 4.3	
BEAM COMPOSITION	
tag	fraction†
π	51.2
K	15.3
p	33.6

†percentage of usefull beam

Because three counters are available which register pions we may use them in pairs to estimate the efficiency of the remaining counter. Hence, as an example,

$$\epsilon^{\pi}_{116} = \frac{N_{68D}}{N_{6D}},$$

where N_{6D} represents the number of two fold coincidences of 116 and LDC. Similarly N_{68D} is the number of three fold coincidences. The pion detection efficiencies were determined to be as follows:

$$\epsilon_{116} = 0.915$$

$$\epsilon^{\pi}_{118} = 0.968$$

$$\epsilon_{LDC} = 0.840.$$

We observe that ϵ^{π}_{118} is the largest due to the fact that 118 was operated at much higher pressure than the other counters. The relative inefficiency of LDC is due to its short length.

Kaons were tagged by a unique signal from the 118O phototube. Since the same amount of radiator, optical system, and phototube were used as for detecting pions we expect the kaon detection efficiency to be near ϵ^{π}_{118}. This is due to the mild β dependence of the number of Čerenkov photons produced above threshold. Referring to table 4.2 we see that a pion will be tagged as a kaon if both 116 and LDC do not fire but 118O does. This occurs with probability

$$P(K|\pi) = (1-\epsilon_{116}) \cdot (1-\epsilon_{LDC}) = 0.0136$$

Factoring in the relative amounts of pions and kaons indicates that 4.5% of all K tags are in fact pions.

We do not expect K or p to enter in the π tags as both 116 and LDC were operated below K (and p) threshold. It is difficult to estimate the intersample contamination between kaon and proton with the data thus far presented. In particular two beams overlapping a single time slot create ambiguous bit patterns. We see that 2.6% of the beams produce light at both of the 118 mirrors with no signal in 116 and LDC. This may be due to beam overlap or to optical misalignment. In the latter case this number represents an upper limit on the K/p mixing.

4.2 FILM SCANNING AND MEASURING

The digitization of track images was fundamentally a two step process. The film was scanned frame by frame for events. When acceptable interactions were encountered a professional scanner first characterized the event topology. Then using an image plane digitizer (IPD) the scanner recorded two or three guidance points along each track as well as the event vertex. The film and IPD data were then passed to an automated, precision measuring machine for final track digitization.

All of the film presented in this thesis was scanned and/or measured by the MIT or Rutgers University groups.

4.2.1 Scanning Procedures

The exact details of the scanning procedure were specified[1] based upon extensive experience with film of a similar nature. Briefly, scanning was done in three steps:

1. **identification** of valid interactions
2. **classification** by topology
3. **IPD** measurement of track points.

A single view of each frame was examined to determine if an interaction had taken place in the fiducial volume of the chamber depicted in figure 4.3. The high resolution view was used for reference purposes during the scan. Once an interaction had been found a selection criteria was enforced by the scanner. Events were accepted in only the following cases:

- any event in volume **A**
- any two prong or kaon induced event in volume **B**
- any interaction within the nuclear targets of charged topology less than or equal to 14. In addition neutral V's were measured for plate events of any topology.

Beam identification was made possible by the program *TRIFID*.[2] Every beam track in a roll was reconstructed in the upstream PWC system. Each track was then swum to the upstream edge of the fiducial volume and its location transverse to the beam direction was calculated in the scan table system. A list of such predictions along with the Čerenkov tag allowed the scanner to identify the individual beams. Events with another beam track within 2 mm (space) were rejected.

The reasons for the event criteria were manifold. Paramount among them was the desire to make available the most interesting combination of data as soon as possible. Since the fraction of kaons in the beam was small they were favored in the scanning stage. High multiplicity (e.g. 50 charged prong) plate events required special measures during their scanning[3] and so they were deferred. The reason for measuring all two prong events will be discussed in detail in §4.8.

4.2.2 Automated Measuring

The scanner's track guidance points were used by an automatic measuring machine in order to locate,

[1] E. S. Hafen, R. I. Hulsizer, and P. E. Stamer, "Scanning Rules for the 1982 Run of E565/570," IHS Consortium Newsnote #56, April 1982.

[2] R. J. Plano, "*TRIFID*," GEOHYP Note 2, June 1982.

[3] The reader is directed to the forthcoming Ph.D. thesis of Robert DiMarco (Rutgers University) for one method of scanning, measuring, and reconstruction of such high multiplicity events.

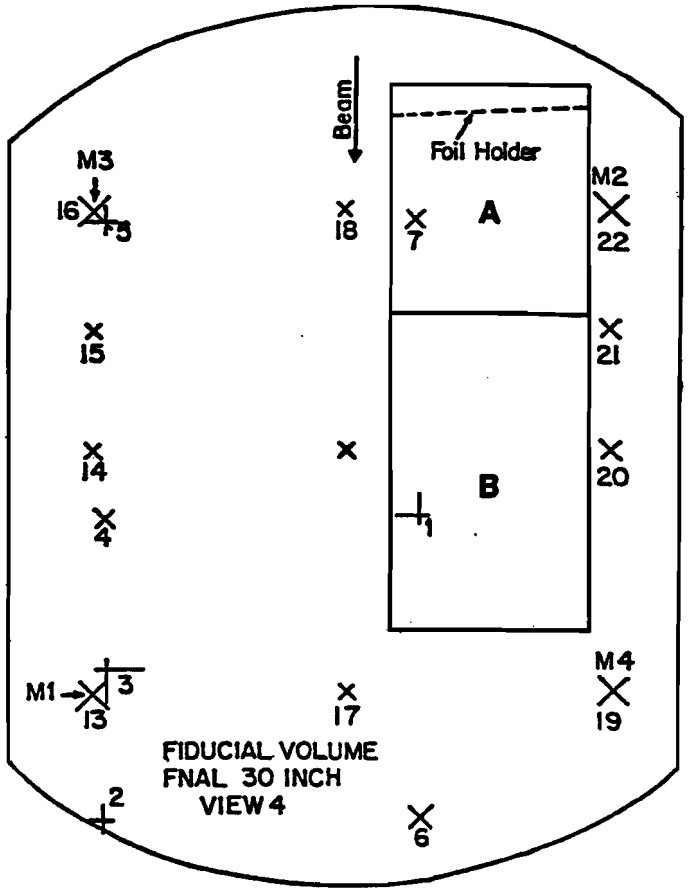

Figure 4.3 The bubble chamber as seen from camera port #4. Events were selected base on the location of the vertex (volume A or B), the topology, and the beam tag.

follow, and measure track images. The PEPR (precision encoding and pattern recognition) device[4] generated a line segment on a precision cathode ray tube. The segment was imaged onto the film and, by transmission, the face of a photomultiplier tube. Rotation and translation of the segment allowed optimization of the pulse height detected by the phototube and thus the location of a track element. Track following software drove the segment along the track image measuring its location and optionally its transmissivity.

4.3 WIRE CHAMBER SURVEY

The wire chamber system was composed of four major elements, namely, the upstream proportional wire chambers (PWU), the downstream proportional wire chambers (PWD), the drift chambers (DC), and CRISIS. Each of these detectors provide information of the same sort: they record the passage of a track

[4] See for example F. C. Winkelmann, Ph.D. thesis, M. I. T., 1968, and M. K. Choe, "The Subroutines of the PEPR Load," PEPR Programming Note PG-42.

through a *strip* in a plane perpendicular to the beam axis. It is the objective of reconstruction programs to associate a collection of such strips into individual tracks in space. A full understanding of each chamber's operating characteristics must be achieved before one attempts such event reconstruction. The following paragraphs discuss the programme undertaken to determine the wire chamber parameters relevant to event reconstruction.

4.3.1 Coordinate System

In order to allow easy manipulation of data within a given detector each of the major detectors has its own internally defined coordinate system. When data is required from several detectors simultaneously all space points and vectors are transformed into one master coordinate system which we shall refer to as the spectrometer system. The spectrometer system is defined within PWU by requiring its x-axis to pass through given wires in each of four planes. Since the first and last PWU triplets are separated by roughly 35 m they are used to give superior angular resolution. The line which passes through the central wires in two of the A triplet planes and two in the C triplet has been defined as the x-axis. This axis, denoted by $\hat{X}_S$, is of necessity closely parallel to the average beam direction. The y-axis is chosen to fall in the plane formed by $\hat{X}_S$ and vertical, and is directed toward the earth. $\hat{Z}_S$ finishes the right handed system. The origin is chosen to fall in a particular plane within the bubble chamber as will be discussed in more detail in §4.4.

4.3.2 Chamber Parameters

As was already mentioned the physical nature of planar wire chambers dictates that they localize the intersection of a track with a plane to some strip falling in that plane. To describe this strip in the coordinate system we have designed it is convenient to introduce four parameters and one variable. These quantities are independent of the specific nature of the chamber and we will find subsequently that further parameters are needed to fully describe the actual detectors.

As the wire planes fall in the $y-z$ plane one chamber parameter is its location along the x-axis. In figure 4.4 we see that the chamber's orientation about the x-axis may be describe by a single angle α, being the angle between the y-axis and the direction of the wires in the plane. Within the plane distances are measured along a line perpendicular to the wires of the plane. This directed distance ρ has its origin at the point of intersection of the x-axis and the plane. The direction of increasing rho is given by $\vec{\alpha} \times \vec{x}$. In order to locate the chamber physically about the x-axis the distance between the axis and a hypothetical zeroth wire (referred to as ρ_0) is ascribed to each plane. The final parameter needed to describe the chamber is $\delta\rho$, the interval in ρ which describes the uncertainty in a single measurement of ρ.

4.3.3 Parameter And Interval Estimation In MWPC

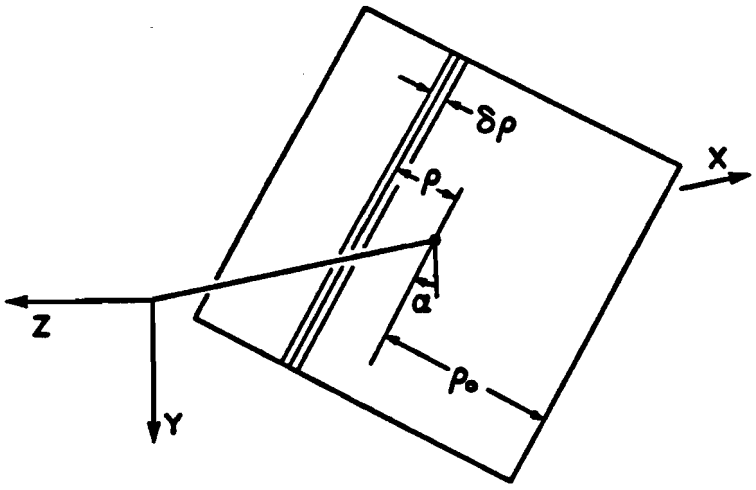

Figure 4.4 The coordinates used in describing the location and orientation of a wire chamber. Also shown is the strip used to describe a struck wire.

Prior to describing the mechanics of the wire chamber survey program we will review the general techniques of track parameter and interval estimation in multiwire proportional chambers.

Suppose we have a set of n chambers labeled by the index i. And that each plane represents a set of quantities $(x_i, \alpha_i, \delta\rho_i; \rho_i)$. We have already seen that x_i, α_i, and $\delta\rho_i$ are parameters which depend simply on the plane index. ρ_i is, however, a random variable to be measured by the experimenter. In order to reconstruct a track in a force free region we need to determine a set of parameters $\eta = (y_0, a_y, z_0, a_z)$ representing the track intercepts and x-slopes at some plane $x = x_0$.

The following paragraphs describe the track fitting algorithms used in the wire chamber sections of the data processing and reconstruction programs.

4.3.3.1 χ^2 parameter estimation

In the general case we wish to evaluate a set of m parameters η given a set of n measurements. We observe that the directed distance ρ_i^{fit} may be written as a function of the fit coordinates of the track's intersection with the plane (x_i, y_i, z_i).

$$\begin{aligned}\rho_i^{fit} &= z_i \cos\alpha_i - y_i \sin\alpha_i \\ &= (z_0 + a_z(x_i - x_0))\cos\alpha_i - (y_0 + a_y(x_i - x_0))\sin\alpha_i\end{aligned}$$

The argument is not changed by making the choice $x_0 = 0$, which we will do for simplicity of notation. With this one may write the system of equations

$$\rho = \mathbf{B}\eta$$

$$\begin{pmatrix} \rho_1 \\ \vdots \\ \rho_i \\ \vdots \\ \rho_n \end{pmatrix} = \begin{pmatrix} \vdots & \vdots & \vdots & \vdots \\ -\sin\alpha_i & -x_i\sin\alpha_i & \cos\alpha_i & x_i\cos\alpha_i \\ \vdots & \vdots & \vdots & \vdots \end{pmatrix} \begin{pmatrix} y_0 \\ a_y \\ z_0 \\ a_z \end{pmatrix}.$$

The case $m = n$ finds its solution in $\eta = \mathbf{B}^{-1}\rho$. The more typical case is, however, for the number of measurements to exceed the number of parameters to be estimated ($n > m$). In this case we are faced with finding the solution to an over-constrained set of linear equations.

Although the choice of an estimator is typically a difficult decision we will make the usual Physics choice for track fitting and use the chi-square estimator. One can in general write an expression for the probability of observing a set of measurements under a given parent distribution. This total probability is referred to as the likelihood function. Under the assumption that the random variable is normally distributed we write the likelihood

$$L(\eta) = \prod_{i=1}^{n} e^{\frac{-r_i^2}{2\sigma_i^2}}$$

or

$$\ln L(\eta) = \sum_{i=1}^{n} \frac{-r_i^2}{2\sigma_i^2}.$$

In the above the residuals are defined by

$$r_i = measured \quad value - fit \quad value,$$

and are by assumption normally distributed with variance σ_i^2

We observe in the chosen case that maximum likelihood is equivalent to a χ^2 minimum. Hence the desired solution vector η minimizes the expression

$$\chi^2 = -\ln L(\eta) = \sum_{i=1}^{n} \frac{(\rho_i^{meas} - \rho_i^{fit})^2}{\sigma_i^2}.$$

The condition

$$\min_{\substack{\eta_j \\ 1\le j\le m}} \left\{ \chi^2 = \sum_{i=1}^{n} \frac{(\rho_i^{meas} - \sum_{j=1}^{m} b_{ij}\eta_j)^2}{\sigma_i^2} \right\},$$

produces the set of equations

$$\frac{\partial\chi^2}{\partial\eta_j} = 0 = -2\sum_{i=1}^{n} \frac{b_{ij}(\rho_i^{meas} - \sum_{j=1}^{m} b_{ij}\eta_j)^2}{\sigma_i^2}.$$

In line with the simple level of discussion we will illustrate the case of *equal errors*, that is all σ_i

being equal. With this assumption we may write the matrix equation which specifies the χ^2 solution

$$\begin{pmatrix} \sum \rho_i \sin\alpha_i \\ \sum x_i \rho_i \sin\alpha_i \\ -\sum \rho_i \cos\alpha_i \\ -\sum x_i \rho_i \cos\alpha_i \end{pmatrix} = \begin{pmatrix} \sum \sin^2\alpha_i & \sum x_i \sin^2\alpha_i & -\sum \sin\alpha_i \cos\alpha_i & -\sum x_i \sin\alpha_i \cos\alpha_i \\ & \sum x_i^2 \sin^2\alpha_i & -\sum x_i \sin\alpha_i \cos\alpha_i & -\sum x_i^2 \sin\alpha_i \cos\alpha_i \\ & & \sum \cos^2\alpha_i & \sum x_i \cos^2\alpha_i \\ & & & \sum x_i^2 \cos^2\alpha_i \end{pmatrix} \begin{pmatrix} y_0 \\ a_y \\ z_0 \\ a_z \end{pmatrix}$$

Inversion of this symmetric matrix gives the parameter estimates.

4.3.3.2 χ^2 interval estimation

The procedure illustrated in the preceding paragraph may be generalize to include estimation of the fit covariance matrix **V**. We summarize bellow the result of such a calculation.[5] Assuming the linear dependence of measurements on the parameters above we introduce *weights* into the expression for χ^2. This is done in order to both allow the relative size of the weights to influence the fit and to allow for the determination of the correlations between the fit parameters. Thus we write

$$\chi^2 = \sum_{i=1}^{n}\sum_{j=1}^{n}(\rho_i - \sum_{k=1}^{m} B_{ik}\eta_k)\cdot(V^{-1})_{ij}\cdot(\rho_j - \sum_{k=1}^{m} B_{jk}\eta_k).$$

We will make the assumption in all that follows that in a grand average the measurements of the detectors are not correlated. This allows use of a diagonal weight matrix

$$(V^{-1})_{ij} = W_{ij} = \begin{cases} 1/\sigma_i^2, & \text{if } i = j; \\ 0, & \text{if } i \neq j. \end{cases}$$

Thus only the individual detector resolutions affect the fit.

Once again we demand a χ^2 minimum and hence

$$\frac{\partial \chi^2}{\partial \eta_j} = 0.$$

Solution of this set of equations provides the interval estimates

$$V_{ij}^{fit} = [(\mathbf{B}^T\mathbf{V}^{-1}\mathbf{B})^{-1}]_{ij} = [(\mathbf{B}^T\mathbf{W}\mathbf{B})^{-1}]_{ij}.$$

4.3.3.3 Note on track fitting in the Chebyshev norm

James[6] recently suggested an alternative to chi-squared fitting in wire chambers. This author pointed out that the track residuals in proportional wire chambers are not normally distributed, but rather

---

[5] The interested reader may wish to consult the literature for a more detailed treatment of this topic. One discussion which is phrased in terms of track fitting is to be found in §2 of H. Eichinger and M. Regler. "Review of Track Fitting Methods in Counter Experiments," CERN 81-06, Data Handling Division, 1981. This paper provides a description of the important *filter* techniques of pattern recognition. Vertex fitting and the effects of detector resolution and multiple scattering are also discussed.

[6] F. James, "Fitting Tracks in Wire Chambers Using the Chebyshev Norm Instead of Least Squares," CERN DD/82/14, Sept. 1982. (submitted to NIM)

that they are governed by the uniform distribution. He then proposed the use of track fitting in the Chebyshev norm due to its superior efficiency under this distribution function.

In order to investigate this approach track fitting programs were written by this author which used Chebyshev estimation. The fitting algorithm is described in detail in appendix B. A comparison was made between the RMS deviation of tracks fit in the upstream PWC system of the FHS (9 planes grouped into three 120° triplets) using both the χ^2 and L_∞ estimators. As was expected the Chebyshev estimator had a superior efficiency. The new fitting algorithm, however, required several times longer to perform each track fit. Since the gain in efficiency for nine wire planes is small and must be traded against computational expense this technique was deemed inappropriate for use in the upstream wire chamber system.

Although the benefit would be theoretically greater for the seventeen downstream wire chambers this fitting method would be inappropriate for two reasons. Most important is the fact that a drift chamber's position error is dictated by the diffusion equation and hence is normally distributed. We also note that any increase in the time required for track fitting in the downstream would add prohibitively to the event processing time.

4.3.4 Determination of Track Parameters

In order to determine the chamber parameters the program *SURVEY*[7] was written. This program was designed to recognize non-interacting beam tracks in the spectrometer and to use them to align the various chambers.

At the end of data taking the location along and orientation about the beam axis of each chamber was determined. These parameters are respectively the x_i and α_i of §4.3.3. A theodolite survey was undertaken to locate the four corners of each wire plane relative to the downstream face of the bubble chamber magnet. This produced results accurate to twenty mils. The upstream distances were measured using a steel tape. The actual wire orientations were determined with the use of a level having a nominal accuracy of one minute of arc. These data were used as input to the survey program.

SURVEY was run on each roll of data considered in this thesis. The major reason for this was to keep track of variations in drift velocities, most notably the CRISIS drift velocity. Another important reason being the occasional removal and replacement of wire chambers due to inevitable breakdowns.

The following paragraphs describe the techniques used to parameterize the wire chambers.

4.3.4.1 Program flow

[7] This program descends from the SRVEHS PAM, although in adaptation for the FHS it was essentially rewritten by this author. The only concept retained from the original was that of the upstream axis determination.

The overall complexity as well as the initial indeterminacy of the survey problem demand an iterative approach to fitting. An algorithm was developed which required a total of five passes through a data set in order to establish all of the wire chamber parameters. Very briefly those five steps can be summarized as follows.

1. Four planes in PWU were used to solve the track parameter equations. The average residuals in the remaining planes were used to align all of the upstream chambers.

2. χ^2 track fits using all nine planes were used to improve the overall PWU alignment.

3. First order CRISIS parameters were determined using upstream track fits in conjunction with course cuts to locate non-interacting beams downstream.

4. Non-interacting beams were identified precisely. DC data was fit to predictions from the upstream system. First order downstream PWC locations were obtained and the CRISIS parameters were improved.

5. The PWC and CRISIS parameters were finalized. Downstream track fits were made as a consistency check.

Each pass scanned the data set until 1000 of the required tracks were located. Data sets were obtained by extracting the wire chamber data blocks from every fifth frame of a given roll. This was done in order to accurately average variations over the course of a roll. The data sets typically contained 3000 incident beam tracks.

4.3.4.2 Upstream wire chambers

As mentioned previously the spectrometer x-axis was defined by the line passing through a specific wire in each of four *master planes*. Using the four master planes alone one could *solve* for the four track parameters. By projecting the tracks to the locations of the other planes average chamber locations were formed. The shift in chamber location was given by

$$\Delta\rho_i = \frac{\sum_{j=1}^{n} \rho_{i,j}^{projected} - \rho_{i,j}^{measured}}{n}$$

for a set of n tracks.

At the end of the first pass the $\Delta\rho_i$ and their standard errors $\sigma_{\Delta\rho_i}$ were evaluated.

In the second pass the redundancy of the upstream system was exploited to obtain superior estimates of track parameters and thereby improve upon the chamber alignment. Time slots were selected which had hits in each of the 9 PWU planes. Tracks were then fit as described in §4.3.3. In these fits a diagonal

weight matrix was assumed. The position error was taken to be $\sigma_y^{PWC} = 577\,\mu$m.[8] Tracks were rejected if their reduced chi-squared had a value $\chi^2_\nu > 3$. For accepted tracks new $\Delta\rho_i$ were accumulated. Upon completion of the data scan a line η^{meas} was passed through the $\Delta\rho_i$ for the master planes. We required originally that this line pass through the four wires used to define the x-axis. Hence the $\Delta\rho_i$ must undergo a rotation in order to maintain consistency in this definition. The planes were thus each moved by

$$\Delta\rho_i' = \Delta\rho_i - \mathbf{P}^i \cdot \eta^{meas} = \Delta\rho_i - \begin{pmatrix} -\sin\alpha_i & \cos\alpha_i & -x_i\sin\alpha_i & -x_i\cos\alpha_i \end{pmatrix} \begin{pmatrix} y_0^m \\ a_y^m \\ z_0^m \\ a_x^m \end{pmatrix}$$

Here we use $\mathbf{P}^i$ to represent the projector of a track impact point into the directed distance measured by plane i.

Due to the inherent stability of the upstream arm of the spectrometer it was only necessary to determine the chamber locations twice. A set of constants was determined for run **A** and another for **B**. In this way the roll by roll *SURVEY* production running circumvented the first two passes.

4.3.4.3 CRISIS

The origin of the CRISIS system was located at the physical center of the device. Its x-axis was parallel to the high voltage planes. The y-axis points toward earth and the z-axis along its wire direction.

In relation to the spectrometer system CRISIS was both translated and rotated. Its position relative to the bubble chamber in the horizontal was determined by hand measurements.[9] Since the drift direction was in the bend plane the z coordinate of this detector is entirely moot. The angles of yaw and roll are taken to be zero in the following analysis. Hence, the parameters to be determined are y_0 (the y offset) and β (the pitch).

We recall that for a planer drift chamber the parameters to be estimated were (ρ_0, v_d, t_0). Due to its spatial extent along the beam direction CRISIS demands the evaluation of (y_0, v_d, t_0, β). Note that there is no conceptual difference between ρ_0 and y_0. This change in notation simply reflects the alignment of the sense wires in CRISIS with the horizontal.

The introduction of β creates a complication not present with the other wire chambers. We note that the drift velocity

$$v_d = \frac{dy^{CR}}{dt}$$

[8] This number is arrived at by calculating the second moment of a uniform distribution on $(-\frac{w}{2}, \frac{w}{2})$, w being the wire spacing of the chamber. The result is $\sigma = 1/\sqrt{12}w$.

[9] D. Goloskie, private communication.

is correlated with the rotation angle as they are both in effect slopes.

$$a_y^{CR} = \frac{dy^{CR}}{dx^{CR}} = v_d^{-1}\frac{dt}{dx^{CR}} = \frac{dy^S}{dx^S} + \tan\beta$$

or

$$v_d^{-1}a_t^{CR} = a_y^S + \beta,$$

in a small angle approximation. Here the superscripts S and CR refer to the spectrometer and CRISIS coordinate systems respectively. With the measured quantities a_t^{CR} (the time slope in x) and a_y^S (the y slope) related the fitting problem becomes extended to a system of four simultaneous equations. As we will see in the next section (ρ_0, v_d, t_0) are related in a piece-wise linear fashion due to the left-right ambiguity. Rather than attempt a simultaneous four parameter fit an iterative procedure was adopted to evaluate $(\rho_0, v_d, t_0, \beta)$.

In passes 3 through 5 beam tracks were fit in the upstream system and swum through the bubble chamber magnetic field to the location of CRISIS. For pass 3 course cuts on intercept and angle were used to identify non-interacting beams. Passes 4 and 5 required a true hookup between the know beam and a CRISIS plane. After 1000 tracks had been located the fitting algorithm developed for the drift chambers (see §4.3.4.4) was used to determine $(\rho_0, v_d, t_0)^{(n)}$ for the n^{th} pass through the CRISIS data. This result of course depended on the value of $\beta^{(n-1)}$ determined in the previous pass. During the data scan the differences

$$\beta^{(n)} = v_d^{(n-1)}a_{t_i} - a_{y_i}^S$$

were stored for each event i. The mean $\langle\beta\rangle$ and standard deviation σ_β were determined. The mean was then evaluated using only those tracks within $3\sigma_\beta$ of $\langle\beta\rangle$. This produced the estimate of $\beta^{(n)}$.

This linearized fitting method converged rapidly. Within six passes through the CRISIS data both β and v_d had settled to sufficiently accurate values. The six passes were obtained by feeding the results of one *SURVEY* run into a second.

Once (y_0, t_0, β) had been determined their values were used as constant inputs to the roll by roll *SURVEY* runs. As CRISIS was moved between runs **A** and **B** these constants were evaluated for both runs. Only v_d was evaluated on a roll dependent basis. This was accomplished by simple averaging with suppression of outliers, much the same as for $\beta^{(n)}$ above. Pass 3 gave a value of v_d sufficiently accurate to select beams for use with the other chambers in the remaining passes. The value of v_d itself was refined in passes 4 and 5.

4.3.4.4 Downstream wire chambers

A very prominent consideration in the design of the downstream survey was the ability to determine with certainty whether a track interacted in the bubble chamber or not. If a track did not interact then a knowledge of the upstream trajectory could be used to predict where each plane would be crossed in

the downstream. In order to achieve this track selection the pattern recognition capabilities of CRISIS [10] were put to use. Since this detector provided 192 redundant measurements for beams it was a simple matter to find them. The ISIS processor [11] was used to reconstruct the two dimensional tracks (or three dimensional *planes*) in CRISIS. Tracks were considered to be non-interacting if the plane fit matched the upstream prediction swum to the plane within 2 mm in y and 0.5 mr in a_y. Once a track was judged to be non-interacting it became available for use in the PWD and DC survey. In swimming a track from the upstream system to a given downstream plane its position and angular errors were evaluated by adding in quadrature the result of the upstream fit covariance matrix and the multiple scattering error deriving from passage through the bubble chamber and its windows.

The downstream PWCs were located by averaging the difference between the recorded wire hits and the prediction from the upstream fit. In pass 4 only hits which were unique to a plane were used. While in pass 5, since the first order location was known, hits were accepted if they were within $4\sigma^{PWC}$ (or 2.3 mm) of the prediction. This suppression of outliers provided location estimates with RMS deviations very much consistent with that expected for a single plane.

Estimation of the drift chamber parameters was more complex than that of the PWCs for a variety of reasons. Most prominent is the fact that a drift chamber measures an absolute value of time rather than a position. As a result one must devolve the distance versus time relationship from one's data. Even under the assertion that distance and time are (piecewise) linearly related one must evaluate a drift velocity and an electronic zero time as well as the chamber location. Another complication arises in that while the upstream and downstream PWCs had comparable resolution the DCs can be expected to be superior by a factor of three to four. Hence the upstream predictions will have a larger intrinsic error than the drift measurements. We will make the assumption *ab initio* that the drift velocity is saturated. Results to follow will demonstrate the validity of this assertion. In this case we may write an expression for time in terms of distance

$$t = \frac{|\rho - \rho_m|}{v_d} + t_0.$$

Here v_d is the drift velocity, t_0 the unknown origin in time due to the TDC, ρ the directed distance as before, and ρ_m the location of the sense wire in the struck cell m. That is $|\rho - \rho_m|$ is the actual drift distance. Referring to the cell width as w we see $\rho_m = mw + \rho_0$.

A flexible fitting algorithm was implemented in order to have the option of specifying an arbitrary time versus distance relationship. The method of Marquart[12] was selected as it combines a gradient

[10] I. A. Pless, "Integrating PWC, DC, and CRISIS Data in the Downstream Spectrometer," DPI Note #12, May 1982.

[11] D. Goloskie, et. al., "The Performance of CRISIS and its Calibration," submitted to NIM, August 1984.

[12] Donald W. Marquardt, "An Algorithm for Least- Squares Estimation of Nonlinear Parameters," J. Soc. Ind. Appl. Math., 11 (1963) 431.

search of χ^2 with linearization of the fitting function. Bevington's[13] implementation of the algorithm was used in both the drift chamber and CRISIS fitting. Normally the curvature matrix is derived by the Taylor expansion of the fitting function in terms of increments in the parameters. In the current method the diagonal terms of the curvature matrix are weighted by one plus a scale parameter. By varying the scale parameter one may force the system of equations to represent a range of solutions between the parameter shifts given by the method of expansion and the gradients found by the search technique. By judicious control of the scale parameter rapid convergence is reached.

The upstream fit covariance matrix elements were projected into the direction of drift for a given plane. A calculation of the multiple scattering error expected at the plane was performed. These two errors were then added in quadrature with the expected drift chamber resolution and used as weights in the fit. For reference we list in table 4.4 the various contributions to the dispersion of position measurements in the drift chambers. Note that the effects of the beam momentum dispersion were note included in the roll by roll survey, and in fact are mute in the field off survey. No attempt has been made to include the effects of incomplete knowledge of the magnetic field map.

TABLE 4.4

DC FIT INPUT ERRORS

source	F chamber	G & H chambers
PWC intercept	577 μm	577 μm
PWC slope	160	400
mult. scatt.	185	450
beam momentum	340	860
intrinsic DC	200	200
all	740	1200

The fit is carried out over several iterations through the accumulated set of time and distance data. This is done to allow for more complete suppression of outliers. We have seen in figure 4.5 the results of selecting non-interacting beams with CRISIS. Since this detector only measures one coordinate transverse to the beam we are not fully successful in eliminating scatters in the unmeasured plane. At the end of each pass the RMS deviation of the time data from the current fit predictions was calculated. The first fit was done using all of the data points. In the following passes points outside of $3\sigma_t$ are dropped. A total of five passes are made through the data. On the final three a cut was made to exclude hits within 2.5 mm of the inter-cell boundary. This cut was imposed due to a slight non-linearity of the

[13] Philip R. Bevington, "Data Reduction and Error Analysis for the Physical Sciences," pp. 235–240. (New York: McGraw-Hill, Inc.) 1969.

time to distance relationship in this region.

The results achieved in terms of the error on parameter estimates are dominated by dispersions other than that intrinsic to the drift chambers. For example using one thousand tracks in F chamber $\sigma_{t_0} = (740\,\mu\text{m}/\sqrt{1000})/v_d = 0.5\,\text{ns}$ or one fourth of a time encoder least count. We are nonetheless able to locate each of the chambers to better than $\sigma_{\rho_0} = 40\,\mu\text{m}$ and achieve estimates of the drift velocity which are good to better than 1%. The drift velocity in HRS gas has been measured at a field strength of 800 V/cm by E570 to be 100.0 μm/lc (least count) in agreement with the previously measured value of 50 μm/ns.[14]

4.4 BUBBLE CHAMBER OPTICAL CONSTANTS

The reconstruction of particle trajectories from the images recorded by the three bubble chamber cameras requires an understanding of the chamber geometry, the properties of the bubble chamber optical system, and the affects of the measuring machine which is used in track image digitization.

4.4.1 Coordinate System

The bubble chamber coordinate system is based on a set of 22 fiducials inscribed on the surfaces of the two chamber windows. There are 11 fiducials on each glass surface in contact with the liquid hydrogen. The center fiducial (#1) on the camera side window is taken to be the origin of the bubble chamber system.

The x and y axes are derived from the relative orientation the the so called master fiducials on the back glass. The x-axis points in the direction of the beam and the y-axis points toward earth. The z-axis is taken to be parallel to the optic axes of the cameras, and to point from the origin toward the film.

4.4.2 Optical Parameters

In order to use film measurements one must know the relationship between the location of the fiducials on the film plane and in space. The cameras are considered to be pinholes and all light rays are considered to follow their classical paths.

Each camera location is described by the location of its optic axis in the $x - y$ plane of the bubble chamber system as this is the plane of the film. Image and object distances are specified in the bubble chamber system along the z (optic) axis. The distances along the optic axis from the film to lens and from the inside font glass to the lens are also needed to specify the configuration of each camera.

---

[14] G. Baranko, et. al., "Drift Properties of Tubular Drift Chambers in High Magnetic Fields," NIM 169 (1980) 413.

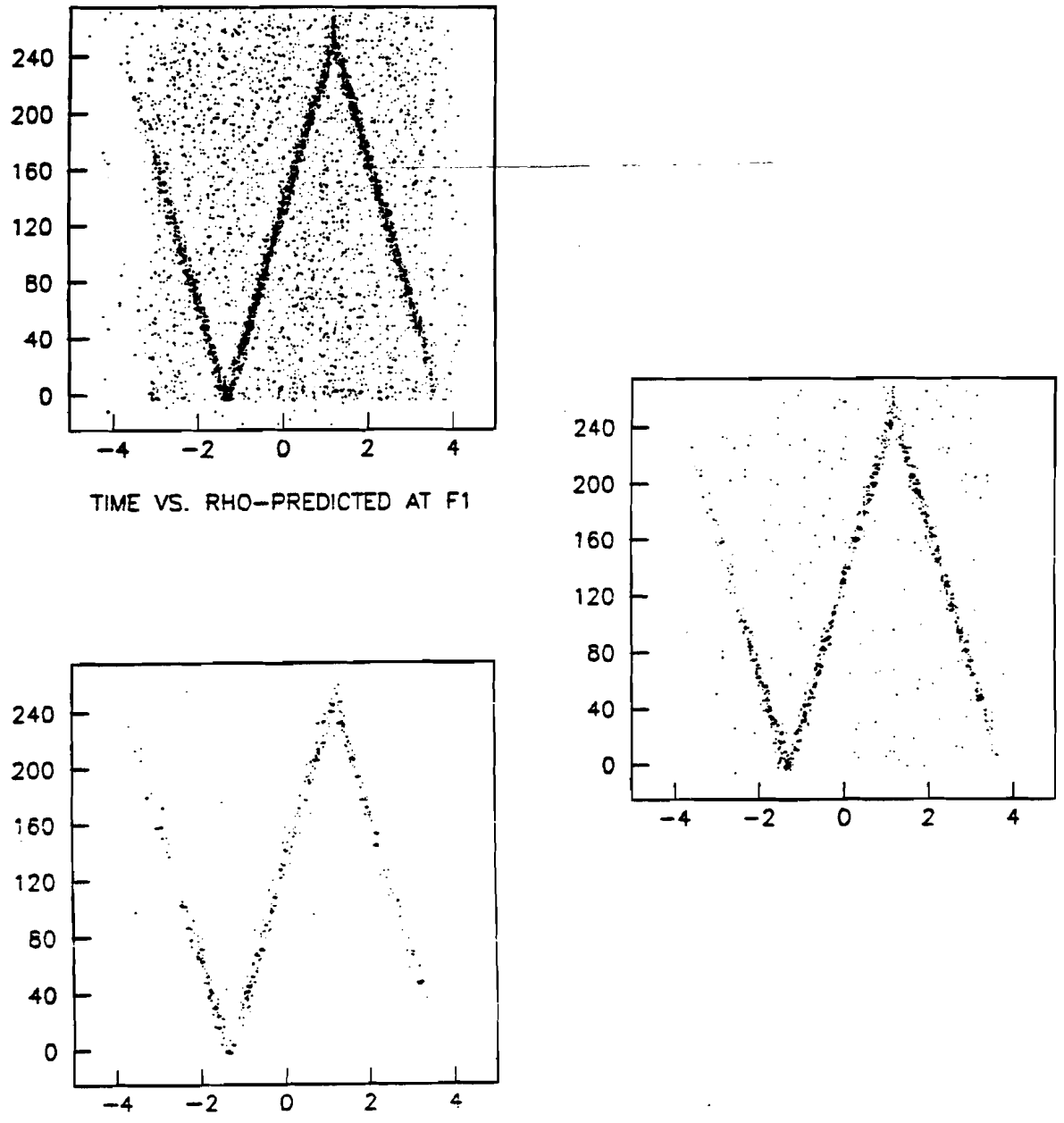

Figure 4.5 The process of isolating non-interacting beam tracks for the drift chamber survey. Each plot shows recorded drift times for a single plane versus their PWU predicted impact parameters at that plane. The upper plot show all hits; the diffuse smear of points is due to tracks which scatter and therefore lose the correlation with the upstream. The center plot shows only those data from time slots with CRISIS selected non-interacting beams. A further cut requiring a single hit in the drift chamber within the beam spot gives the lower plot.

The know values of indices of refraction were used when light rays were traced through dense media.

4.4.3 Fiducial Survey

In order to determine the positions of the various fiducials in space a survey was undertaken. Just prior to running and with the chamber cold (that is to say full of liquid hydrogen) a theodolite was mounted in one of the camera ports. Complete surveys of the fiducials were made by both the bubble chamber crew and a team of Fermilab surveyors. Both surveys measured the horizontal and vertical angular location of each fiducial as well as the angles of the normal to the front glass surface (auto-reflect). Measurements were made with the theodolite stage up (normal) and rotated by 180° (inverted). All angles were recorded with a nominal accuracy of one second of arc. The two data sets have been tested for internal consistency by comparing the normal and inverted measurements. The differences in the surveyors' set show an angular RMS of 50 μr in the horizontal and 75 μr in the vertical (excluding fiducial 16 which differed 380 μr from the mean). The other data set proved to be inferior both in the RMS and the number of outliers. As a result we have chose to work with the surveyors' set.

With the windows at room temperature and on the lab bench a jig bore was used to measure the location of each of the fiducials on both glasses. The combination of the location of the fiducials on their planar glass surfaces, the thickness and index of refraction of each optical medium, and the angular fiducial survey information allows one to fit the remaining unknowns in the system. The program *FIDAJUST*[15] combined this information with the coefficient of linear expansion of the glass (scaling the jig bore results down to liquid hydrogen temperature) to fit all relevant parameters. This program constrains the fiducials to fall on two planes, but allows the back glass to have an arbitrary orientation with respect to the front glass. After fitting the relative orientation of the two glasses and the location of the theodolite, *FIDAJUST* provides the real space locations of all fiducials. In the final run it was decided not to use the measurements from fiducials 13 and 16 during the iterative chi-square fit. The solution found for the average of the normal and inverted survey data thus defines the nominal location of the fiducials.

One may evaluate the intersection of each survey data point with the fit glass planes. The difference between these projected measurements and their fit values show the spatial RMS deviation to be 50 μm for the 20 fiducials used. We have already noted that the survey data differences had an angular RMS of 50 μm, so that a single measurement had an RMS of $50/\sqrt{2} \approx 35$ μm. We can estimate the angular resolution implied by a spatial deviation of 50 μm. The theodolite was located roughly 1.5 m from the chamber center, hence 50 μm/1.5 m $\approx$ 35 μm. This observation confirms that *FIDAJUST* was able to achieve a solution limited only by the setting error of the theodolite. As a result we may proceed with

[15] The author would like to thank Dr. Ron Walker of Fermilab for making the various *FIDAJUST* runs and for providing their results.

confidence in using these results.

4.4.4 Determination of Optical Parameters

The program *CONGEN*[16] was used to fit film plane measurements of fiducials to their know locations in space. This program searched for a χ^2 minimum in the twelve dimensional space defined by the location and focal length of each of the three cameras.

CONGEN was written to evaluate residuals on the individual film planes rather than in space[17] and as such it normally converges rapidly to a solution. The χ^2 is formed from the deviation of measured corresponding points from both their reprojected three view average space point and the actual space location of the point.

Optical parameters were generated for both the MIT and Rutgers PEPR devices.

4.5 BUBBLE CHAMBER SURVEY

In order that tracks may be fit as 'hybrids', that is to say using both bubble chamber and wire chamber information, one must determine the transformation between the two detector coordinate systems. To this end a special data set was developed consisting of non-interacting beam tracks. The selected beams were scanned and measured as though they were interactions with an incident track and one outgoing track. The bubble chamber reconstruction algorithm required the successful reconstruction of an interaction vertex as a point in space. As a result a special procedure was used during the scanning phase which provided a corresponding point in each view. On each accepted track a landmark (such as a δ-ray or a gap in the trail of bubbles) was selected and measured as the position of the vertex in each of the three views.

4.5.1 Track Reconstruction

Each of the time slots for a chosen frame were reconstructed. Ultimately one would like to associate a single time slot with the measured beam. Since the transformation between wire chamber and bubble chamber was as yet unknown the complete list of reconstructed tracks was retained.

The bubble chamber tracks were reconstructed using an algorithm very similar to the bare bubble chamber program described in §5.2.5. First the pseudo-vertex was reconstructed and then the track segments upstream and downstream of it were fit. This fit estimated the tracks angles at the pseudo-vertex given the known beam momentum.

---

[16] R. J. Plano, "Programs *CONGEN/ANTIC*," Rutgers University internal memo, April 1978.

[17] See for example the description of the program *PYTHYD* found in P. C. Trepagnier, Ph.D. thesis, M. I. T., Jan. 1975.

In order to check the consistency of the optical parameters as well as the reliability of the PEPR measurements the space track fits were projected into each of the three film views and the y residuals calculated for each measured point. The film plane RMS deviation (or FRMS) was found to be 5 microns (or roughly 100 μm in space). Thus the measured points were consistent to within one quarter of a bubble diameter.

4.5.2 Chamber Alignment

Since the origins in x of the two systems were chosen to coincide it was necessary to estimated five parameters. Those being the y and z translations and the three Euler angles of a generalized rotation between the two systems.

Based on initial parameters an iterative fit was carried out to determine the transformation. In each iteration the current estimate of the transformation was used in swimming each time slot to the vertex in its frame. Tracks which passed within 2 mm of the vertex were accepted and the difference in their intercepts and angles added to the fit. At the end of each pass through the data the values of each of the transformation parameters was updated.

In considering the effectiveness of this determination we will use the data set containing 285 tracks from roll 2259. We are interested here in verifying that the residual error between the two fits at the pseudo-vertex is representative of those fits alone. We expect that the RMS deviation in y to be dominated by the PWC prediction as the bubble chamber data has roughly 20 points measured to 100 μm in this dimension. We find the RMS to be 620 μm which is satisfactorily close to $\sigma^{PWC} = 577\,\mu$m. The other parameter which merits our attention is the rotation about the z axis as this has a direct impact on the momentum reconstructed for a given track. Here we find a angular RMS of 230 μr. We expect the wire chamber system to contribute 50 μr to this due to its moderate spatial resolution coupled with a long lever arm. Most of the dispersion is due to the rather short track length available in the 30" bubble chamber. A relatively long track of 50 cm would have an angular error of 100 μm/0.5 m = 200 μr. We conclude that the determination of the transformation matrix is well in hand.

Three independent data sets were scanned and measured in order to fit the transformation matrix under distinct conditions. In particular one fit was performed for each of the following segments of data: the MIT **A** rolls, the MIT **B** rolls, and the Rutgers **A** rolls.

4.6 ANALOG CALIBRATION

Because CRISIS is a fully analog device its calibration is more complex than that of the other wire chambers. Although techniques similar to those used for the drift chambers can be applied to finding its location and drift velocity, the charge calibration is quite another matter. This detector displayed wide variations in gain over the course of the run (some 20% peak-to-peak). Due to the size and time scale

of these gain shifts great care has been exercised in smoothing the detector response.

The following sections describe the procedures used in the gain calibration of this detector. The overall calibration has been divided into two areas. First the compensation for variation among the ADCs (Analog to Digital Converters) is described. Then the problem of systematic gain shifts is addressed.

In the following we will ignore the effects of capacitive cross talk between the sense wires. In the mean cross talk reduces the measured ionization by 4.6% in CRISIS.[18]

4.6.1 ADC Response

As is described elsewhere [19] a precision charge generator was used to evaluate the ADC response for each storage cell of each channel in CRISIS. The input charge Q_{IN} was best related to the the digitized value $Q^{i,j}_{ADC}$ by

$$Q_{IN} = a_0 + a_1 Q^{i,j}_{ADC} + a_2 (Q^{i,j}_{ADC})^2.$$

The indices (i,j) run over the 20 storage cells in each of the 384 channels. We note that the response was only mild non-linear. The typical channel deviated from linearity by 7% over the full scale. A typical value for the *pedestal* a_0 was -10 units of charge. The ADC had a full scale of 256 charge units. A typical track depositing 0.2 picocoulombs of charge registered at about midrange.

Due to hardware failures ten channels were not calibrated and have been removed from consideration.

In order to compensate for cell dependent gas gain effects beam tracks were used to find coefficients which normalized the relative response of each of the cells.[20] The resulting coefficients had an RMS deviation of 4%. Nine cells were found to require corrections of greater than 10%. These have been removed from further consideration, leaving 365 active data channels.

4.6.2 Smoothing Temporal Gain Variation

Two distinct gain variations can be observed in the CRISIS data. The first is a long term drift associated with atmospheric conditions. This drift was expected and is in principle easy to remove due to its time scale of hours. A second and unexpected short term, erratic gain shift has also been observed.

Figure 4.6 shows the 70% truncated mean ionization $\tilde{Q}$ for pion beams in a typical run A roll (2248) versus their frame number within the roll. These data have already been treated for the ADC response

---

[18] The author wishes to thank Tim Bolton for carrying out the cross talk calculation. By adapting the drift chamber field map program to the CRISIS geometry he was able to investigate the various inter-anode capacitances using a limited number of cells.

[19] D. Goloskie, et. al., op. cit.

[20] Ibid.

just described. We observe first a broad Gaussian distribution of the individual $\tilde{Q}_i$ about their mean. Second we see a dramatic (and yet unexplained) shift of the short term mean $\tilde{Q}$. The following describes a procedure developed to remove both the long term gain drift as well as the stochastic component.

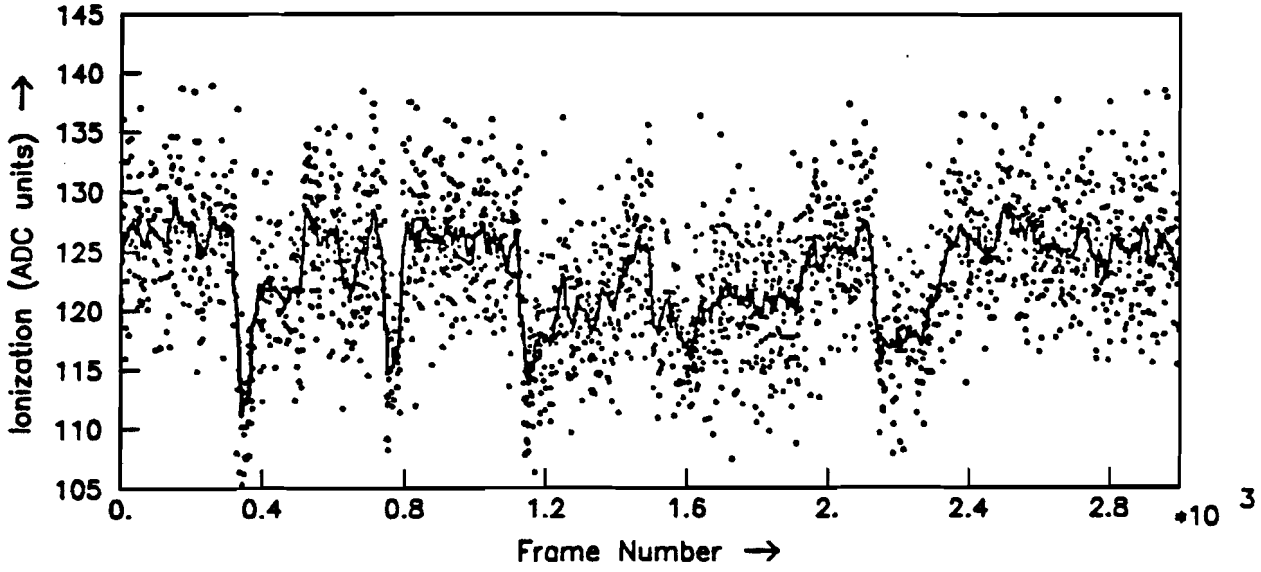

Figure 4.6 The truncated mean ionization for non-interacting pion beams versus frame number for roll 2248. Note the erratic component underlying the otherwise random variation.

Although the autocorrelation series for this data fit the criteria for treatment by time series technique[21] a more pedantic approach has been taken due to the on/off nature of the shifts.

A modified version of the program *SURVEY* was used to store the ionization measurements for each roll of film. The ADC calibration was enforced and the mean of the 70% smallest signals was calculated for each track identified as a pion by the Čerenkov counters. A smoothed representation of the series was then obtained in a two step process.

Due to the square wave character of the shifts a simple running average is inappropriate as the trend will always lag the point under consideration. For this reason an average was chosen which would both lead and lag the desired point. For each point in the series the sum

$$k_{1,i} = \frac{\sum_{j=i-l_1}^{i+l_1} \tilde{Q}_j}{2l_1 + 1}$$

[21] M. G. Kendall and A. Stuart, "The Advanced Theory of Statistics," (London: Charles Griffin and Co. Ltd., 1968), vol. 3.

was formed about each data point i. Then

$$k_{2,i} = \frac{\sum_{j=i-l_2}^{i+l_2} k_{1,j}}{2l_2+1}$$

was evaluated. The choice of a double smoothing as well as the combinations

$$l_1 = 10, l_2 = 25 \qquad \text{(runA)}$$

$$l_1 = 80, l_2 = 80 \qquad \text{(runB)}$$

was a purely subjective one. As can be seen in the illustration this combination has sufficient response to the gain shifts (due to a small l_1) while maintaining a reasonably flat response during stable periods (due to a larger l_2).

The overall gain from this procedure is a reduction of variance $\sigma_{\bar{Q}}$ of 25% for a typical roll. This is shown for the above mentioned roll in figure 4.7.

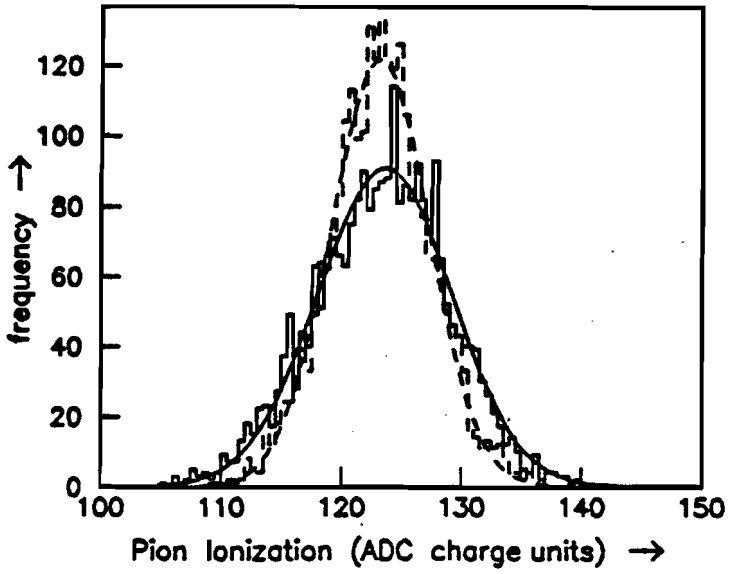

Figure 4.7 The solid line and histogram show the distribution of truncated mean ionization for roll 2248 after the ADC and cell-to-cell corrections. The dashed curve and histogram show the result of also applying the smoothing described in the text.

It has been observed that the short term gain shifts were not present during the run B data taking. In response to this the smoothing time constants were increase in order to reflect the longer time scale of the gain variation. We see in figure 4.8 the behavior of the gain for roll 1950. This displays the slow changes expected from variation of atmospheric conditions.

Having carried out the gain calibration we have investigated the ionization loss probability distribution function using CRISIS. The distribution of corrected ionization measured for all of the hooked

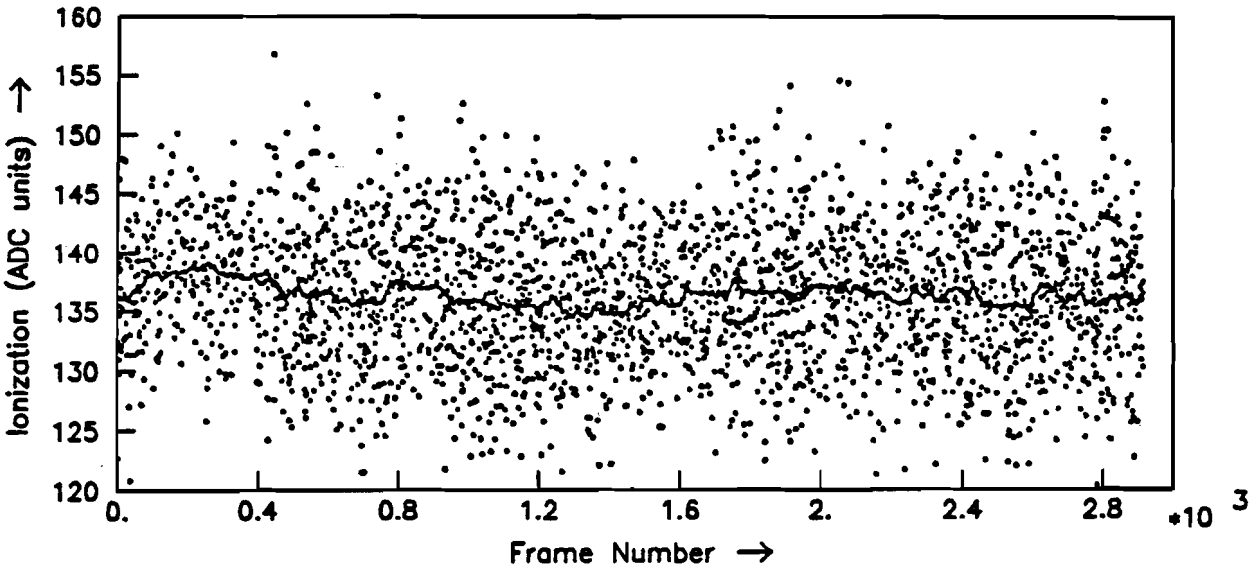

Figure 4.8 The truncated mean ionization for non-interacting pion beams versus frame number for roll 1950. This spectrum is dominated by the expected environmental effects.

up (i.e. non-interacting) pion beams of roll 2299 is shown in figure 4.9. This sample consists of some several hundred thousand individual ionization measurements. The break in the tail above 240 units is an artifact of calibration due to one's inability to recover information from the overflow bin. Plotted along with the data is a maximum likelihood fit to the data of the energy loss distribution function $f(\Delta)$ described in appendix C. The fit estimated both the conversion factor between measured charge and theoretical energy loss and the offset in the energy scale. Thus the parameters $\tilde{\epsilon}$ and $\tilde{\Delta}_0$ were found which maximized the likelihood $L(\epsilon, \Delta_0)$ under the relationship

$$Q = \epsilon \cdot (\Delta - \Delta_0).$$

The likelihood was evaluated on a series of grids of points in (ϵ, Δ_0) in order to locate the maximum. $L(\epsilon, \Delta_0)$ was evaluated using the binned distribution so that it had the explicit form

$$L(\epsilon, \Delta_0) = \prod_{i=qmin}^{qmax} (f(Q_i/\epsilon - \Delta_0))^{n_i},$$

where the domain of the fit was specified on $(qmin, qmax)$ and n_i was the content of bin i. The final result of this analysis gave $\tilde{\epsilon} = 0.0453\,\text{eV/q-unit}$ and $\tilde{\Delta}_0 = 756\,\text{eV}$.

4.7 BEAM TRACK STUDIES

Prior to discussing event reconstruction we can comment on the integrity of the various calibration parameters. In order to do this we will examine non-interacting beam tracks.

4.7.1 Beam Momentum

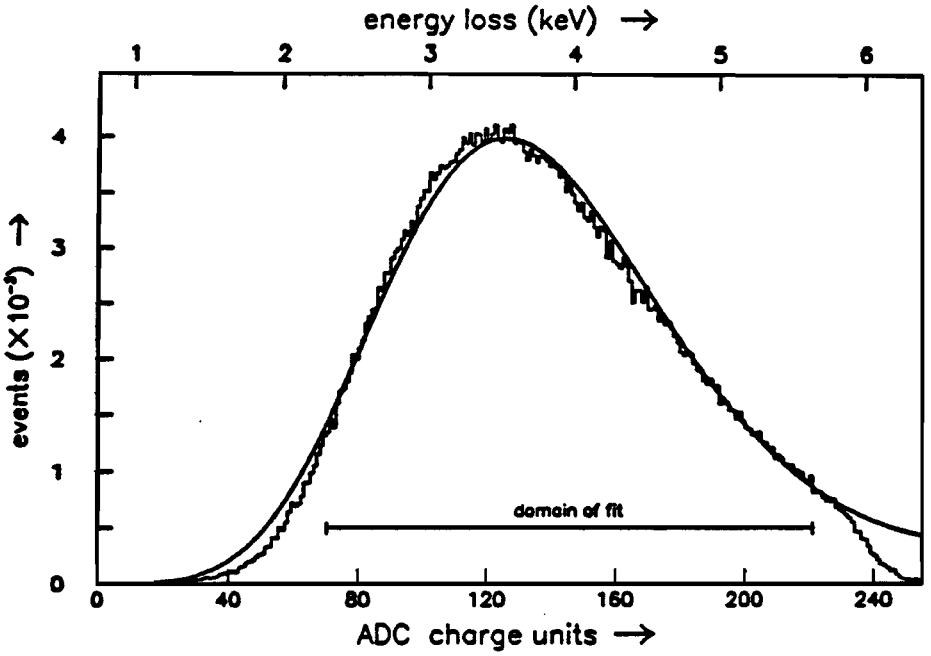

Figure 4.9 The distribution of corrected ionization measurements. Also plotted is the result of a fit to the data as described in the text.

The determination of the beam momentum serves two significant purposes. First it measures a quantity for the experiment and second it illustrates the quality of the survey parameters.

As a charged particle traverses a magnetic field it is deflected according to $\int B \cdot dl$. By measuring the deflection of straight through beams one may determine the beam momentum. In the discussion so far we have assumed a value for the beam momentum. This is necessary in order to be able to trace the particle trajectories through the magnetic field and predict their locations for the downstream survey. The value used for the beam momentum above was the result of the following measurement. In order to obtain a survey which was not biased by the input value of the beam momentum, data were collected with the bubble chamber magnet turned off. This allows all beams to be treated as straight lines when swimming through space.

In order to obtain results of the highest quality special data sets were taken for surveying purposes. During roll 2300 the final focus of the beam was changed so that the beam profile was a circle of radius 8 cm at the bubble chamber. This served to illuminate larger portions of the wire chambers than normally obtained with the run beam profile. The *spot* beam also allows more precise determination of the PWC-BC transformation matrix due to the greater range of the z coordinate. Spot beam data were taken with the magnetic field off and with the field on. In the following we will discuss a set of 500 frames of field-on data and a set of 500 frames of field-off data. It is significant to note that these data sets were taken one directly after the other to minimize any other affects.

One may think of the downstream segment of the x-axis as an independent line in space. The concept of a downstream wire chamber axis has been used to determine the beam momentum in the following way. A survey of the field-off data was used to determine the nominal downstream axis. Since this run had zero magnetic field the survey results are independent of the imposed beam momentum $\tilde{p}$. Next a survey was performed using the field-on data. Since this data was taken with the magnet on the chamber locations are sensitive to $\tilde{p}$. If $\tilde{p}$ were to have the value of the true beam momentum none of the chamber locations would change, within errors, between the two runs. As the magnetic field is directed along the z-axis an arbitrary $\tilde{p}$ will 'deflect' the new downstream axis in such a way as to vary its y-slope relative to the nominal axis. Setting aside for the time being considerations of the error introduced by the uncertainty in the path integral of the magnetic field we now consider how to evaluate the beam momentum.

For a given $\tilde{p}$ *SURVEY* constrained the chambers to fall along the line traced out by a particle incident along $\hat{X}_{PWC}$ and swum through the magnetic field. The slope of the downstream axis is clearly a function of the imposed beam momentum. It is then possible, by varying $\tilde{p}$, to obtain another downstream axis which coincides with the initial field free axis. The value of $\tilde{p}$ used for this run will be the true beam momentum.

A series of field-on runs have been made which imposed a variety of incident momenta. For each run the orientation of the resulting downstream axis was fit relative to the nominal field-off axis. Each relative axis was described by the four parameters $(\delta y_0, \delta a_y, \delta z_0, \delta a_y)$. The results of these runs in the bend plane are summarized in figure 4.10. We see that the relative y-slope (δa_y) of the downstream axis does indeed depend linearly on the imposed beam momentum. By fitting the plotted points to a straight line the zero crossing has been determined to occur at $198.2 \pm 0.2_{1\sigma}$ GeV/c. The quoted statistical error derives from the error propagation of $\sigma_{\delta a_y} = 7\mu$r found by the linear fit. It is of interest to point out that in all of the fits the results are consistent with an error due to the wire chamber survey of $\sigma_{\rho_0} = 40\mu$m for each of the planes in the downstream system.

4.7.2 Hybridized Beam Tracks

The first independent test of the survey parameters for the entire spectrometer is the reconstruction of beams tracks using information from all the wire chambers, the bubble chamber, and CRISIS. This section describes studies performed on such a sample of beam tracks.

4.7.2.1 Track reconstruction

A set of one-prong beam tracks (§4.5) from roll 2245 was passed through the normal chain of programs used in event reconstruction. This produced a sample of 151 fully hybridized tracks. The reconstruction programs are to be discussed in detail in the following chapter. We mention here for the advanced reader that after reconstructing this sample of tracks with PIG they were forced through SOW as a test of this

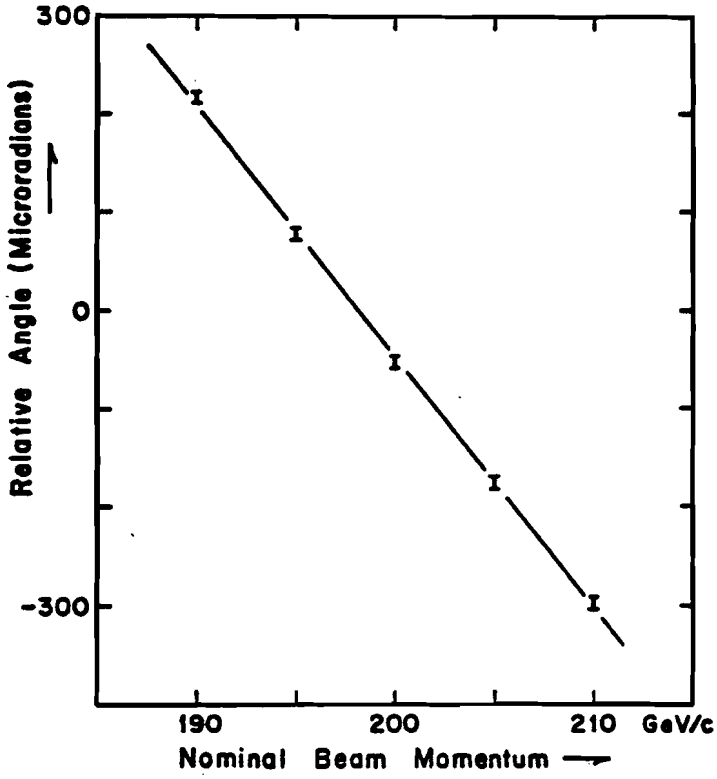

Figure 4.10 The relative angle between the upstream and downstream axes as a function of the hypothetical beam momentum.

algorithm. This resulted in SOW locating 96% of the tracks.

During the part of the run under consideration 14 of the 16 wire chambers were instrumented and taking data. The PIG run found an average of $11 \pm 1_{RMS}$ wire chamber hits per track. By design a PIG fit has three constraints other than those provided by the wire chambers. As we are estimating four parameters in the field free downstream spectrometer this means that the typical PIG fit had 10 degrees of freedom. The SOW run found an average of $10 \pm 3_{RMS}$ hits per track. Under normal circumstances the PIG and SOW algorithms are run in succession in order the achieve the highest track finding efficiency.

4.7.2.2 Detector resolution

In order to illuminate the performance of the spectrometer elements we may examine the fit residuals from the highly constrained PIG beams. The various constraints which contribute to a PIG fit may be summarized as a vertical line through the BC vertex, PWC wire hits, DC wire hits, and two degrees of freedom resulting from a CRISIS plane fit, namely an intercept and a slope. Table 4.5 summarizes both the input and achieved resolutions for the various detector degrees of freedom in a PIG fit. Because these fits are well overconstrained these estimates are essentially unbiased. We observe that each of

the detectors has behaved at least as well as expected. Note that the CRISIS intercept input error is very conservative in order to offset certain systematic errors. One can calculate that the RMS deviation expected for this detector alone should be 712 μm in agreement with the measured value. The bubble chamber RMS residual seems to be significantly smaller than expected. Because the vertex is almost two meters from the first wire plane we realize that this degree of freedom can in fact bias the fit. The affect on track parameters is nonetheless small.

TABLE 4.5		
DETECTOR RESOLUTION		
D.O.F.	fit input	RMS residual
σ_{xv}^{BC}	350 μm	270 μm
σ_{p}^{PWC}	577 μm	523 μm
σ_{p}^{DC}	200 μm	170 μm
$\sigma_{int.}^{CR}$	$\approx$1.2 mm	709 μm
$\sigma_{ang.}^{CR}$	$\approx$150 μr	161 μr

This sample of reconstructed tracks also serves to illuminate the performance of the wire chambers in terms of their efficiency. We find that the efficiencies ranged from 60—99%. The average PWC efficiency was 77%, while the average DC efficiency was 85%. We note that each of the first two PWCs and the first four DCs operated at better than 95% efficiency. Because of the geometry of the FHS the first PWC doublet and the first DC triplet are the most important elements involved in momentum determination as well as *paging*.

4.7.2.3 Momentum resolution

Using the PIG data set we may examine the spectrum of reconstructed momenta. The combination of survey parameters and reconstruction programs obtained a value for the beam momentum of $195.9 \pm 2.2_{1\sigma}$ GeV/c. This number is in adequate agreement with the nominal value of 198.2 GeV/c. The RMS deviation of the momentum spectra is $\sigma_p = 26.8$ GeV/c. This number was calculated after dropping 13 tracks which were judged to be outliers with momenta more than 80 GeV/c from the mean. This number is indicative of the largest momentum error as for a magnetic spectrometer $\frac{\sigma_p}{p} = \kappa p$. We then have determined

$$\kappa = \frac{\sigma_p}{p^2} = 6.7 \times 10^{-4}.$$

It is important to note what effect this value of κ will have on the Physics capabilities of the spectrometer. In terms of the familiar center of mass kinematic variables Feynman X and rapidity we obtain $\sigma_{x_f} =$ 0.2 units and $\sigma_{Y^*} = 0.3$ units.

The major contribution to σ_p comes from the bubble chamber part of the fit. The very small sagitta of the beam track combined with the low resolution of the scanner's pseudo-vertex cause large errors in the determination of the track slope at the vertex. A track's momentum is fundamentally determined by the angle through which it turns in the magnetic field as it travels from the vertex to the wire chambers. Hence the bubble chamber angular resolution enters linearly into the momentum resolution. For the purpose of illustrating the wire chamber spectrometer one may ignore the bubble chamber information and compare the upstream track fit with that of the downstream. For the PIG sample the change in slope of the tracks as they pass through the analyzing magnet has been evaluated. This is accomplished using the upstream and downstream wire chamber track fits alone. The hybrid fit is disregarded in this study. The angular reflection has been examined in both the bend plane (δa_y) and the non-bend plane (δa_x). These distributions give $\sigma_{\delta a_y} = 176\,\mu r$ and $\sigma_{\delta a_x} = 140\,\mu r$. As all effects are identical for the two directions except for those due to the magnetic reflection we expect that the larger RMS in the bend plane is due to the beam momentum dispersion. We take $\sigma_{\delta a_x}$ as the instrumental error and remove it from $\sigma_{\delta a_y}$ to obtain the dispersion due to the momentum byte $\sigma^{beam}_{\delta a_y} = 107\,\mu r$. Error propagation gives $\sigma_p = 4.2\,\mathrm{GeV}/c$ or 2.1% in complete agreement with the value defined by the beam optics (§2.1.4).

We next re-evaluate κ using only the wire chambers and removing the effects of the beam dispersion,

$$\kappa = \frac{\sigma_p}{p^2} = 1.4 \cdot 10^{-4}.$$

This value of κ reflects the error introduced by both lever arms of the FHS and the full deflection of the magnet.

4.7.3 Ionization Loss Near the Fermi Plateau

As we have already seen non-interacting beam tracks were used to perform the gain calibration of CRISIS. At this time we would like to comment on the results of that calibration. For this study a collection of some $5 \cdot 10^4$ beams was collected from ten rolls. These tracks were both identified in the Čerenkov counters and judged to be non-interacting. Each of the calibration steps mentioned in §4.6 was carried out in order to correct the ionization information. We see in figure 4.11 the resulting distributions of ionization drawn by beam type.

Table 4.5 summarizes the detector resolution. The most important result is that CRISIS has achieved a 9.2% (FWHM/mean) resolution. This value is some 25% larger than the theoretical limit of 7.5%.[22]

4.8 OPTICAL ROTATION ANGLE

[22] W. W. M. Allison and J. H. Cobb, "Relativistic Charged Particle Identification by Energy Loss," Ann. Rev. Nucl. Sci. 30 (1980) 253.

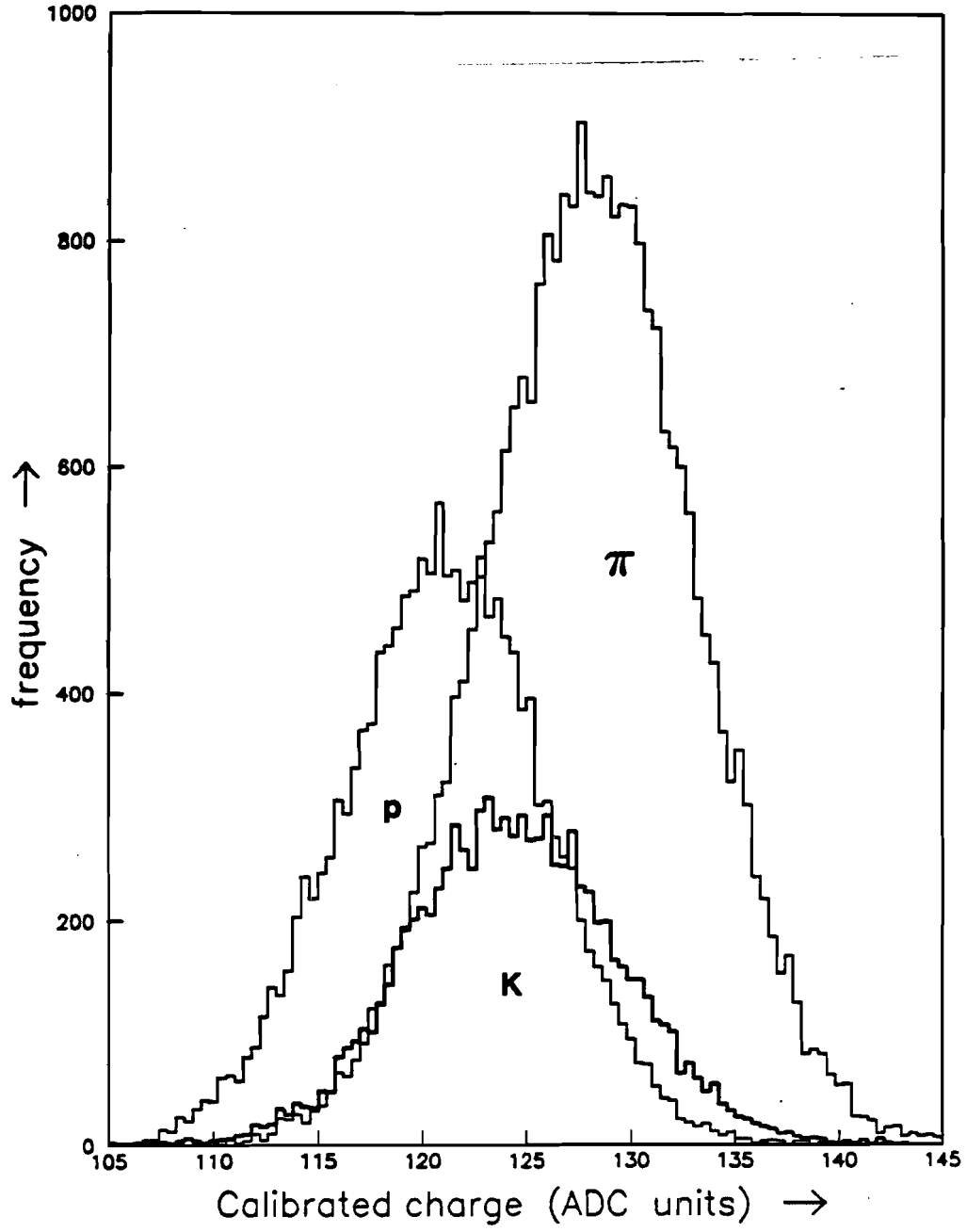

Figure 4.11 The distribution of truncated mean ionization losses for non-interacting, identified beams. These data have been processed through each of the gain corrections. The Čerenkov tags are displayed below the appropriate curves.

During the E570 run the 30" bubble chamber was expanded six times during the one second long slow spill. It has been observed previously[23] that this rate of expansion and recompression has a degrading effect on the hook up of tracks between the bubble chamber and the wire chambers. It has been demonstrated that an instability exists in the observed relative angle between the two systems in the bend plane. This was originally brought to light in E299 by two observations. First the diffractive two prong events were being reconstructed at other than the beam momentum. And second the reconstructed visible energy in the four and six prong events did not peak at the beam momentum. It was found that one could correct this behavior by measuring the angle between the upstream PWC system and the apparent orientation of beams in the bubble chamber on a roll by roll basis. A phenomenological rotation of the bubble chamber was then imposed prior to event reconstruction.

It has been observed in E570 that just such an effect is present. By using a program similar to the one described in §4.5.1 one was able to reconstruct the matched ionization reference track which was measured for each frame with an accepted event. The associated PWU time slot was swum into the bubble chamber and the relative angle between the bubble chamber and wire chamber fits was calculated. The average value of the relative angle was used to effectively realign the two coordinate systems on a roll by roll basis. The PWC-BC transformation matrix was thus updated by *GEOHYB* for each roll processed. We note that the angle was at most a few tenths of a milliradian.

[23] Seog H. Oh, Ph.D. thesis, M. I. T., May 1981, pp17–19.
Thomas B. Stoughton, Ph.D. thesis, M. I. T., June 1981, pp.17–19.

Chapter 5

EVENT RECONSTRUCTION

The previous chapter described the procedures used in preparation for event reconstruction. We observe that two distinct undertakings were at hand. The bubble chamber film had to be scanned and measured in order to make their event related track data available. And just as importantly the non-interacting beams were used to locate and otherwise characterize each of the detectors. The early part of the current chapter deals with the process of collecting all the facets of data related to a particular event. This is followed by a brief description of the event reconstruction algorithm. Finally the actual event reconstruction processing is summarized.

The programs to be described in this section descend from a collection of software maintained in the CERN PAM library. This material was developed and used by experiments in both the U.S. and Europe. Modifications were made to optimize performance for the FHS geometry.

5.1 PREPROCESSING

Prior to reconstruction an independent program was used to assemble event data into a single structure.

5.1.1 Time Slot Assignment

The event preprocessing program was appropriately named *PRECIS.*[1] Its function was to associate a measured bubble chamber event with its electronic data.

As was mentioned in §2.2 once the event vertex has been reconstructed in space it could be matched with its electronic time slot. The vertex location was fit with the processor *CC* to be described later. Then the beam track in each time slot was fit in PWU and swum through the magnetic field to the x coordinate of the vertex. If a unique track was found which had y and z impact parameters of less than 2 mm the time slot was associated and processing continued. Otherwise the event was rejected.

5.1.2 Bank Creation

Each of the FHS programs used the CERN HYDRA dynamic store to hold event and spectrometer related data.[2] Related information were associated into the fundamental storage unit referred to as a *bank.* The banks were arranged in a *tree structure.* The branches of the tree (*links*) describing the type of banks which they supported. An extended system of pointers (*reference links*) allowed rapid association between disparate parts of event data.

5.1.2.1 Bubble chamber

At this stage of processing the bubble chamber data had already been organized into a bank structure.[3] For each view a bank contained the measured locations of the fiducials for the frame. Then a series of banks describe the track measurements from the automatic measuring machine. A final bank contained data for a non-event related ionization reference track.

5.1.2.2 Wire chambers

All of the wire chamber data for a time slot was organized into a collection of banks. For the drift chambers this could include data from a different time slot due to their maximum drift time.

PRECIS used the roll by roll *SURVEY* results in order to convert wire addresses and drift times into locations in space.

5.1.2.3 CRISIS plane finding

The CRISIS data was organized into raw banks containing charge and time data. Then the ISIS

---

[1] The Oxford English Dictionary ascribes the meaning "to abstract" or "summarize" to the transitive use of précis.

[2] See R. Bock, et. al., "HYDRA Topical Manual MQ: Basic HYDRA," CERN Program Library, Geneva, October 1981.

[3] R. J. Plano, "*GEOHYP* Exterior Banks," RIHSC 82-12D, Rutgers Univ., Oct. 1983.

processor[4] was called to locate and fit lines to the drift time versus cell number information. As the pattern recognition and fitting aspects of this package are fully documented elsewhere it will suffice to mention that the end result was a list of banks which described the location and orientation of all plausible planes. Also associated into banks was the charge data related to each plane. Charges that were common to crossing planes were removed at this time.

The functions of the plane finding processor are best illustrated by example. In figure 5.1 we see the time data recorded by CRISIS for a single time slot. We see the drift times recorded by each of the 394 cells in the detector. The lower edge of each entry indicates the time of arrival of the hit, while the height represents the time over threshold for the collected charge sample. One should recall the geometry of the two drift spaces (§2.4.3) when interpreting the drift time data. The upper plot shows the raw data taken by the self-triggering electronics. The minimum of time in each half is at the sense plane and so we see from the two shallow V-shapes that one track crossed each sense plane. The deep V-shaped feature is a slow electron which was ejected from the upper high voltage plane.

The lower plot shows those hits which were associated into unique planes. Hits shared by two planes have been removed to maintain the integrity of the ionization measurement. The extraneous hits have been removed. Also note that hits shared with many of the extraneous plane fragments have been removed as well.

This CRISIS data is unusually clean, especially when we consider that this time slot was associated with an interaction of charged multiplicity 16. It was not uncommon, however, for the CRISIS data to be significantly degraded by accidental tracks such as those produced in a secondary interaction in the exit window or by scraping of a magnet face. Figure 5.2 illustrates this point for a 6 prong event.

5.2 THE HYBRID GEOMETRY PROGRAM

The event reconstruction algorithm was realized in a specially modified version of the program *GEOHYB*. This program consisted of a series of interrelated algorithms all directed toward the common goal of providing the most complete description of the event kinematics given the data as recorded.

This section is intended as a brief introduction to the track reconstruction problem and its solution as applied to E570. The level of treatment is geared toward illustrating those areas which have the greatest impact on the Physics goals of this thesis. Let the reader be warned that this discussion is far from complete.

5.2.1 Program Components and Flow

[4] D. Goloskie, et. al., op. cit.

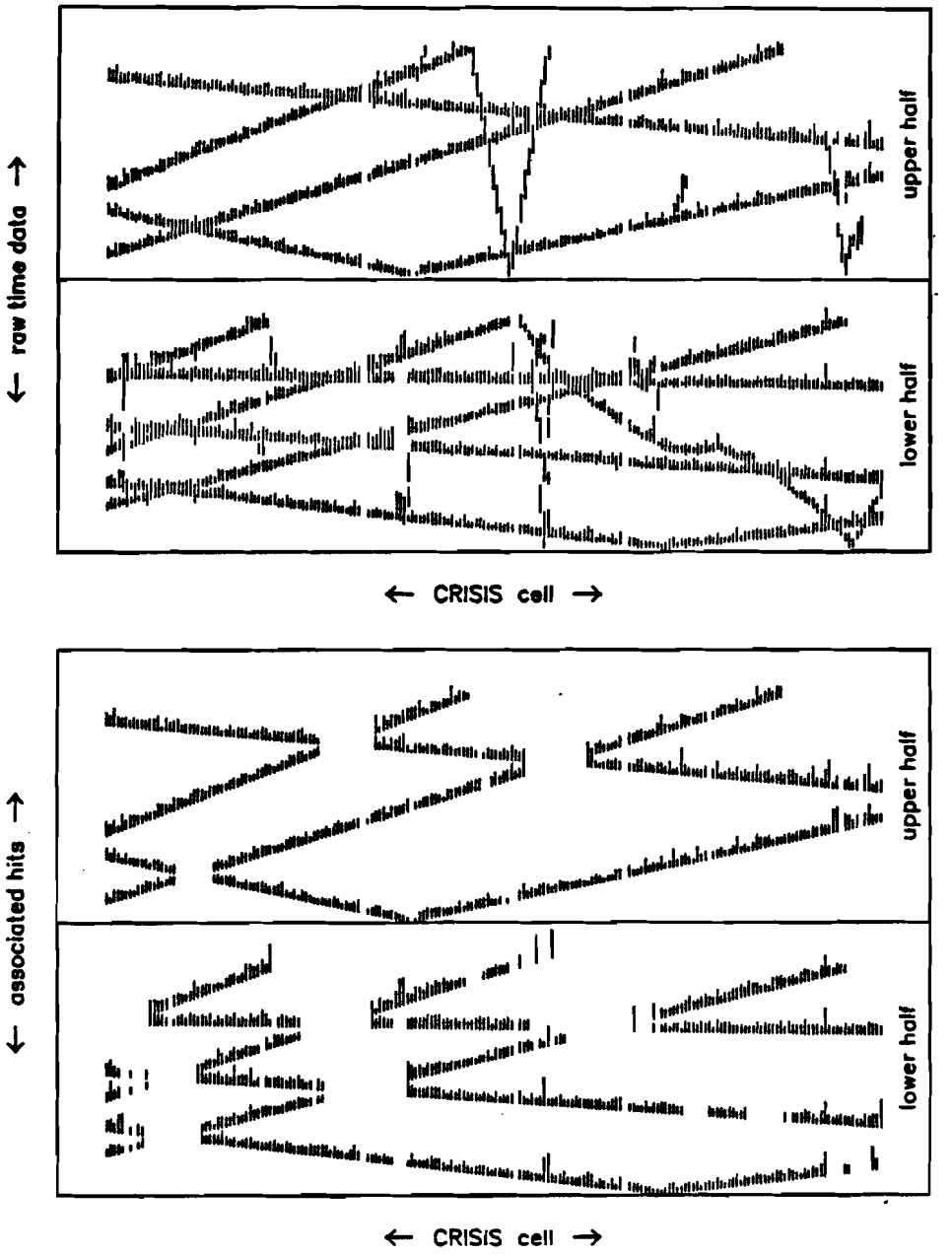

Figure 5.1 Two stages in the processing of CRISIS time data. The upper plot displays the raw times, while the lower contains only those hits which were associated with planes by the *ISIS* processor. These data are from roll 2245, frame 394272, time slot 3 and were produced by a 16 prong interaction in the bubble chamber. In terms of drift distance we note that the horizontal scale is compressed by roughly a factor of four over the vertical.

The major components of *GEOHYB* were HYDRA *processors*. HYDRA accommodates re-entrant subroutines in FORTRAN via the processor. An internal stack is created and arguments are passed by special *call banks* when a processor is invoked. HYDRA also provides facilities for servicing conditional branches beyond those allowed by FORTRAN alone. This feature is especially useful for event oriented

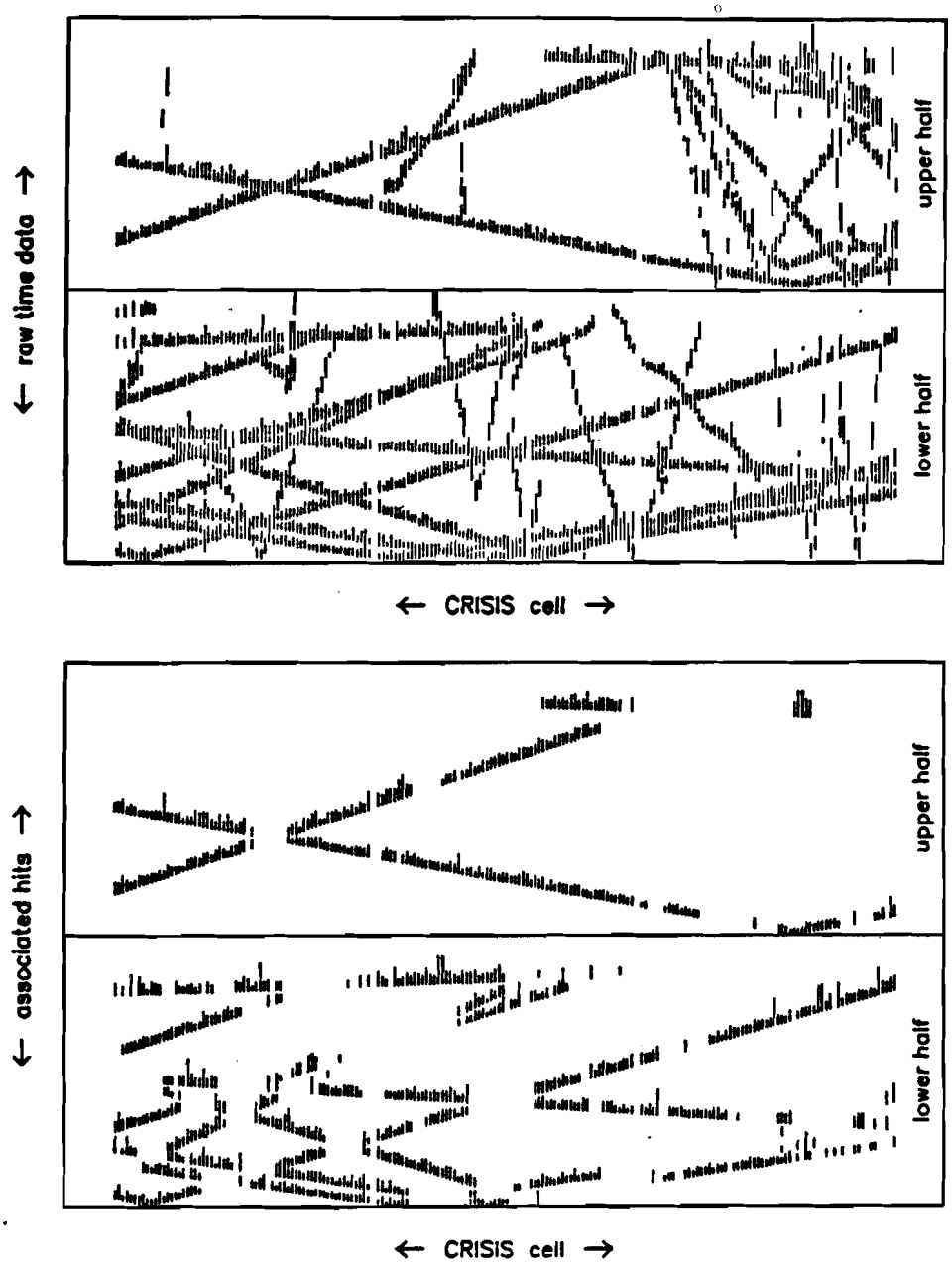

Figure 5.2 We see here the data recorded for roll 2245, frame 393760, time slot 3, which was associated with a 6 prong interaction. This data clearly contains many tracks not directly associated with the bubble chamber event. The consequent loss of information in this not unusual situation places limitations on the overall usefulness of this detector.

processing. Much of the HYDRA system has nonetheless become outdated due to developments in computer software and hardware. The trapping of mathematical exceptions as well as event timing were handled at the system level.[5]

[5] The author is indebted to Dr. James Bober for his assistance in this area.

Aside from some minor preparations the program proceeded in four major steps. First the vertex was located. Tracks were then isolated by iterative fitting in the downstream system. These tracks were then matched with their images in the bubble chamber and an overall fit was performed (*hybridization*). Data associated with these tracks was removed from further consideration. Next the remaining bubble chamber images were sorted and fit to helixes in space by a three view geometry program. Finally bare bubble chamber tracks which were of sufficient momenta to enter the downstream system were iteratively swum out to locate associated hits which might remain in the wire chambers. Acceptable hits were then used in a hybrid fit.

The order of processing was motivated by the folding of secondaries into the forward jet due to the center of mass motion in the lab system. By using the bubble chamber alone one is unable to associate images reliably among the three views into correct tracks. A track fit in the wire chambers could, however, be used to point out its associated image in each view. Having removed the fastest particles each of the remaining tracks could be reconstructed using a traditional geometry program. This was now possible because there were fewer images present, each of which had lower momenta and was thus more likely to provide unambiguous matches.

There were in all three distinct algorithms used in track reconstruction. We will refer to these as PIG, BBC, and SOW for very dim historical reasons. The PIG algorithm hybridized tracks directly from the spectrometer. This technique was directed toward tracks which traversed at least part of the dE/dx detector. As such only tracks reconstructed with PIG are available for possible identification. BBC refers to the bare bubble chamber code best suited to low momentum tracks. SOW was used to hybridize tracks of intermediate momenta which entered the spectrometer, but failed to reach the dE/dx detector.

5.2.2 Vertex Reconstruction

The estimation of vertex parameters represents one of the most difficult tasks in the process of event reconstruction. Due to the complex relationship between the vertex parameters (x_V, y_V, z_V) and the track parameters $(1/p, \Lambda, \phi)_i$ a familiar bootstrap approach has been taken in determining the vertex location. Each step in this process contained greater and more highly refined information such that the final estimate was in fact quite reliable.

The processor *PFT* (point fit) via *PM* (point match) was used to determine a zeroth order estimate of the vertex from the scanner's measurements. The measured point on each film plane was traced back through the optical system in order to determine its classical light ray within the bubble chamber volume. A χ^2 fit was then performed to evaluate the point of closest approach of the three light rays. The film plane estimates were updated by projecting this space point back into each view.

Having correlated the scanner's measurements a simple parameterization of the film plane images

was used to locate their point of intersection. The processor *CC* (concave) evaluated a film plane vertex independently for each view. This was accomplished by first fitting each image to a circle and then locating the point closest to the current vertex estimate and the fit trajectories. *PFT* then determined a new space point.

It was at this stage that track reconstruction was undertaken. The full set of reconstructed trajectories in space was then used by the processor *CV* (convex) fit their common intersection point. Because the vertex and momentum were artificially decoupled by the choice of algorithm steps were taken to eliminate bias in the various fits. A comparison was made between the *CC* and *CV* vertex estimates. If a significant shift occurred in either the x_V or y_V coordinate the entire track reconstruction algorithm was reentered with the new vertex. If on the other hand the error estimate σ_{y_V} was significantly reduced by *CV* the reconstruction algorithm was reentered at the level of the hybrid fit. The reasons for these choices will become more apparent as the track reconstruction algorithm is described in the following sections. In simple terms both tests seek to eliminate bias in the wire chamber track fits and the bubble chamber track matches due to a poor initial vertex estimate.

5.2.3 Wire Chamber Track Finding

The track finding problem in E570 was made particularly difficult by the number, orientation, and location of the wire chamber planes. The ability to recognize tracks was made practical by exploiting the enormous redundancy of the dE/dx drift time measurements.[6] As we have already mentioned the *ISIS* processor located into planes each track which crossed its volume. This pattern recognition process formed the rudiments of the track reconstruction due to two important facts. First every real, event related secondary track must originate at the event vertex. And second (with high probability) each CRISIS plane corresponds to some real track. Thus we may redefine the track finding problem in terms of the location of all wire hits consistent with the event vertex and a given CRISIS plane.

It is important to realize just what information each detector contributed to the fit. CRISIS provided a hypothetical track intercept y_0^{CR} and slope a_y^{CR}. Since the chambers were in a field free region the trajectories were straight lines. One could not, however, make use of the bubble chamber vertex y coordinate y_V as the magnetic deflection had yet to be determined. In the non-bend plane we are nonetheless certain that each real, event related secondary track will pass through the line described by (x_V, z_V).

In terms of a track fit (§4.3.3) we thus far have three constraints to be found in the CRISIS intercept and slope and the bubble chamber vertex. (As the vertex constraint is a line in space just as a wire hit we will refer to it as the vertex pseudo-wire in the following). The addition of any linearly independent

[6] I. A. Pless, op. cit.

wire hit will provide the fourth constraint needed to parameterize a candidate track. Since we are still in the process of isolating tracks we have no confidence in a zero constraint fit. In general we desire that a track hypothesis be greatly overdetermined before we accept it as a real track. This brings us to the actual track finding algorithm.

Up to this point we have seen the first level of pattern recognition which has yielded three course degrees of freedom. Presently we discuss the final pattern recognition used to isolate tracks by iterative fitting.

The processor *FARM* contained the steering for wire chamber track finding. At its disposal were two algorithms for locating tracks. The first (COW) was restricted to searching for tracks using the PWC and DC data only. The second (PIG) incorporated information from the bubble chamber and CRISIS. COW was not used in the event processing.

PIG selected a CRISIS plane and undertook a search for hits consistent with a track in a preselected group of n wire planes. For each n-tuple of hits a full χ^2 fit was made to the $n+3$ constraints. If the fit χ^2 was inconsistent with a track the next n-tuple was tried. If on the other hand the χ^2 was favorable the unused wire hit banks (i.e. those other than the group of n planes) were scanned for hits consistent with the current trajectory.

The process of *picking up* additional wires was highly refined in its abilities to select data and to eliminate outliers. If necessary a series of fits was undertaken to be certain that all and only those hits consistent with the developing trend were maintained as candidate elements. If at this point a candidate did not have at least four wire hits it was dropped and the next n-tuple tried, otherwise processing continued to refine the candidate.

Up to this point drift chamber hits which were within the first few millimeters of a sense wire were excluded from consideration. This was due to the possibility of unrecoverable track misguidance owing to the left-right ambiguity. After the initial wire pick up the track parameters were well enough defined to resolve close drift hits even within a few σ^{DC} of the sense wire. Any such hits were added to the fit at this time.

For a given CRISIS plane only one track was located, eventhough two tracks could in fact lie within the resolving distance of the detector. (This is of no practical consequence as the associated charge data for strongly overlapping tracks is of no value). Two estimators were used to discriminate between candidates derived from different n-tuples for the same plane. The overriding consideration was the the candidate have the greatest number of hits. For two candidates with the same number of hits the one with the smaller χ^2 was kept.

If after all n-tuples had been tried the best candidate for a plane had an unlikely fit χ^2 it was

dropped. If a candidate was accepted a bank containing the track fit was created. The used CRISIS plane and wire hits were then eliminated from further consideration by the tracking algorithm.

The above procedure was carried out for each CRISIS plane and for all plausible image planes. Image planes are the reflection of a plane in the sense plane and are due once again to the left-right ambiguity.

Operationally PIG was executed two times (the passes are referred to as PIG-A and PIG-B). This allowed distinct n-tuples to be used in the initial fits and added substantially to the effectiveness of the algorithm. PIG-A started fitting with pairs of wires selected from among the six drift chamber planes downstream of CRISIS, while PIG-B chose pairs from the three drift chamber planes upstream of that detector. The A pass was intended to locate the tracks which traversed the entire DPI. The B pass could then locate the wider angle tracks which only passed through a part of CRISIS. Note that by removing the hits associated with the long tracks in PIG-A both the combinatoric and pattern recognition burdens of PIG-B have been diminished due to the reduction of the number of hits where their areal density was highest. If no tracks were accepted in either PIG-A or PIG-B a special PIG-C pass was entered which started fitting with hits selected from among the seven PWC planes.

5.2.4 Wire Chamber Track Hybridization

The *FARM* produced a chain of banks containing wire chamber track fits consistent with the primary vertex. It was the task of the processor *STDW2* to associate these tracks with their bubble chamber images and to carry out the hybrid fit utilizing both the bubble chamber and wire chamber data.

The association between wire chamber track fit and bubble chamber film plane images was made by projecting the particle's trajectory onto each film plane and choosing the best match in each view. In order to trace the trajectory in the magnetic field a first estimate of the momentum was obtained by *DTA* (detector track approximation). The particle's charge was assigned based on the event geometry and a binary search in momentum was carried out. At a given momentum value the wire chamber fit was swum back through the magnetic field to x_V and the y impact parameter between the vertex and the track was calculated. The search continued until the impact parameter was less than the position error typical of a track fit. The approximate values $(1/p,\Lambda,\phi)$ thus obtained were then used to swim out from the vertex in order to produce film plane images of the candidate trajectory.

For each image in a view the difference in y_{film} was calculated (by *TIH*, track image hooking) between the hypothetical arc and the measured points. A single estimator was formed which was sensitive to both the mean shift and the mean absolute shift between the tracks. In this way the selection was based on the relative shape as well as the relative position of the images. A list of acceptable images was generated for each candidate.

The final hybrid fit (*HFT*) for PIG tracks used the bubble chamber vertex, the film measurements in the form of light rays, and the downstream track fit intercept and slopes. Having initial estimates for all parameters an iterative, linearized fit was undertaken in the seven (difference) parameters ($\Delta(1/p)$,$\Delta\Lambda$, $\Delta\phi$,Δy_t,Δz_t,$\Delta\Lambda^{MS}$,$\Delta\phi^{MS}$). Each pass through the data calculated the changes in:

$1/p$	inverse momentum
Λ	dip angle
ϕ	phi angle
y_t	y impact parameter of track at vertex
z_t	z impact parameter of track at vertex
Λ^{MS}	dip multiple scattering angle in exit window
ϕ^{MS}	phi multiple scattering angle in exit window.

As implemented the fit was arbitrarily stopped after two iterations. Fits which resulted in a poor χ^2 were dropped.

Thus far in the discussion of *STDW2* we have ignored the possibility that two (or more) film plane images may be consistent with a given wire chamber track fit. In such an event all combinations of the accepted images were processed through *HFT* independently. It is also possible for two wire chamber track fits to be consistent with a single image. Therefore all wire chamber track fits were processed as above before a decision was made as to the final track match assignments.

The processors *PTSE* and *PTDC* were used to make the final match decision consistent with the unique assignment of the greatest number of images. The images thus matched and fit were removed from further consideration.

5.2.5 Bubble Chamber Track Reconstruction

Images which remained after the hybridization of PIG tracks were passed to the bare bubble chamber (BBC) track reconstruction processor *MIT* (match intersecting tracks). Any comment which this author can make regarding the ontogeny of this software over a time period spanning most off his life would be of small value to the reader and a disservice to its creators. We can only point to the extensive literature regarding this topic.[7]

The BBC code handled a multitude of topological features aside from the matching and fitting of ordinary tracks. For example the range of stopping tracks was used in the determination of their momenta. All decay vertices were fit as were the momenta of their daughter particles. For tracks below

[7] E. S. Hafen, *GEOMAT* Part I. APC Programming Note DAS 75-1, Feb., 1975. This document provides a detailed discussion of the immediate progenitor to the *GEOHYB* bubble chamber code. A great deal of *GEOMAT* was taken over directly into *GEOHYB*. The references cited in this note are also of value as they both frame the historical position of *GEOMAT* and describe those elements of the algorithm not specifically covered in the write-up.

5 GeV/c a series of mass dependent fits were performed to take into account the $\beta\gamma$ dependence of the energy loss due to ionization.

5.2.6 Bubble Chamber Track Hybridization

BBC has matched and fit the images which remained after PIG track hybridization. Limitations on momentum resolution imposed by the chamber diameter and magnetic field behoove the experimenter to seek further track elements in the wire chamber. Over the radius of the bubble chamber a 5 GeV/c track had a sagitta of two millimeters or roughly five bubble diameters. The momentum measurement could be improved by locating related wire hits. The benefit derives from a doubling of the $\int B \cdot dl$ and a much longer lever arm over which to measure the magnetic deflection.

SOW[8] located candidate hits by swimming the BBC tracks into the downstream system. A total of four swims were carried out at $(1/p,\Lambda,\phi)$, $((1/p)+\sigma_{1/p},\Lambda,\phi)$, $(1/p,\Lambda+\sigma_{\Lambda},\phi)$, and $(1/p,\Lambda,\phi+\sigma\phi)$ where σ_i is the BBC error estimate for the parameter i. In this way a volume was described in the wire chambers in which one could look for consistent hits. Available hits were picked up and fit along with the bubble chamber prediction to a line in space. As in PIG hits were added and possibly dropped according to their contribution to the overall χ^2. When a suitable set of hits was isolated a distinct hybrid fit was performed which incorporated the bubble chamber vertex, the bubble chamber track fit, and the downstream line fit from above.

5.2.7 Summary

This brief summary of the reconstruction process serves to place each component of the algorithm into perspective as well as to point out the interrelationships among them.

We have seen that a reasonably accurate vertex estimate was the first step. Then the fastest tracks were reconstructed. The wire chamber tracks were isolated. These tracks were then used to locate their associated bubble chamber images and the process of hybridization was then completed. Next the remaining bubble chamber tracks were reconstructed. Finally tracks of intermediate momenta and angles were then hybridized by using the bubble chamber tracks to locate their associated wire hits.

At this point a highly refined vertex estimate was made using all available track information. Significant shifts in the vertex parameters triggered either a full track reconstruction pass of a reexamination of the track matching.

In so far as the overall pattern recognition problem is concerned we have seen that the detectors were used in a fashion that allowed the strengths of each to balance the weaknesses of the others.

---

[8] This routine is crudely documented in R. J. Plano, "*GEOHYP*: Technical Description," RIHSC 82-15A, Rutgers Univ., Dec. 1982.

In order to see first hand the performance of *GEOHYB* the EHS graphics package was converted for use by E570.[9] The resulting program *TEKSCAN* was used to visualize in space the raw wire chamber data, the CRISIS planes, the downstream track fits, and the reconstructed particle trajectories. Thus the effectiveness of the reconstruction software could be checked against this physicist's expectations. The final modifications to *GEOHYB* were based on a double *scan* of an entire roll of events.

We show in figure 5.3 an elevation and plan view of a reconstructed event as displayed by *TEKSCAN*. Note that this is the same sixteen prong event for which the CRISIS time data was displayed in figure 5.1. With the tracks fully reconstructed we see the relationship of the raw planes to the actual tracks in space. This event had seven tracks reconstructed by PIG, five by SOW, and the remaining four by BBC.

5.3 RECONSTRUCTION PROCESSING

The present data sample is composed of 68 non-contiguous rolls of film. The scan revealed 36,296 interactions within the full fiducial volume in the roughly 204,000 frames of film. The scan rules (§4.2.1) precluded the measurement of the majority (25,856) of these interactions. Table 5.1 summarizes the various scanning and measuring rejects.

TABLE 5.1
SCAN AND MEASURE REJECTS

events	reason for rejection
8456	too many incident tracks
5723	deferred
5166	beams too close
3003	PEPR (frame)
2330	bad beam identification
503	view missing
344	> 2 events in frame
246	interaction too close
85	PEPR (event)

A great many of the interactions were lost due to the confusion caused by the spray of particles emanating from interactions in a small, heavy liquid bubble chamber which was located directly upstream

[9] The author thanks Dr. Caroline Milstene for her preliminary efforts on this project.

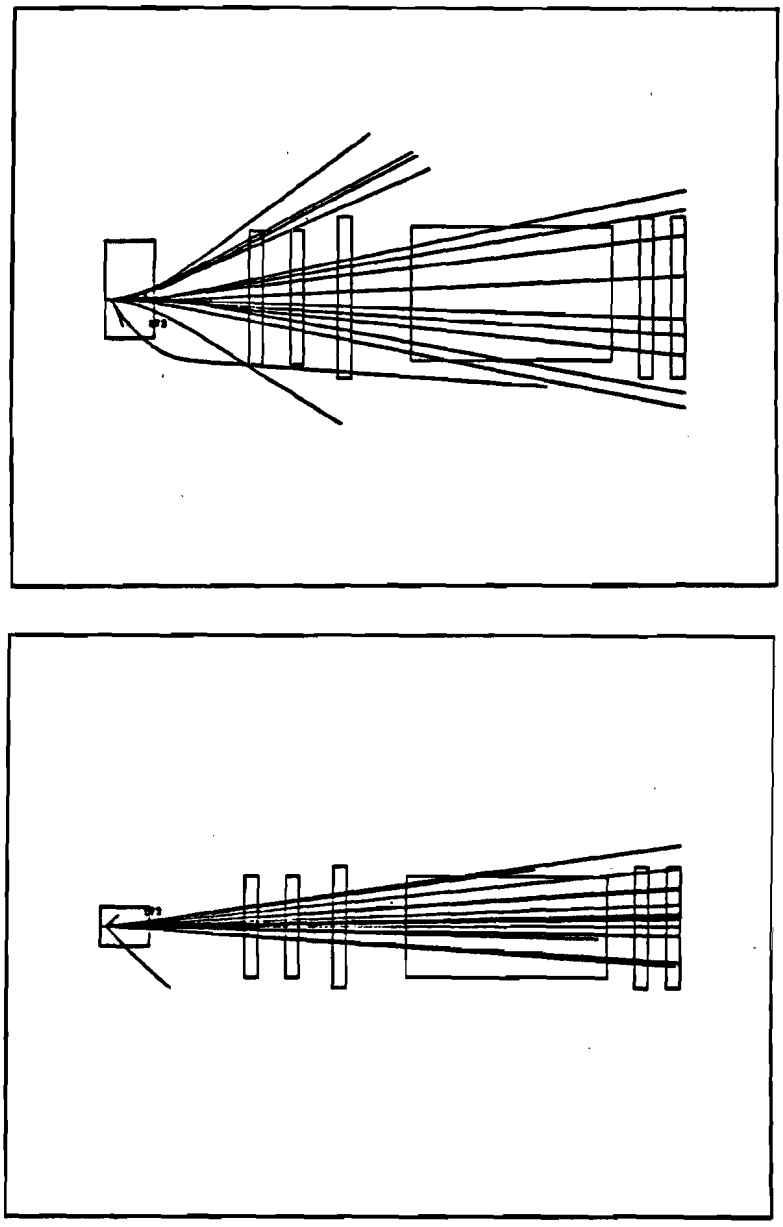

Figure 5.3 A reconstructed 16 prong event displayed in space. The upper plot is a view of the spectrometer from the east, while the lower plot is a view from above. (Note the the bubble chamber is improperly displayed in the upper plot. It should of course appear as a circle from this vantage point.)

of the 30" for a part of the run. The "deferred" events are those π and p induced events which occurred in the downstream fiducial volume. Thus this sample will yet produce an additional 5,723 events. We observe close beam tracks were a frequent occurrence and that the losses due to bad Čerenkov identification were consistent with the know counter performance.

Of the 10,438 events 2,669 were removed from the sample for the software, hardware, and Physics

reasons listed in table 5.2. Although 1,309 events produced in the nuclear targets were reconstructed they will not be considered at this time. The large number of events without time slots are due in part to events produced in or upstream of the plates. Because these event vertices are often obscured it is difficult to obtain a good vertex estimate.[10] Also several of the rolls were scanned without the use of *TRIFID*. The (wasteful) measurement of events without time slots serves to demonstrate one of the major reasons for the implementation of this program.

TABLE 5.2
SOFTWARE REJECTS

events	reason for rejection
1309	plate event
667	no time slot
313	bad beam identification
130	error unpacking D/S
119	poor fiducial measurement
32	time limit exceeded
28	arithmetic exception
20	no U/S data
17	space limit exceeded
12	PFC read error
11	bad U/S track fit
8	too many multiples
2	vertex fit failure
1	*FQXIN* read error

The remaining 7,769 reconstructed hydrogen events comprise the basis for the Physics analysis to follow. These events were distributed by beam type and charged topology (at the primary vertex) as shown in table 5.3. As the net charge of the initial state was +2 we expect only even topologies to be found. There were, however, 143 accepted events which were scanned with odd topologies. Hereafter these events will be considered to originate from the next higher topology under the supposition that a remaining track was too short to see or obscured by the other tracks. Also shown in table 5.3 is the fraction of events successfully reconstructed by the geometry program listed by topology. Note that this

[10] This problem has been address by R. DiMarco, Ph.D. thesis, Rutgers University, in preparation.

TABLE 5.3					
TOPOLOGICAL EVENT SUMMARY					
N_{ch}	π^+	K^+	p	sum	pass rate
2	918	279	1280	2477	0.999
4	357	220	453	1030	.997
6	376	290	451	1117	.994
8	428	305	416	1149	.988
10	335	234	364	933	.989
12	178	127	210	515	.991
14	127	63	115	305	.981
16	51	44	64	159	.961
18	25	10	17	52	.912
20	4	8	11	23	.950
22	4	–	2	6	.792
24	1	1	1	3	.909
sum	2804	1581	3384	7769	.991

pass rate considers only reconstructed events plus those which failed for reasons directly associated with the reconstruction algorithm. The overall pass rate is considerably lower.

The effective performance of PIG is crucial to the identification of secondaries. A total of 15,041 PIG tracks were successfully hybridized during event processing. For events of charged topology four or greater we find that the apparatus plus software located 2.5 ± 1.5 PIG tracks per event. On average these tracks had 8.4 ± 2.3 wire chamber hits. The number of PIG tracks per event is broken down into percentages in table 5.4.

TABLE 5.4									
PIG TRACKS PER EVENT†									
N_{PIG}	0	1	2	3	4	5	6	7	8
%-age	9.1	20.6	24.4	22.5	12.8	7.1	2.1	1.1	0.1

†excluding two prongs

SOW located 9,731 tracks with an average of 4.8 ± 2.4 wire hits. Finally 23,338 tracks were reconstructed by BBC.

Chapter 6

EVENT SIMULATION

The complexity of contemporary detector systems of itself forces upon the experimenter the burden of developing software to rival, and better still exceed, the intricacies of the hardware.

Programs written for high energy physics fall into five basic categories:

- **Design** of instrumentation
- **Modeling and Simulation** of physical processes
- **Calibration** of detectors
- **Reconstruction** of events
- **Analysis** of DST level data

Thus far this thesis has examined major programs used by E570 in three of the areas listed above. Design programs are often used to achieve a numerical solution to closed form problems. The calculation of electrostatic potentials described in Appendix A is a straight forward example of such a program. Chapter IV explored the various calibration programs. Due to the typically vast amounts of data to be characterized (often in new ways) it is this area which goes beyond mere statistics and places the physicist at the heart of *data analysis*.[1] Chapter V concerned itself with the reconstruction programming, while

---

[1] In the sense of J. W. Tukey. "The Future of Data Analysis". Ann. Math. Stat. 33 (1962) 1.

Chapter VII will address the final analysis programs. In order to maintain an overall sense of continuity the simulation programs will be introduced at this time. One must realize, however, that simulation finds its way into all of the areas of programming. The division of discussion by program type is admittedly artificial from the point of view of the Physics. The fact that it is necessary only serves to point out the trend toward removing the scientist from the Science at hand.

The importance of Monte Carlo programming can not be overly stressed. In the early stages of an experiment simulation spills over into the design of detectors which are capable of achieving the experimental goals. Because of the complexity of each of the calibration and reconstruction areas one must have the capacity to test software results with known input data. This activity goes beyond that of high level debugging. Using representative data one is able to study and compare statistical procedures in a timely and easy to understand fashion. Finally in analysis work the Monte Carlos are called upon to study the effects of detector resolution and acceptance on specific models of physical reality thereby forming a meeting place with theory.

6.1 EVENT GENERATION

Event simulation is a two step process. First one must produce an event in terms of the four-momenta of a collection of particles in the initial and final states. With this information in hand one then proceeds to track these particles through space and time all the while simulating the response they would cause in the detector. This conceptual separation of function has been carried over into the development of distinct programs for use by E570. The next section discusses the physical model, with the following section describing the simulation process. The end of the chapter presents results of tests of the reconstruction software and studies of acceptance.

6.1.1 Model for Soft Hadronization

Because one of the expectations of event simulation is the evaluation of experimental bias it is necessary that the spectrum of generated events closely resemble those that the detector will record in actuality. General techniques for event generation were developed in the last decade. In response to the observation of limited transverse momentum in multiparticle production these methods focused on the generation of events in phase space.[2] The isolation of the longitudinal and transverse components allowed gross features of the data to be represented.

Apart from these largely computational studies several theoretical models of particle dynamics emerged during the same years. Although originally intended as results in themselves some of these concepts were rapidly transformed into algorithms for event simulation.

---

[2] J.H. Friedman. "Random Event Generation with Preferred Frequency Distributions". J. Comp. Phys. 7 (1971) 201. D.C. Carey and D. Drijard. "Monte Carlo Phase Space with Limited Transverse Momentum". J. Comp. Phys. 28 (1978) 327.

of quarks. Hence, it is the simple function of *GENEV* to specify the initial state of the quarks in an interaction and then ask *JETSET* to perform the fragmentation. This having been done two files were created. The first file was simply a copy of the LUND COMMON blocks. These data were retained as they represented a complete and easily accessed description of the event. The second file contained a description of the event in terms of track parameters and topological features. This was used by the simulator programs to create the induced detector response for each event.

6.2 DETECTOR SIMULATION

The foundation of the simulation package was layed by members of the EHS collaboration. Two of the many EHS programs were the most applicable to the FHS configuration of detectors, namely *SIMEV* and *SIMOUT(2)*. Although major rewriting was required[7] to suite the needs of E570 the original names have been retained as a testament to the original authors.

6.2.1 Bubble Chamber Data

The purpose of the program *SIMEV* is to provide HYDRA banks at a level equivalent to the output structure of *PRECIS* (§5.1). That is to say as though real track images had been recorded on film, scanned, measured, and processed as described previously.

In order to accomplish this each event from *GENEV* was read in and underwent the following sequence of operations. First a vertex was generated randomly in the fiducial volume of the bubble chamber. Then a set of incident track angles was generated at the vertex in a fashion representative of the beam dispersion. At this time a beam track was generated in the upstream system and wire chamber data was recorded. A fit was then done to the wire hits to provide a track fit for the beam as is done in *PRECIS*. Each of the charged tracks was then traced through the bubble chamber magnetic field. For each view a set of points on the track in space were chosen and projected through the optics and onto the film plane. These points were recorded as representative of those which would have been found by the automatic measuring machines. As such the points were dispersed about their true values and were chosen so that their separation and number corresponded to those normally achieved with the MIT PEPR. Since the measuring machine can not record the vertex this point was simulated with an accuracy representative of a scanner using an IPD machine. Tracks were stopped if they crossed into a dense medium such as the bubble chamber windows or magnet iron. Features of the event such as stopping protons and charged and neutral decays were placed into the banks. Each track was traced until it was stopped, decayed or exited the bubble chamber. Decay products were retained internally if their decay vertex was anywhere within the entire spectrometer.

In addition to the required banks *SIMEV* also produced banks which contained information on the

[7] By Dr. Dave Brick of Brown University and this author.

original track parameters.

6.2.2 Electronic Data

The program *SIMOUT* was designed to pick up the tracing of particle trajectories as they entered the downstream system. Tracks were continued until they left the spectrometer in either transverse plane or they passed the last drift chamber. Wire hits were produced at each wire chamber plane which was crossed. In CRISIS both time and charge data were produced. The charge Monte Carlo used the model for ionization described in Appendix C.

After generating hits for all the tracks in an event the data was *cleaned* in order to impose limitations characteristic of the detectors. Overlapping hits were eliminated in the DCs, adjacent hits were associated into bunches in the PWCs, and so on.

6.3 RECONSTRUCTION STUDIES

A total of 5000 Monte Carlo events were processed through the *GENEV* · *SIMEV* · *SIMOUT* · *GEOHYB* chain of programs. These events were divided evenly among π^+, K^+, and p beams. During processing events were invariably lost due to ill conditioned data and certain limitations of the reconstruction algorithm. Table 6.1 details the various reasons for event loss. Those events which failed during the simulation phase were due to an unbiased test in *SIMEV* and so they have been removed from further consideration. A single hard failure (tape read error) has also been dropped.

TABLE 6.1
SUMMARY OF EVENT LOSSES

events	reason for loss
47	simulator failure
49	mathematical exception†
45	time limit exceeded†
14	"space" limit exceeded†
1	hardware failure

†during *GEOHYB* step

GEOHYB failed to reconstruct 108 events or 2% of the total. Roughly half of these were due to run time exceptions or traps such as divide by zero or square root of a negative argument. The remaining losses were due to processing limitations.

Of the 4844 reconstructed events 86% were complete and charge balanced at the primary vertex. That is to say *GEOHYB* reconstructed the correct number of secondaries for the event and their total charge was that of the initial state. *GEOHYB* reconstructed 99% of all the generated secondaries. Less than 2% of all tracks were assigned the wrong charge, but since a single misassignment breaks charge balance for the entire event the fraction of unbalanced events is larger by a factor of the average multiplicity.

6.3.1 Vertex

In order to investigate the reliability of vertex estimates the difference between *simulated* and *reconstructed* coordinates were calculated for each event. We see in figure 6.1 the resulting distributions of vertex shifts for each of the x, y, and z coordinates. These results indicate that the vertex reconstruction algorithm has been rather successful at its task. We may understand this statement by a few simple considerations.

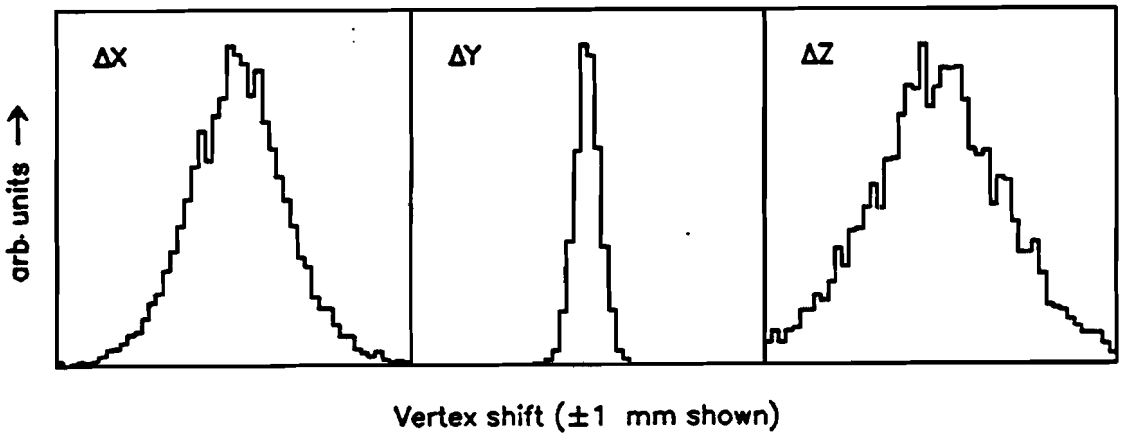

Figure 6.1 Distribution of vertex coordinate shifts between the simulated and reconstructed values.

The measuring machine has an inherent setting error of 1 μm on film. Due to the bubble diameter it was, however, only possible to locate a track to within 5 μm in a direction transverse to its path. The coordinates (x_V, y_V, z_V) are the result of fitting the intersection point of several trajectories in space. As the tracks are for the most part traveling at small angles with respect to the x-axis we expect the y estimate to be dominated by the measuring error times a statistical factor. As the cameras had a demagnification of roughly twenty a distance of 5 μm on film corresponded to 100 μm in space. We see this compares well with the value achieve by *GEOHYB* for $\sigma_{\Delta y_V} = 70\,\mu$m. It is clear that the other transverse coordinate Δz_V does not have the same width. This is due to the effects of reconstructing sterioscopic light rays on the z coordinate. We expect z to be degraded relative to y by the ratio of

the object distance to the camera seperations, or a factor of 3.5. This is bourne out in the value of $\sigma_{\Delta z_V} = 380\,\mu$m. Finally the x coordinate is influenced by the sloping nature of the tracks. If two tracks meet at right angles a very precise vertex location can be found as is the case for most two prong events. But if the tracks diverge at a small angle the propagation of errors to the initial line of flight reduces the quality of the vertex location in that dimension. We see that $\sigma_{\Delta x_V} = 280\,\mu$m falls between the corresponding values for the y and z directions.

Note that the Monte Carlo data set contains no elastic or diffractive events. Also in terms of our expectations for real event data we mention that the simulated bubble chamber track segments contain no wild points. That is to say the effects of track overlap are not considered in the simulation. In reality close tracks are problematic both during event scanning and during the pattern recognition and track follower processing of the automatic measuring device. Such effects will naturally degrade the overall performance as regards track matching as well as vertex and momentum estimation.

6.3.2 Momentum

We now turn our attention to the reconstruction of momentum. Recall that this involves estimating the three parameters $(1/p, \Lambda, \phi)$ at the interaction vertex for each track. In the the following we will examine the resolution anticipated at the FHS and using *GEOHYB*, both being less than perfect devices.

Results will be presented on both parameter and interval estimates. The three reconstruction techniques BBC, PIG, and SOW will be examined seperately in order that we may more fully understand their individual properties.

Of the reconstructed tracks 98% utilized bubble chamber data from all three camera views. In the following analysis simulated and reconstructed tracks were correlated by requiring the reconstructed track to match a simulator track in at least two views. This test provided simulated/reconstructed track pairs in 87% of all cases.

We will consider in the following the shifts in the parameters between their simulated and reconstructed values. That is, for example, in the case of the dip angle

$$\Delta\Lambda = \Lambda^S - \Lambda^R.$$

Where the superscripts S and R refer respectively to simulated and reconstructed quantities. Of secondary importance to the goals of this thesis we also examine the various *pull* distributions, being for example

$$\frac{\Lambda^S - \Lambda^R}{\sigma_\Lambda^R}.$$

Here σ_Λ^R is the error assigned by the track fit to the parameter Λ. We note that a pull distribution which is not a unit normal is indicative of residuals which are not normally distributed or an incorrect error

analysis.

The distribution of shifts in the various parameters are seen in figure 6.2, while the related pull distributions are seen in figures 6.3. The standard deviation of each distribution has been determined by fitting gaussians to the data. The results of these fits are presented in tables 6.2 and 6.3. We note that the sample contained 15477 BBC, 16494 PIG, and 4066 SOW tracks.

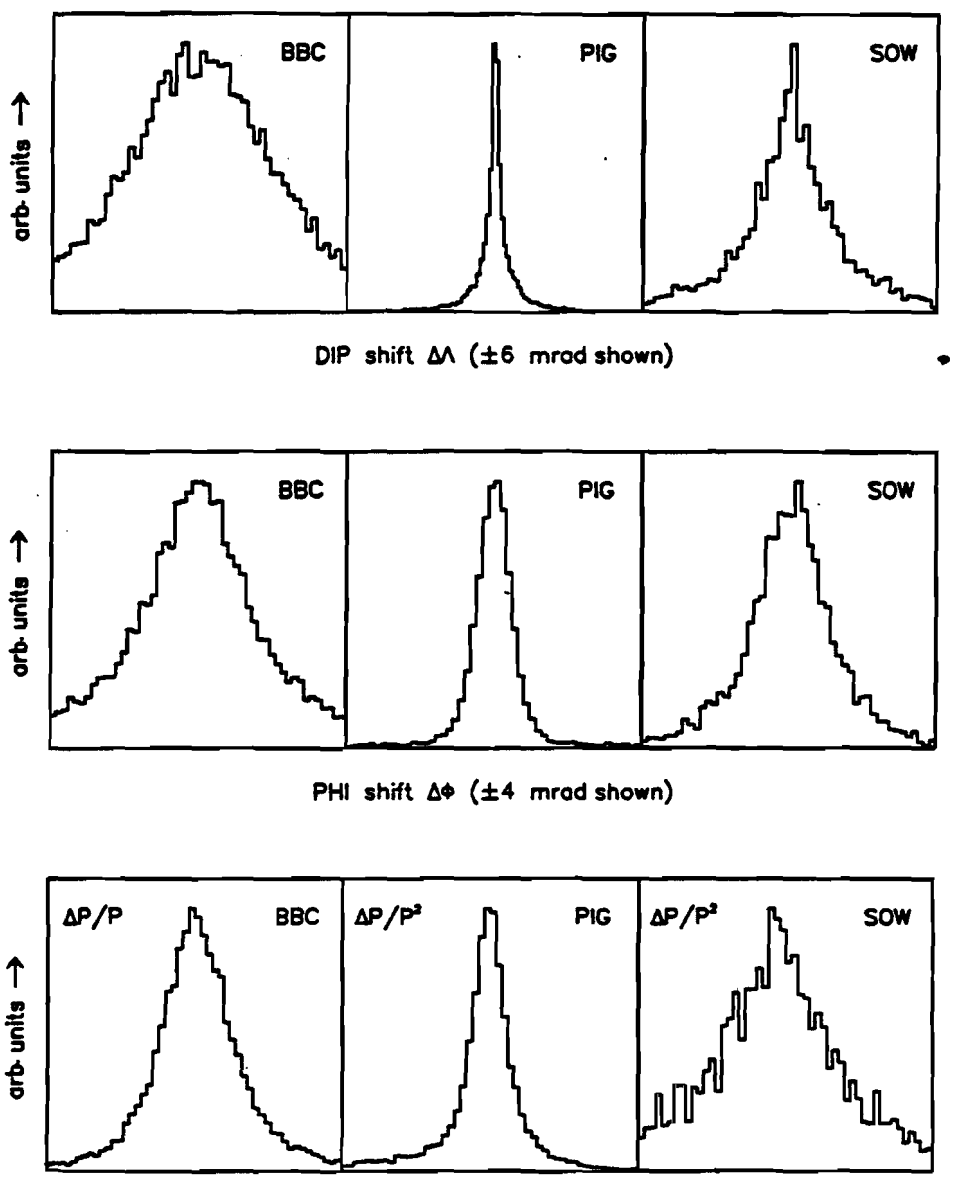

Figure 6.2 Distribution in the shifts of Λ, Φ, and $1/p$.

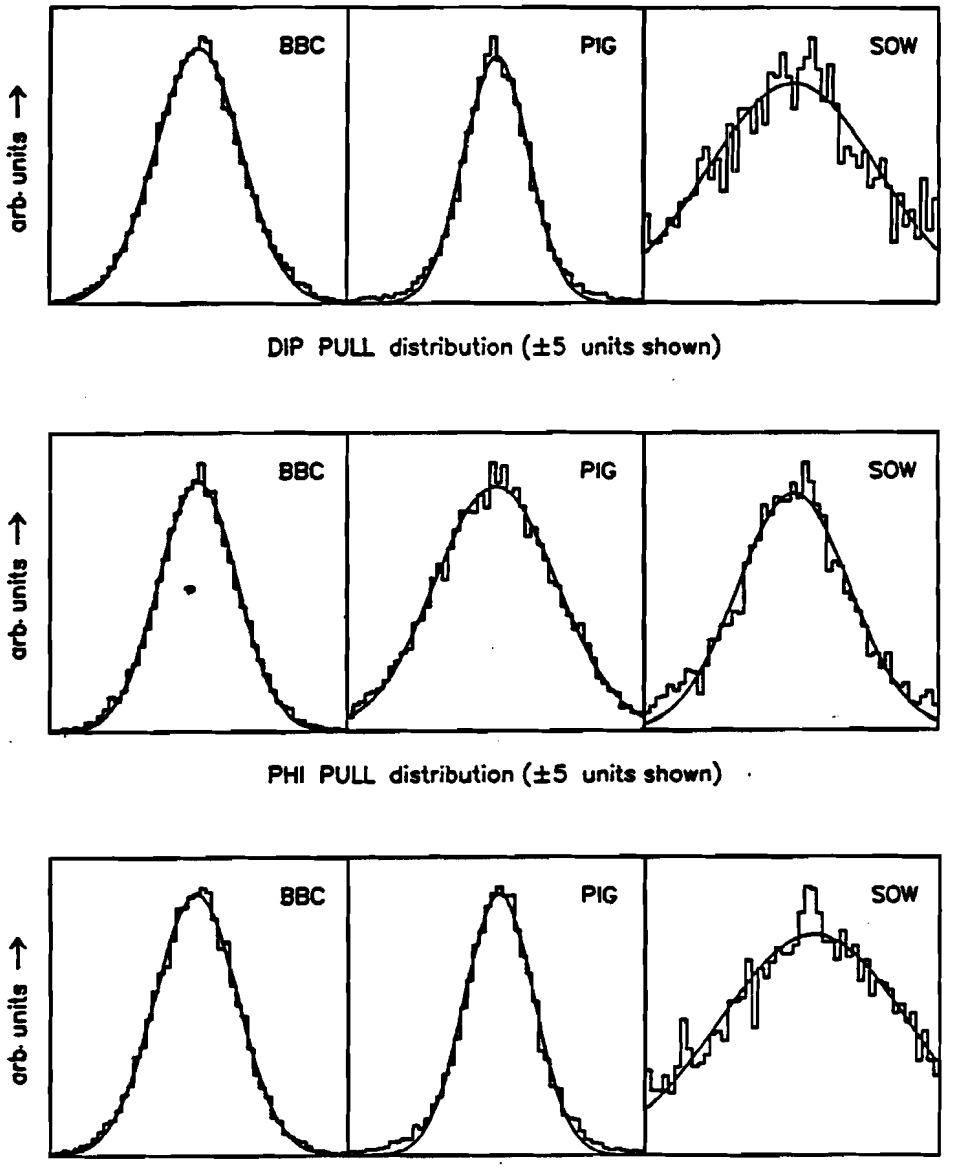

Figure 6.3 Pull distributions.

The results are consistent with the relative expectations of each reconstruction technique.

6.3.3 Acceptance Studies

In order to eliminate reconstruction bias in the final data analysis we will presently examine the reconstruction efficiency in terms of relevant kinematic variables. In particular figure 6.4 shows the ratio of the number of particles reconstructed in a particular Feynman X bin to the number simulated in that

TABLE 6.2			
RMS SHIFT			
	BBC	PIG	SOW
$\sigma_{\Delta\Lambda}$	3.0 mr	0.3 mr	1.5 mr
$\sigma_{\Delta\phi}$	1.6 mr	0.5 mr	1.0 mr
$1/p$	$2.5 \cdot 10^{-2}$†	$1.3 \cdot 10^{-3}$‡	$4.1 \cdot 10^{-3}$‡

†$\sigma_{\Delta p/p}$

‡$\sigma_{\Delta p/p^2}$

TABLE 6.3			
RMS PULL			
	BBC	PIG	SOW
Λ	1.1	2.9	1.6
ϕ	2.0	1.9	2.5
$1/p$	1.4	1.2	3.2

bin. We observe the the efficiency is essentially flat over the entire range of x_f. As the x_f distribution is inherently exponential any variations here are in any event reduced to logarithmic corrections to the exponential slope.

Having established the x_f dependence of the reconstruction efficiency we will now examine the composition of the events by reconstruction technique. The simulator results are shown in figures 6.5. These plots show the bin by bin ratio of, for example, the number of tracks reconstructed by PIG to the total number reconstructed (BBC+PIG+SOW). We note that HYBRID refers to the sum PIG+SOW. One observes that the hybridization techniques provide a uniform response over nearly the entire range of x_f in the forward hemisphere. The acceptance of the spectrometer limits those tracks which pass through the dE/dx detector (PIG) only at the smallest x_f values. This inefficiency is more evident in the plots of the center of mass rapidity Y* (see figure 6.6). We observe that the ability to identify final state particles is relatively restricted over the first unit of rapidity. This plot becomes particularly revealing when we recall that Y^* is by nature uniformly distributed up to its kinematic limit. Thus figure 6.6 is a direct indication of the percentage-wise acceptance of the particle identifier. When SOW tracks are included we see that the spectrometer is effective in reconstructing track momenta over virtually the entire forward hemisphere.

The fact that the ultimate fraction of HYBRID tracks is in the range of 90–95% reflects a variety

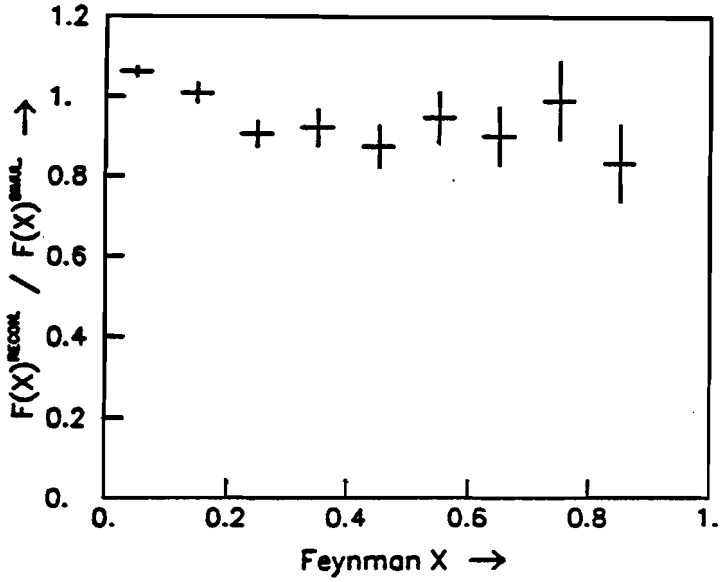

Figure 6.4 Efficiency of reconstruction in terms of the Feynman X variable.

of "experimental" limitations. For example two tracks may have been so close to each other that they could not be resolved in CRISIS, or for that matter in the bubble chamber. Alternatively the density or number of wire chamber hits may have exceeded the pattern recognition capabilities of PIG.

We may conclude from the above that the product of the DPI acceptance and the reconstruction efficiency of *GEOHYB* provide the opportunity for final state particle identification over a significant fraction of the forward hemisphere. The following section describes father limitations on particle identification imposed by the ionization sampling technique.

6.3.4 Ionization Loss Studies

Those simulated ionization samples which were associated with hybridized (PIG) tracks have been examined. Figure 6.7 shows the 70% truncated mean ionization of each track plotted against its lab momentum. Along with the data are plotted theoretical ionization curves for the pion, kaon, and proton. These curves represent the 70% truncated mean ionization loss predicted by the model described in Appendix C. They were evaluated by numerical integration of the energy loss distribution as is discussed more fully in conjunction with figure C.2. The simulator used a parameterization of Sternheimer's density effect correction[8] which differs by some 3% in the height of the relativistic rise with the newer values[9] used for the data analysis.

---

[8] R. M. Sternheimer, et. al., Phys. Rev. 3B (1971) 3681.

[9] R. M. Sternheimer, et. al., "The Density Effect for the Ionization Loss of Charged Particles in Various Substances,"

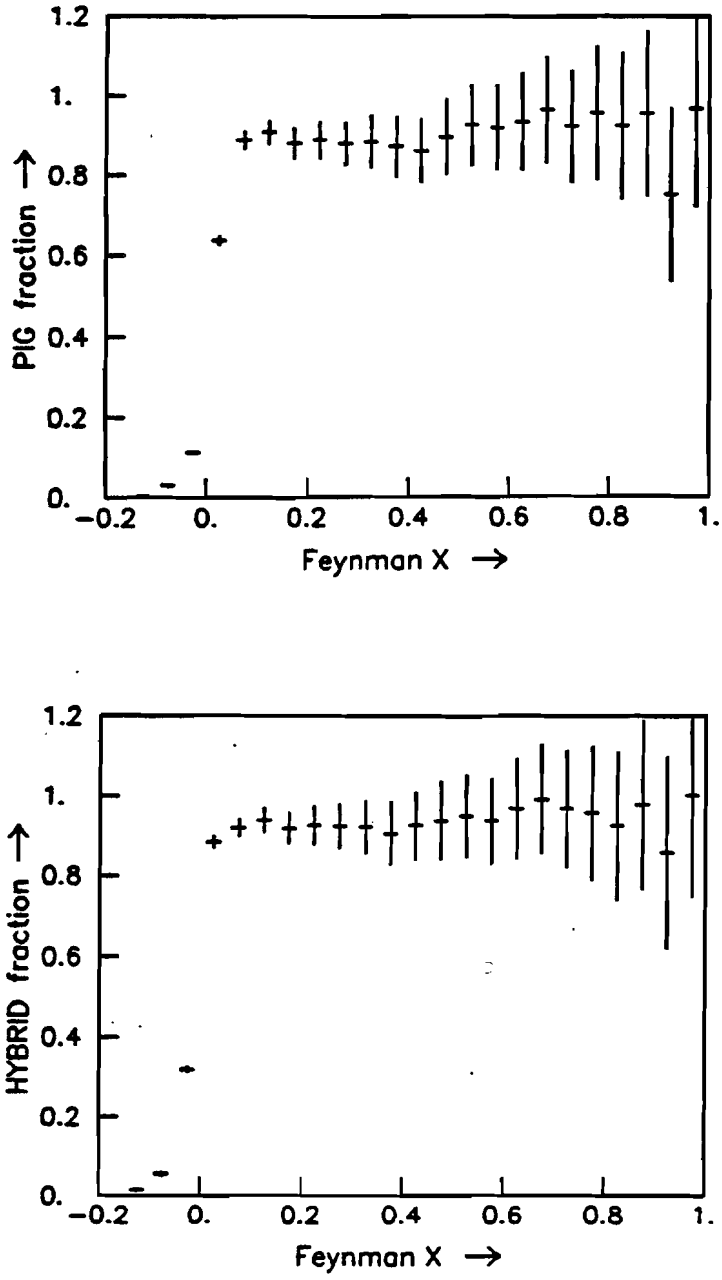

Figure 6.5 Fraction of all reconstructed tracks which were reconstructed using the PIG technique (upper) and the fraction of those which were HYBRID (lower). Both are plotted in terms of the Feynman scaling variable.

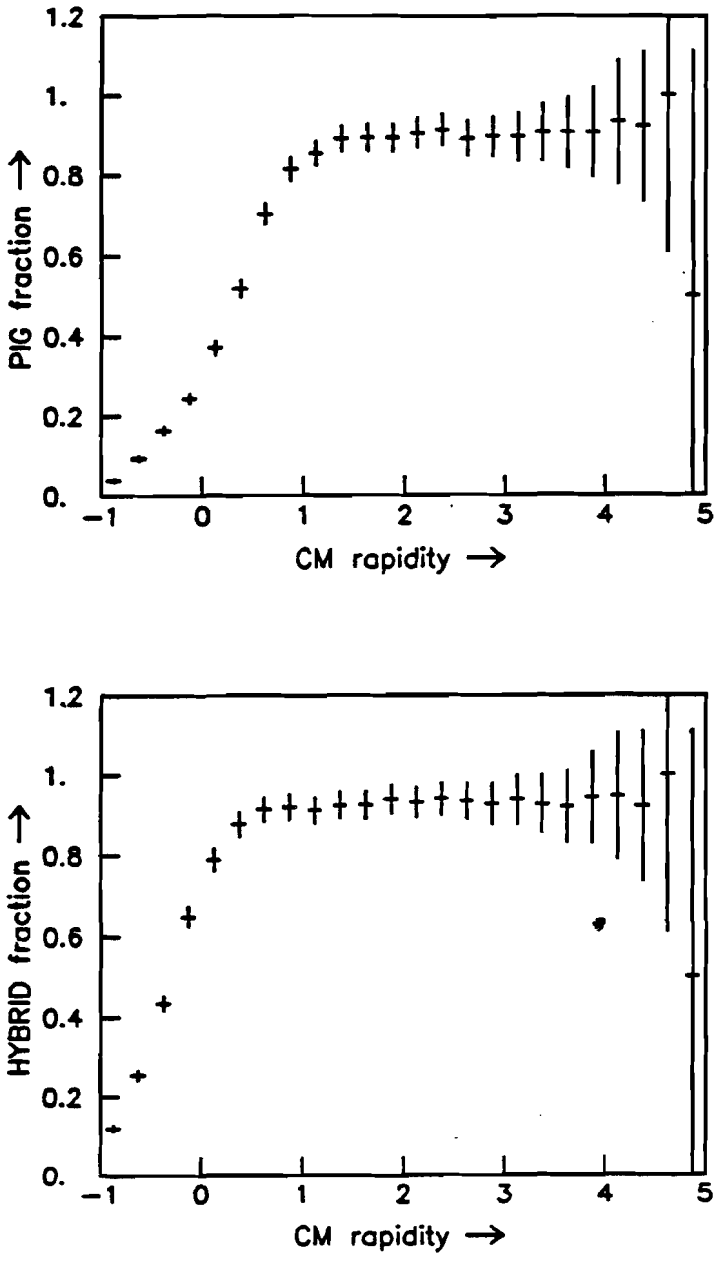

Figure 6.6 The PIG and HYBRID fractions (as in figure 6.5) in terms of the center of mass rapidity.

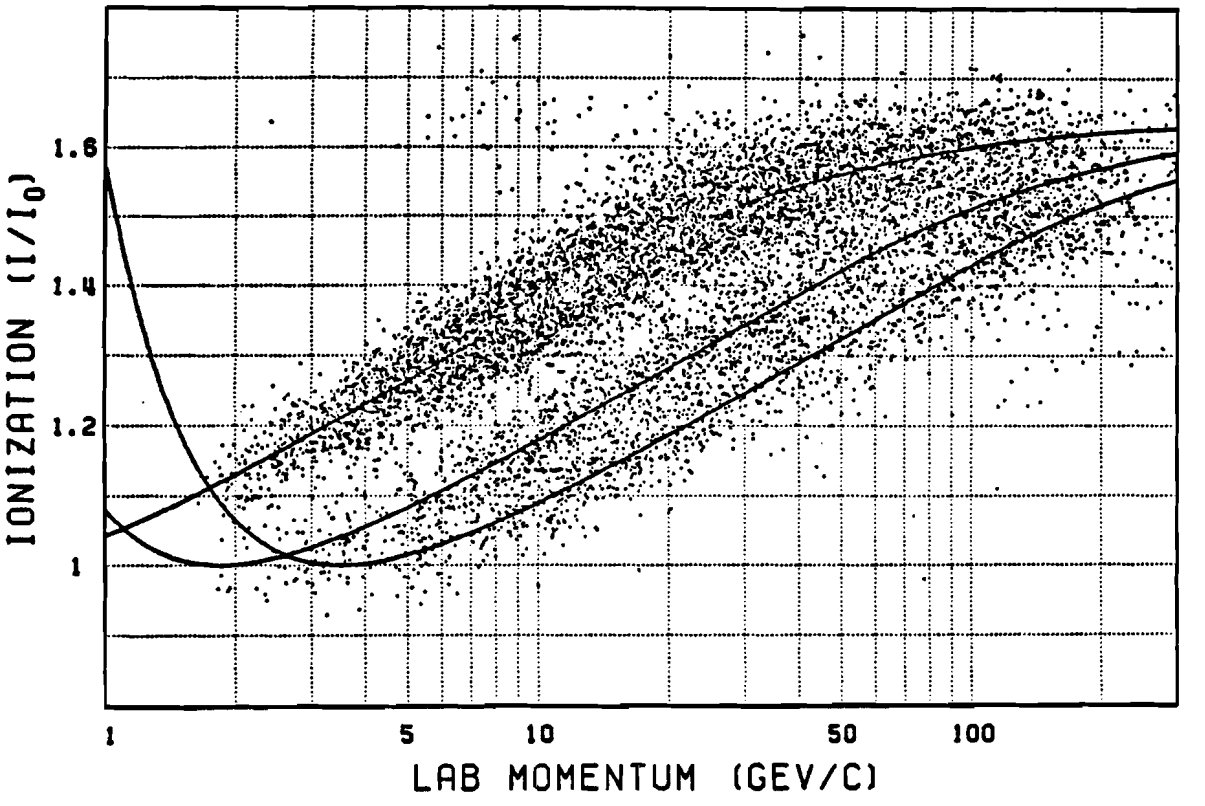

Figure 6.7 Truncated mean ionization versus lab momentum.

The plotted results show the case of essentially ideal performance of the dE/dx detector. We observe that the pions are cleanly separated from the kaons and protons in the region of 5–50 GeV/c. The small cluster of events located in the area of 1.5–1.6 I/I_0 and 5–10 GeV/c appear to be outliers. They are in fact not outliers but rather Dalitz electrons from the primary vertex, which at this momentum have ionization losses on the Fermi plateau.

Using this data we may predict the resolution which the E570 dE/dx detector can be expected to achieve. Figure 6.8 shows the distribution of the difference between the estimated ionization and the predicted value at the reconstructed momentum for those tracks which are know to be pions. This distribution has an RMS deviation of 0.058 units. It is typical to express this figure of merit as a percentage of the plateau value. Thus we expect an RMS of 3.8% or a FWHM of 8.4%. These numbers are most strongly dependent on the sample thickness, the number of samples, and the gas composition.

It is interesting to note at this time the spectra of secondary momenta in the laboratory system. This is relevant given the expected behavior of the ionization loss as a function of lab momentum. We see in figure 6.9 the distribution of all reconstructed secondaries as well as those reconstructed with

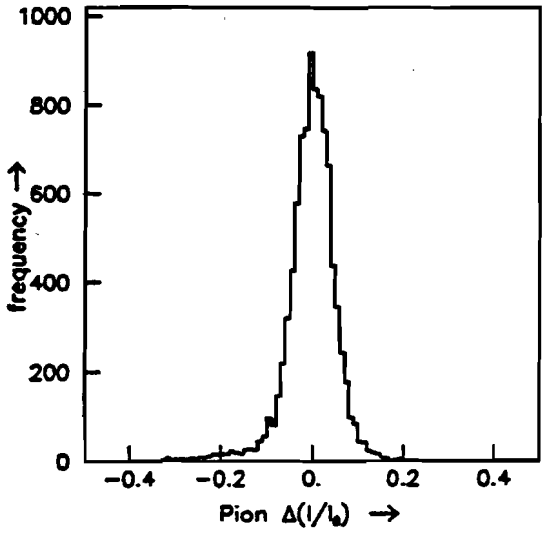

Figure 6.8 The reconstructed residual ionization for particles which were simulated as pions.

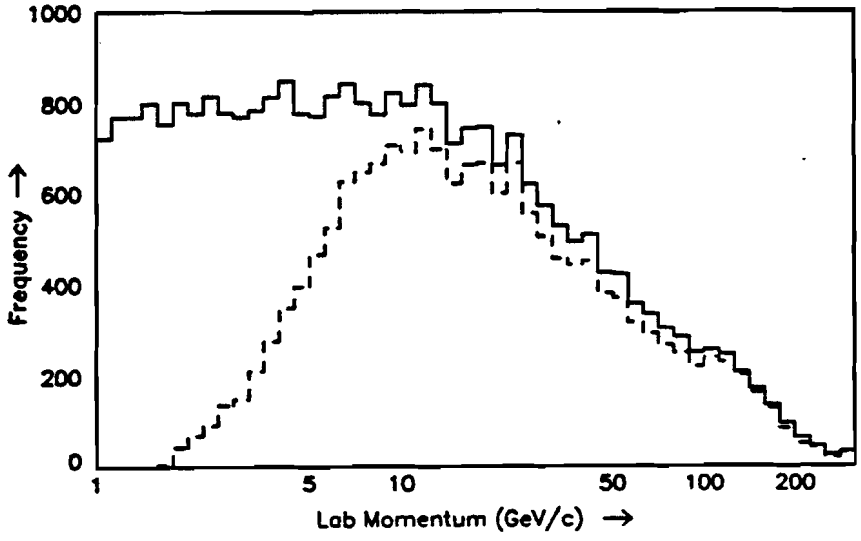

Figure 6.9 The distribution of particles plotted against the logarithm of the lab momentum. The solid histogram is for all reconstructed particles, while the dashed histogram if for PIG tracks only.

associated ionization information. This spectra underlies the data shown in figure 6.7

More detailed discussion of particle identification efficiency will be presented in the next chapter in association with the treatment of data.

Chapter 7

ANALYSIS

Thus far the process of data acquisition and event reconstruction have been described. In addition the spectrometer acceptance as well as the efficacy of the reconstruction software have been illustrated with the use of Monte Carlo techniques.

The purpose of this the final chapter is to present measured distributions. In preparation for this the algorithms developed for final state particle identification as well as the means of compensating for various inefficiencies will be described.

The data processing which is discussed in this chapter has taken place after event reconstruction. Aside from the *GEOHYB* output data structure, certain calibration and Monte Carlo data have been used in order to make the best possible Physics related decisions.

7.1 FINAL STATE PARTICLE IDENTIFICATION

E570 was instrumented to determine secondary particle masses by ionization loss in two lab momentum ranges. First the bubble chamber was capable of separating protons from pions below the momentum of 1.4 GeV/c. And second the DPI was designed to separate pions, kaons, and protons in the range of 5–50 GeV/c.

7.1.1 Bubble Chamber Ionization

The bubble chamber ionization routine used in this analysis descends from the subroutine *PWGION*.[1,2] This routine has been estimated to identify 90% of all non-stopping protons in the momentum range $0.2\,\mathrm{GeV/c} < p_{lab} < 1.4\,\mathrm{GeV/c}$, while only introducing a 5% contamination of pions. The algorithm was originally developed for use in E154. As both the 30" chamber and the MIT PEPR were used in this experiment we expect results of similar quality.

The PEPR device automatically measured the density of bubbles along the film plane images. In addition the density of a non-interacting *ionization reference track* was also measured. The ionization routine made corrections for geometrical (track dip angle) and measurement (angle of attack of the sweep element) effects. The track ionization was then divided by that of the reference track. By using the reference track as the nominal minimum in ionization for a given frame effects due to variations in the operation of the bubble chamber were eliminated.

In figure 7.1 we show the resulting distribution of ionization loss versus lab momentum for several rolls from run **A**. We observe that the separation between pion and proton is for the most part unambiguous over the selected momentum range.

A track was identified as a proton by either its being noted as stopping by the scanner or by its bubble chamber ionization. When a proton was found its kinematic properties were taken to be those determined for the proton hypothesis in the mass dependent fit. All other particles were considered to be pions.

Due to an error in the Rutgers PEPR software the number of measurements produced was not sufficient to make adequate mass assignments. As a result any further mention of particle identification in the backward hemisphere will refer to the MIT portion of the data sample exclusively.

7.1.2 Identification of Secondaries by Ionization Sampling

Particle identification in the forward hemisphere is to be accomplished using the ionization samples collected by the dE/dx detector. This section describes the treatment of charge samples which were associated with hybridized tracks. We will address calibration, the development of an estimator of ionization loss, and finally the techniques used in particle identification.

7.1.2.1 Calibration

After *GEOHYB* was run the calibration described in §4.6 was applied to the relevant charge samples. In particular the ADC, cell-to-cell, and temporal gain corrections were enforced. As the track slopes in both

[1] D. Ljung, "Selection of 0.2 GeV/c to 1.4 GeV/c Protons using PEPR Ionization Measurements," PHS Consortium Newsnote #31, Oct. 1974

[2] The author wishes to thank Theresa Fuess for her help in creating a revised version of this program for use in E570.

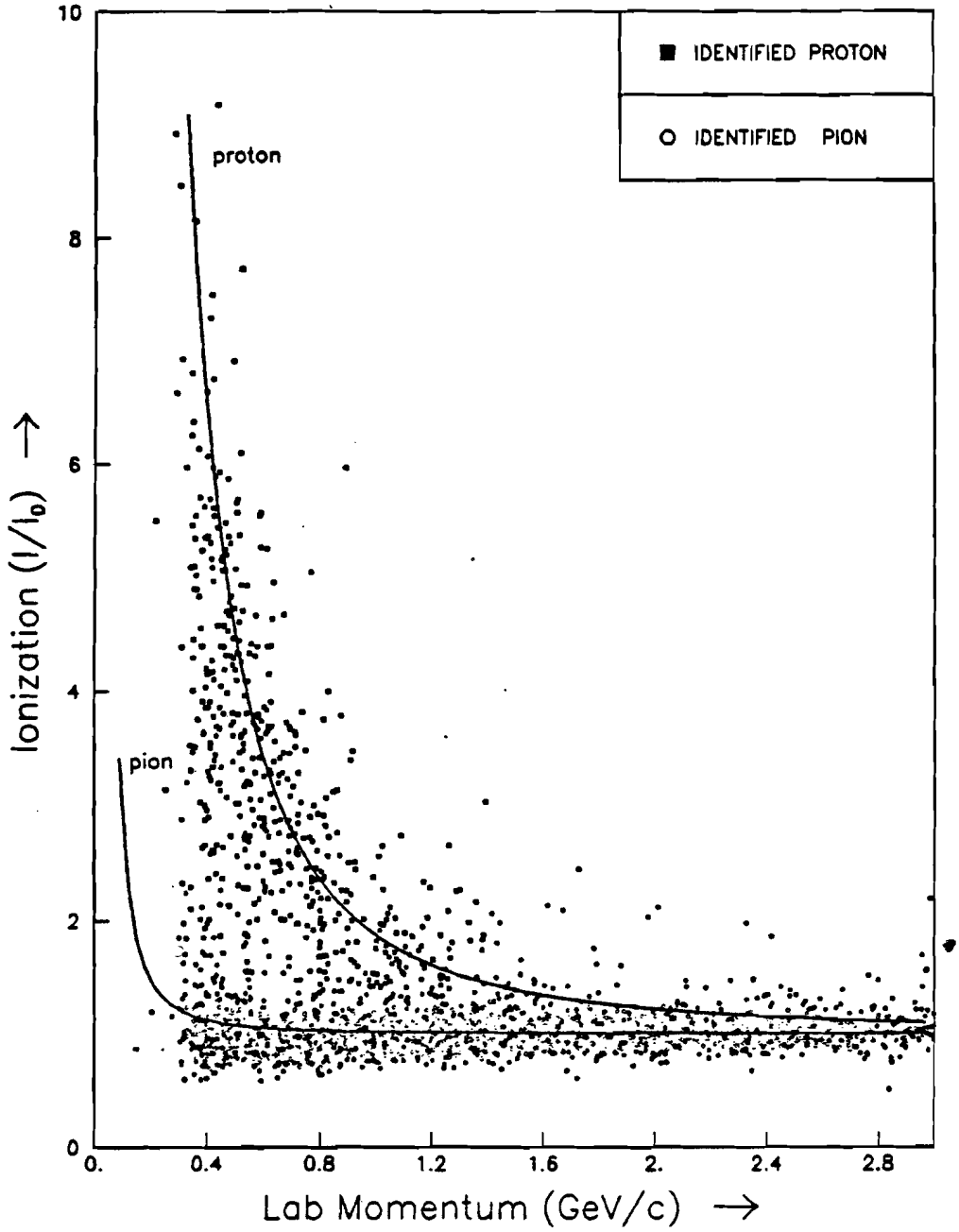

Figure 7.1 The corrected bubble chamber ionization measurements versus lab momentum. Plotted along with the data are curves showing the expected ionization for the pion and the proton.

the y and z directions were know at this time a simple *tilt* correction was made for the effective length of the cell due to track inclination. Overflow and underflow charges were removed from the sample.

7.1.2.2 Estimation of the ionization loss

Having smoothed the detector response we are now interested in choosing an estimator with which to evaluate the ionization loss for a given track. In chapters 4 and 6 we have already seen the use of the truncated mean to estimate the ionization. In the following we will use the maximum likelihood estimate of the ionization rather than the truncated mean. This choice has been made based on the fact that maximum likelihood is the most efficient estimator for parameters with normally distributed residuals.[3]

The form of the fitting function was determined using the energy loss distribution described in appendix C. Specifically the energy loss distribution $f(\Delta)$ was taken to be that of a 6.5 GeV/c pion in 1.6 cm samples of an 80/20 mixture of Ar/CO_2 at NTP. The legitimacy of assuming that the shape of $f(\Delta)$ is independent of momentum has been investigated by Allison and Wright.[4] They have found that this introduces a relatively small error provided the sample size is greater than 1 cm-atm of Argon.

The goal of the maximum likelihood analysis was to estimate a scale parameter ϵ which relates the energy loss Δ to measured charges Q_i via $Q = \epsilon\Delta$. We may write the likelihood

$$L(\epsilon) = \prod_{i=1}^{n} f(Q_i/\epsilon)$$

for a track with n samples. By varying ϵ we seek to maximize L. In practice we have exploited the parabolic nature of $\ln L(\epsilon)$ in order to shorten the time required to find the best value $\tilde{\epsilon}$. The analysis proceeded as follows. $\ln L(\epsilon)$ was evaluated at 15 points on a plausible range of ϵ. These points were then fit to a quadratic and the maximum was located at ϵ_1. $\ln L(\epsilon)$ was then evaluated at a new set of 15 points. This time, however, the range was reduced by a factor of five over the previous pass and centered at ϵ_1. These points were then fit to a quadratic giving the final estimate $\tilde{\epsilon}$ at the maximum of the fit to $\ln L(\epsilon)$.

In figure 7.2 we see the values of $\ln L(\epsilon)$ evaluated on both ranges for a typical track. Here we see the validity of the quadratic fit. We show in figure 7.3 the best fit to several tracks. Note that the data has been rebinned so that the peak bin contains a statistically significant number of entries. The maximum likelihood estimate is of course independent of the binning. We observe the close match between the best fit distribution and the track data.

---

[3] W. T. Eide, et. al., "Statistical Methods in Experimental Physics," (Amsterdam: North-Holland Publishing Co., 1971), §8.3.

[4] W. W. M. Allison and P. R. S. Wright, "The Physics of Charged Particle Identification: dE/dx, Čerenkov and Transition Radiation," Oxford University preprint 35/83.

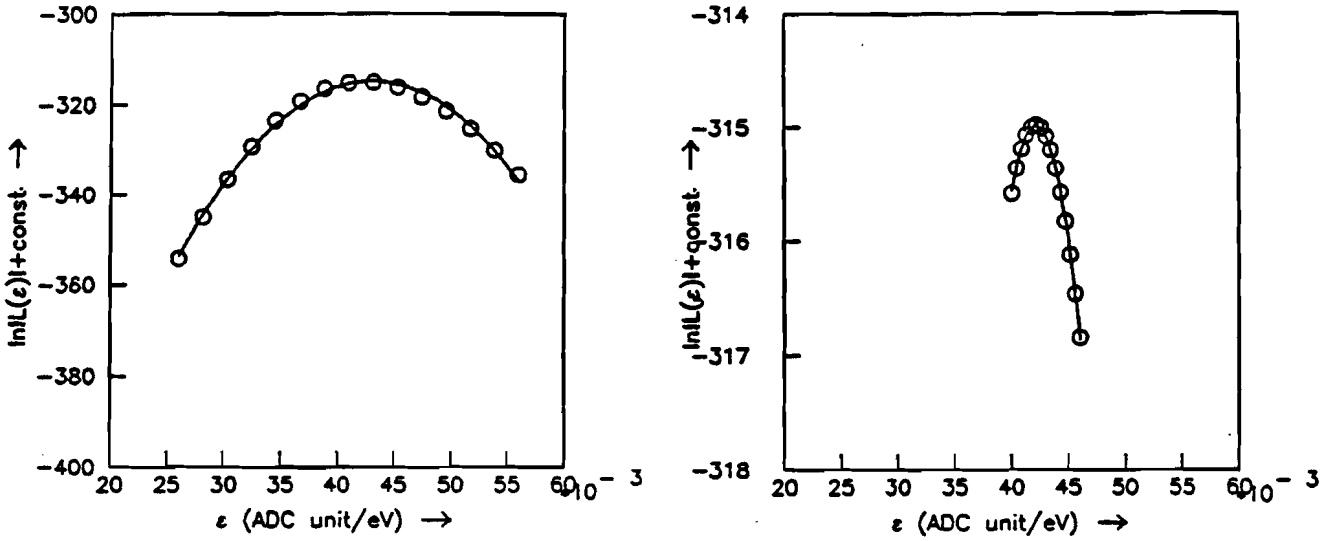

Figure 7.2 At left is shown $\ln L(\epsilon)$ evaluated on the full domain of ϵ. This course estimate allows us to zero in on the maximum as is shown on the right. Note the change in the vertical scale.

7.1.2.3 Normalization

Having fit the scale parameter for each of the tracks in our sample it remains to determine the overall normalization of this measure of the ionization to the expected ionization loss curves. This may be accomplished best by using the secondaries produced by pion beams as this sample will consist for the most part of pions. We may further enhance the pion signal by requiring the secondary track momenta to fall in the range $5\,\mathrm{GeV/c} \leq p_{lab} \leq 50\,\mathrm{GeV/c}$ as it is in this range that we expect the least overlap between π and K/p. Finally we require that the tracks each have more than 100 charge samples.

Within these boundaries we have plotted the ratio of the expected ionization for a pion at a given reconstructed momenta to the fit value of ϵ for that track. The result is seen in figure 7.4. In order to determine the proportionality constant accurately this distribution has been fit to a gaussian on the domain (25,35). This was done in order to suppress the effects of kaons and protons in the sample. Their presence is clearly evident in the high end tail of the distribution. The mean value determined by the gaussian fit has been used to relate the maximum likelihood fit ϵ values to relative ionization losses I/I_0.

Using the same data and cuts we have determined the RMS deviation of the measured charge from its expected value. This distribution is also seen in figure 7.4. Again pions have been selected by fitting a gaussian on a restricted domain $(-0.09,+0.21)$. This yields $\sigma_{I/I_0} = 0.095$ as opposed to 0.058 determined by the simulator (§6.3.4). The achieved resolution is therefore 64% larger than expected.

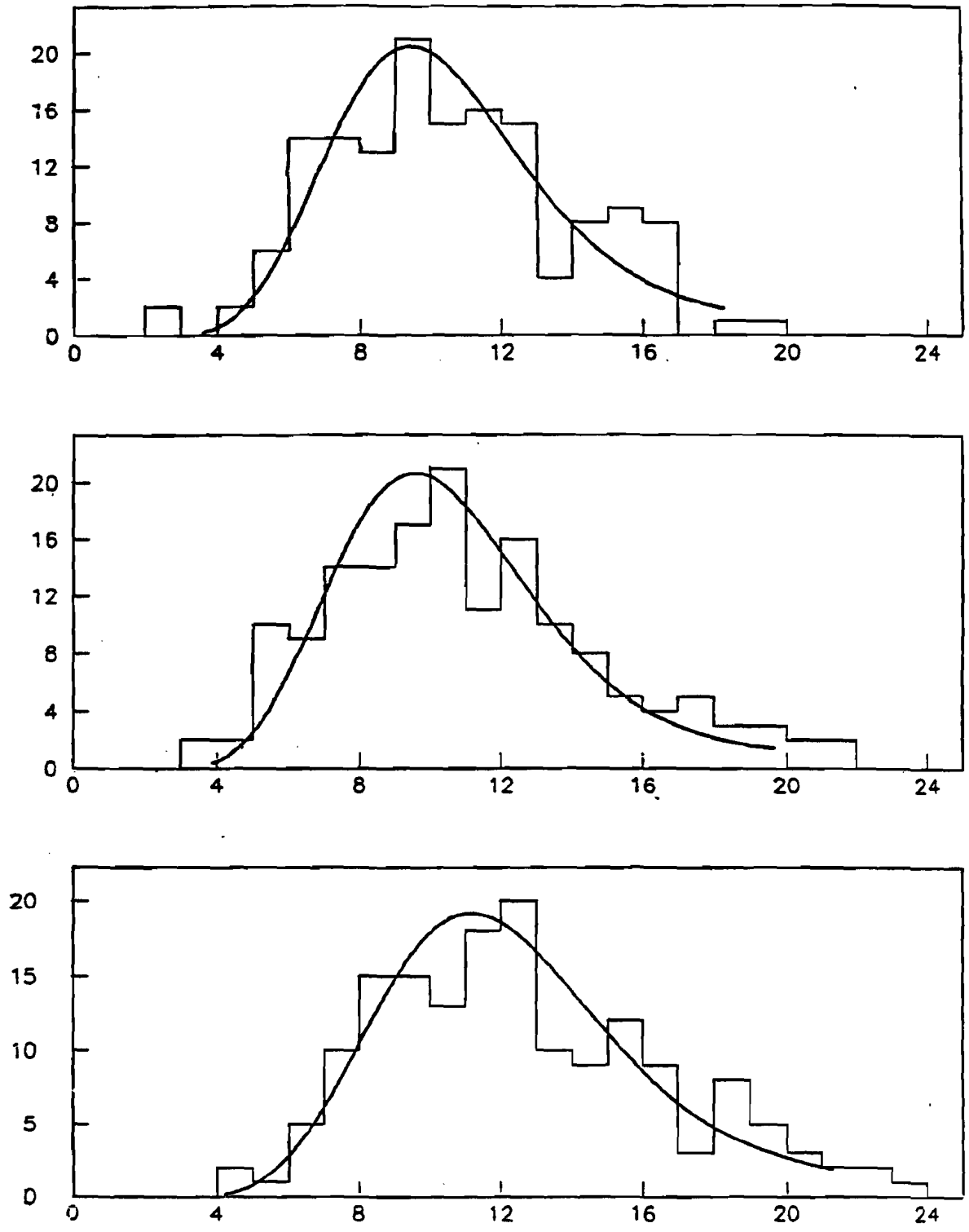

Figure 7.3 The ionization loss distribution for three typical tracks. The smooth curve plotted with the data for each track is the result of the maximum likelihood fit. This is the predicted energy loss distribution for the measured momentum and scale parameter. Note that the horizontal scale (binning factor) has been chosen for each track such that the peak bin contains at least twenty entries.

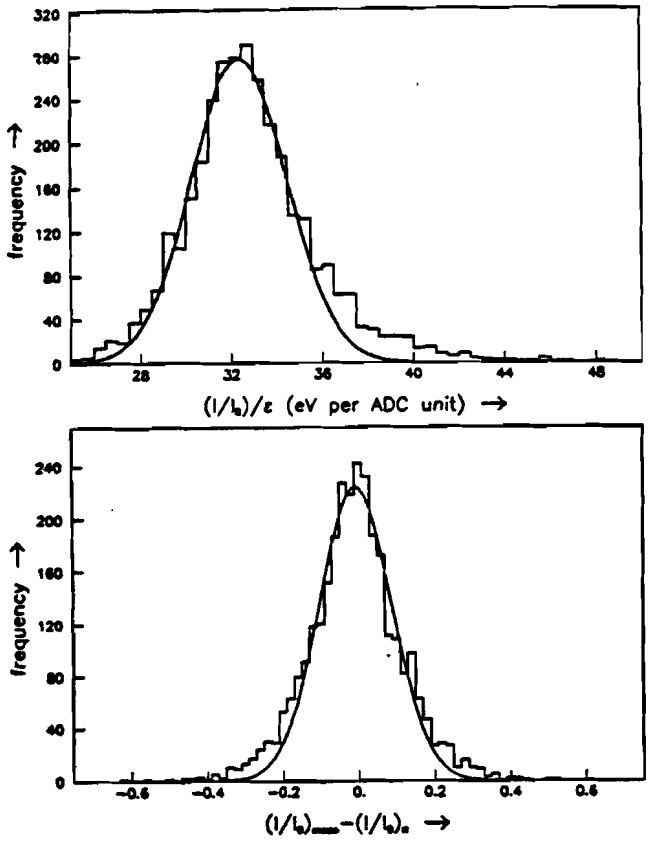

Figure 7.4 At top we see the distribution of the proportionality constant between the measured value of ϵ and the expected ionization I/I_0. Using this normalization constant we then display in the lower plot the distribution of the residual ionization for pion induced events assuming all secondaries to be pions as well. Various cuts and the origin of the smooth curves are described in the text.

7.1.2.4 Ionization loss on the relativistic rise

Using the scale normalization determined in the previous section we have plotted the ionization measurements for all PIG tracks in figure 7.5. This plot shows secondaries from events produced by pion, kaon, and proton beams alike. Recall that geometrical acceptance limits the DPI to tracks with momenta greater than roughly 5 GeV/c. Within the large σ_{I/I_0} we observe general agreement with the expected shape of the relativistic rise. The most energetic tracks, however, deviate from their predicted ionization.

The accumulation of points near the beam momentum of 200 GeV/c are for the most part due to two prong events. Their relatively low ionization is due to the effects of space charge in the region of the straight through beam tracks. We do not expect that this effective degradation in gas gain will impair measurements outside the 1 cm wide beam spot. This is confirmed by examining the data without the

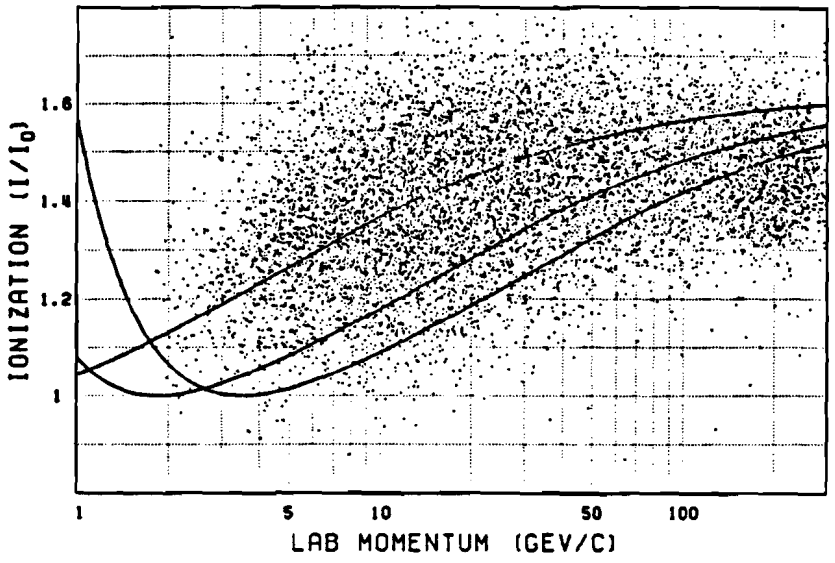

Figure 7.5 The measured ionization loss for secondaries produced in π^+p, K^+p, and pp events of all topologies.

two and four prong topologies as is done in figure 7.6.

We may compare the achieved CRISIS results in figure 7.6 directly with our expectations for that detector in figure 6.7 as the Monte Carlo by its nature does not produce diffractive events. While examining these plots one should bear in mind that the data contains 1529 π, 1082 K, and 1651 p induced events while the Monte Carlo has roughly 1615 events of each beam type. Hence the kaon signal will not be as evident in the data as it is in the simulation. In any event we observe that the poor ionization resolution removes any hope of using this detector for direct particle identification.

We show for reference the ionization plots separately by beam type in figures 7.7, 7.8, and 7.9. Each of the ionization plots have been made with the requirement that the accepted tracks have at least 100 charge samples in order to reduce the number of outlying measurements.

7.1.2.5 Statistical treatment of mass hypotheses

Had the dE/dx detector achieved its design resolution one might imagine using it for track by track particle identification.[5] Given the present level of performance one is forced to pursue other means in extracting the physical content of the data. In the following we describe a statistical procedure used to affect particle identification.

[5] The extent to which this is possible has been investigated in T. B. Stoughton, "Comparison of the Acceptance and Identification Efficiences of a One Module and Two Module CRISIS for the Fermilab Hybrid Spectrometer," DPI Note #3, May 1978.

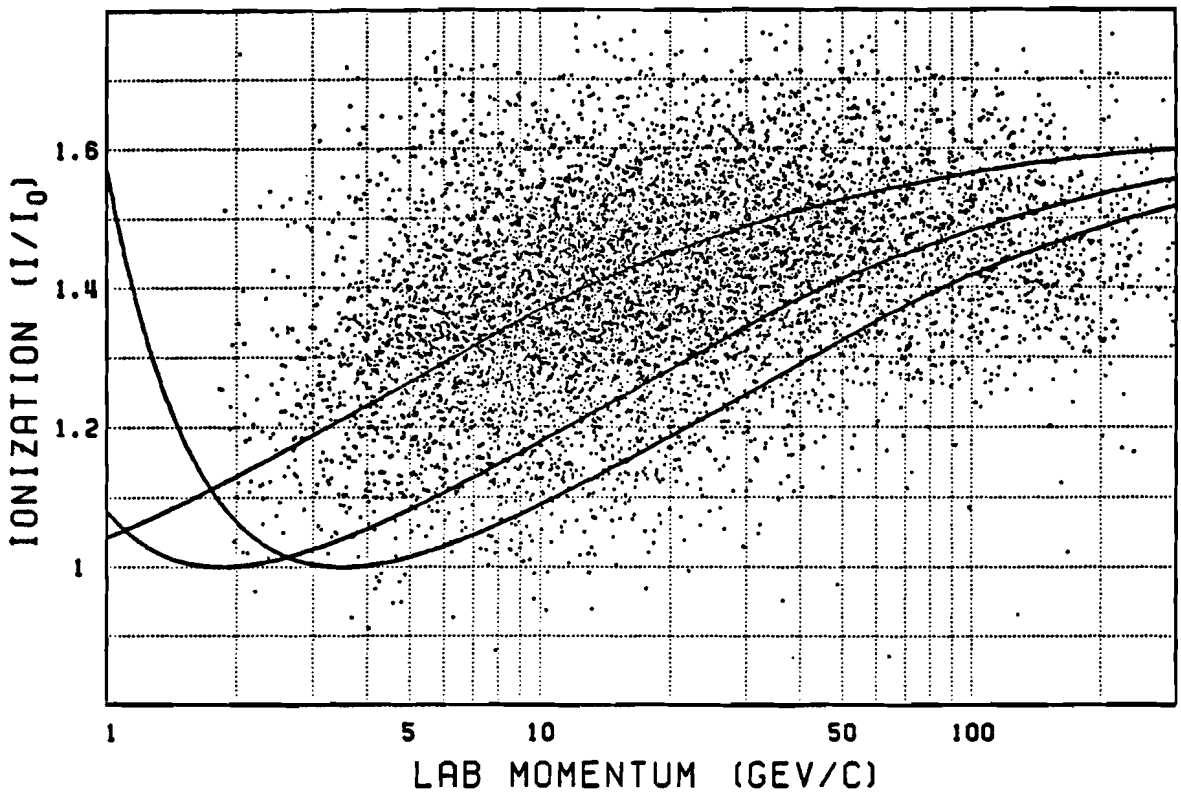

Figure 7.6 The ionization loss for non-diffractive events, all beams.

Due to the predominance of pions in the final state we are faced with a significant signal-to-noise problem in identifying kaons and protons. In order to make the best use of the data we propose to evaluate the probability that a given measurement was due to each of π, K, and p. Single particle distributions will then be created by weighting each entry by its appropriate probability.

In order to ascribe identification probabilities to measurements one needs to know the expected ionization loss for each of the species (e.g. $I_\pi(p)$), the ionization measurement error (σ_I), and the natural abundance of each of the species (e.g. $f_\pi(p)$). With this information we may write a simple expression for the probability that a given measured ionization $\tilde{I}$ at momentum $\tilde{p}$ was due to a specific parent. Denoting the parent particle by h we see that

$$P(h|\tilde{p},\tilde{I}) = \frac{f_h(p)\exp\{-(\tilde{I}-I_h(\tilde{p}))^2/2\sigma_I^2\}}{\sum_{h'=\pi,K,p} f_{h'}(p)\exp\{-(\tilde{I}-I_{h'}(\tilde{p}))^2/2\sigma_I^2\}}$$

We have already calculated $I_h(p)$ and measured the value of σ_I (referred to previously as σ_{I/I_0}). Hence we need only determine the $f_h(p)$ in order to use this statistical identification procedure. One could in principle determine the $f_h(p)$ from the data. This would be best accomidated by binning the

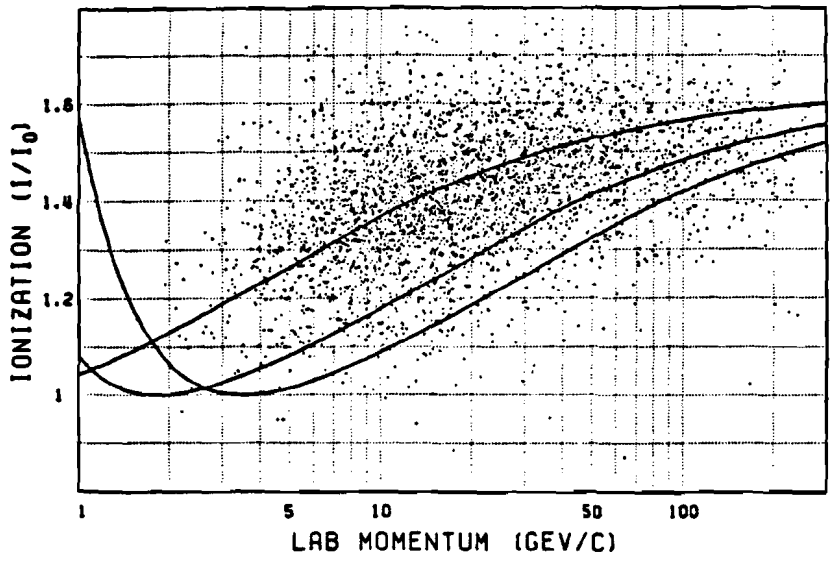

Figure 7.7 The ionization loss for non-diffractive $\pi^+ p$ events.

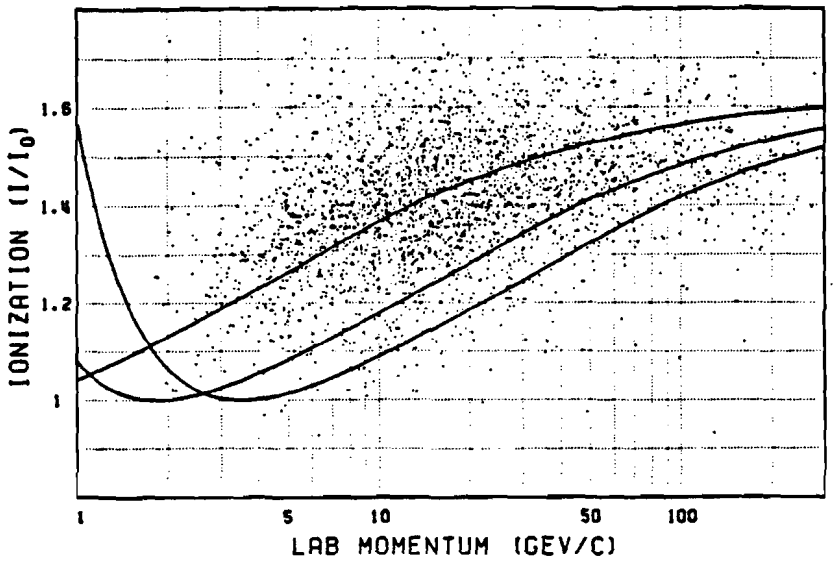

Figure 7.8 The ionization loss for non-diffractive $K^+ p$ events.

data into many momentum slices and for each slice fitting the area of three gaussians to the data. The gaussians would be centered at the $I_h(p_i)$ and have variance σ_I. With our sample of $1.5 \cdot 10^4$ tracks and the relatively large σ_I it seems inappropriate to undertake such a determination. We will instead fix the $f_h(p)$ within a specific model for the strong interaction.

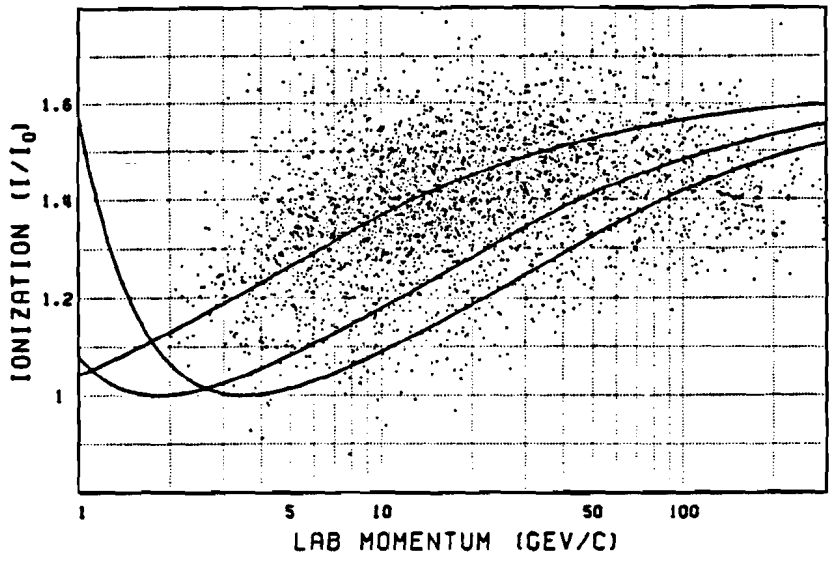

Figure 7.9 The ionization loss for non-diffractive pp events.

Using the Lund model for soft hadronization[6] ten thousand events have been produced for each of the interactions π^+p, K^+p, and pp at a lab momentum of 200 GeV/c. The fractions of produced pions, kaons, and protons have been determined for each of the beam types. The distributions of produced particles are seen in figure 7.10 in terms of their lab momentum. The binning was chosen to be uniform in $\log(p_{lab})$ due to the behavior of the relativistic rise.

We note that in the evaluation of $f_h(p)$ the strange meson has been treated as though it were stable. At a lab momentum of 5 GeV/c 11% of the kaons will decay before reaching CRISIS, while an additional 7% will decay within the detector volume. As the K^+p center of mass has a lab momentum of just 5 GeV/c the above numbers represent an upper limit on the introduced error.

7.2 CORRECTIONS

As there are unavoidable inefficiencies in both the apparatus and the software we must take care to understand their effects so that they may be removed in the final analysis. We will consider in the following the topological reconstruction efficiency, the PIG hybridization acceptance, and finally the losses due to poorly determined ionization.

We have already seen in table 5.3 the topological reconstruction pass rate or efficiency. These numbers have been used in the analysis to weight the entries into histograms according to event topology. In this way the limitations imposed by reconstruction software are hoped to be removed.

---

[6] T. Sjöstrand, op. cit.

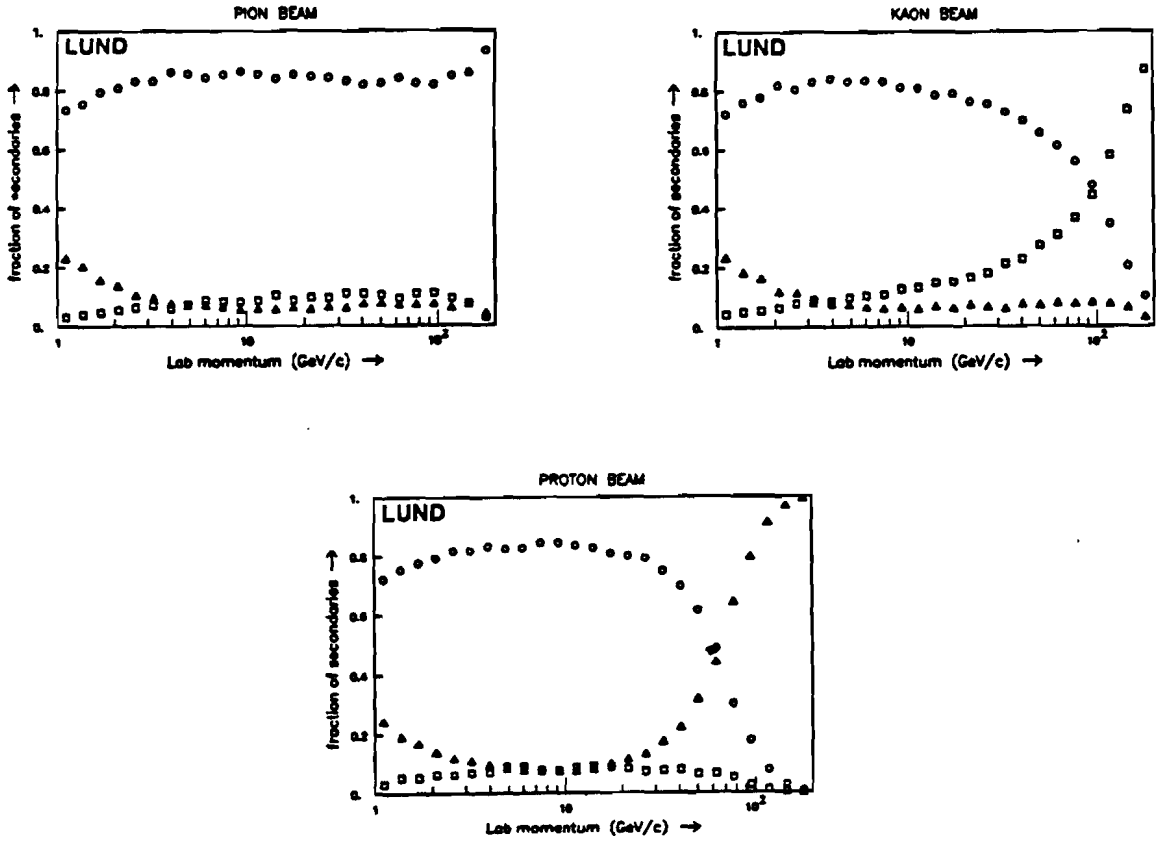

Figure 7.10 Relative abundances of secondaries as predicted by the Lund model. In each plot the symbols are ○ π, □ K, △ p. Both charged states of each particle are included in the distributions. The upper left plot is for $\pi^+ p$ interactions, the upper right for $K^+ p$, and the lower plot is for pp.

With the aid of the simulation package we have seen in §6.3.3 that the DPI acceptance imposes constraints on our ability to perform final state particle identification. At that time it was demonstrated that *GEOHYB* reconstructs tracks equally well regardless of their x_f. The fraction of PIG tracks was seen, however, to have a sharp cutoff near $x_f = 0$. We have carried out a similar analysis using event data in order to estimate the effects of the DPI acceptance. In figures 7.11 thru 7.13 we see the results of this study. These plots show the fraction of tracks reconstructed in a particular class relative to all tracks reconstructed as a function of various kinematic variables. We may compare each of these plots directly with their simulator counterparts found in figures 6.5, 6.6, and 6.9.

In terms of correcting for acceptance we will find figure 7.11 most usefull. We see again that the DPI can only begin to identify particles with x_f slightly larger than zero. Further the efficiency for such reconstruction plateaus at roughly 80%. We have therefore assigned weights $w_{PIG} = \epsilon_{PIG}^{-1}(x_f)$ to tracks when their charge data has been used. The fraction of tracks reconstructed by PIG has been

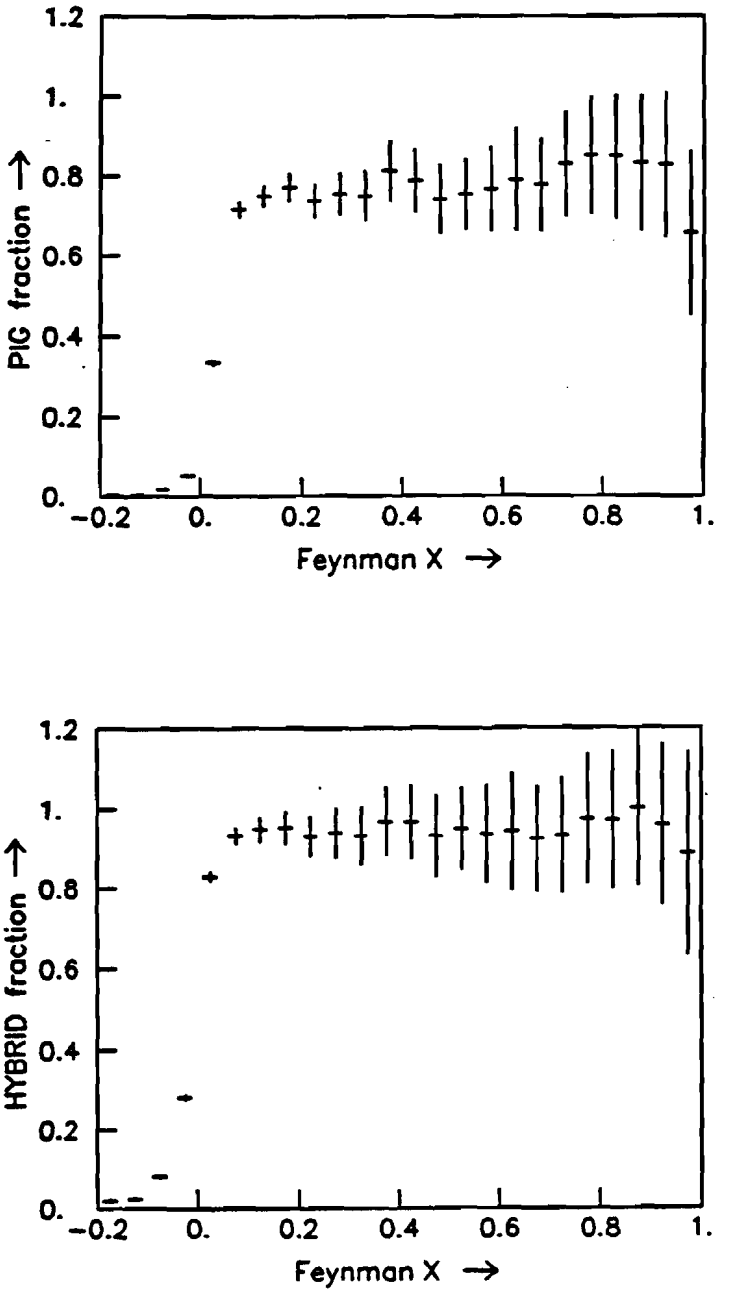

Figure 7.11 Fraction of all reconstructed tracks which were reconstructed using the PIG technique (upper) and the fraction of those which were HYBRID (lower). Both are plotted in terms of the Feynman scaling variable.

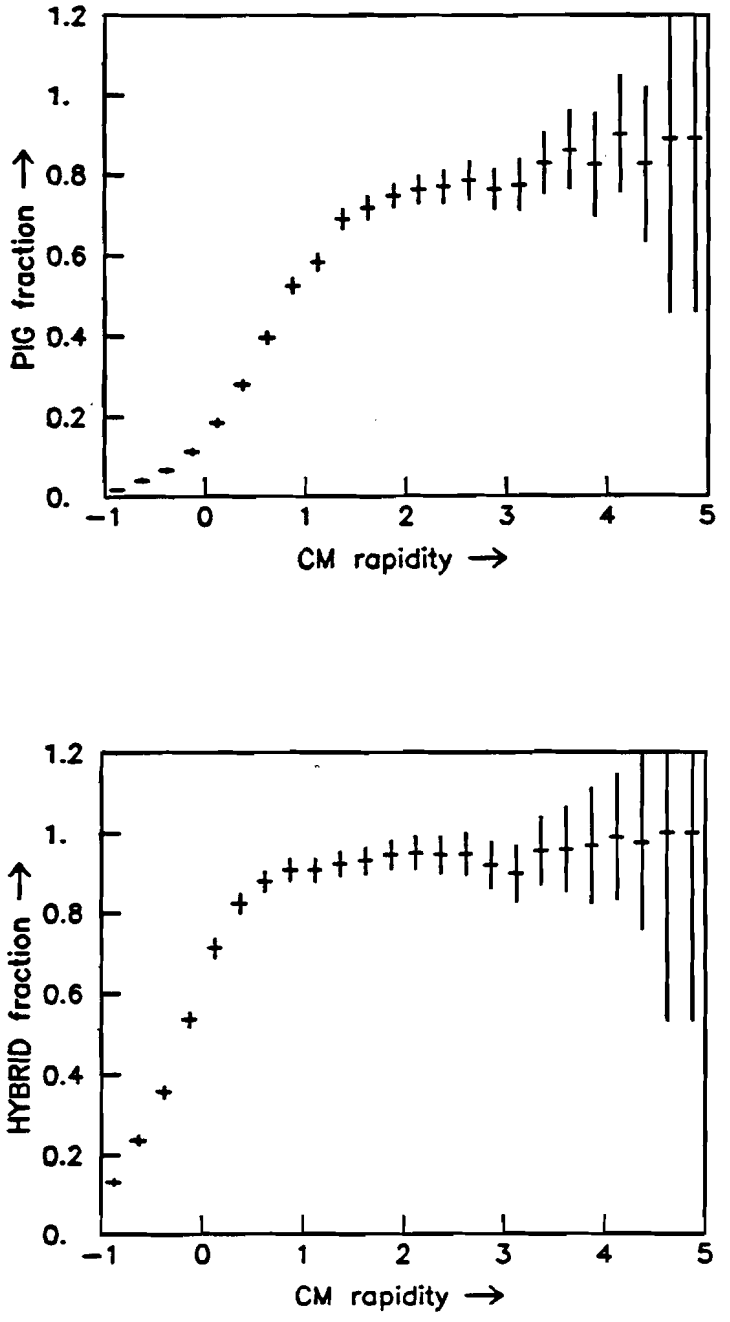

Figure 7.12 The PIG and HYBRID fractions (as in figure 7.11) in terms of the center of mass rapidity.

parameterized as follows

$$\epsilon_{PIG}(x_f) = \begin{cases} 0.217 + 6.61x_f & \text{if } 0 \leq x_f \leq 0.075; \\ 0.8 & \text{if } 0.075 < x_f \leq 1. \end{cases}$$

Figure 7.12 shows the PIG fraction in terms of the center of mass rapidity Y^*. It is evident from the results achieved that the DPI is severely limited in its ablility to support investigations in terms of rapidity correlations. In particular the entire backward hemisphere as well as a major fraction of the first two units in the forward hemisphere do not have particle identification information available. Given that the correlation length is expected to be on the order of one unit of rapidity for the various types of quantum number compensation[7] there is small hope to observe such effects in the data.

The above mentioned figures also show the additional acceptance provided by the wire chambers for improved momentum reconstruction using SOW. While figure 7.13 shows the number of tracks reconstructed by PIG relative to the total reconstructed in terms of the lab momentum.

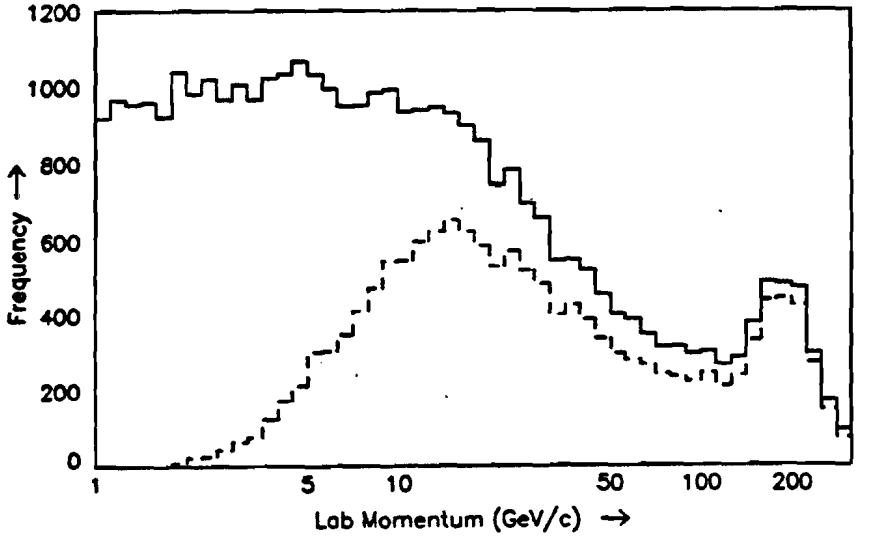

Figure 7.13 The distribution of particles plotted against the logarithm of the lab momentum. The solid histogram is for all reconstructed particles, while the dashed histogram if for PIG tracks only.

Given that a track has been reconstructed with associated charge data by PIG we now seek to determine the fraction of these tracks which have sufficient information with which to attempt particle identification. We find that tracks which are clearly outliers or which have fewer than 100 charge measurements comprise 10% of the data independent of their x_f. Acceptable tracks have therefore been appropriately weighted when their ionization information has been used.

[7] C. Quigg, "Local Quantum-Number Compensation in Multiple Production," Phys. Rev. D 12 (1975) 834.

7.3 GENERAL FEATURES OF THE DATA

We are now in a position to take a first look at the data. This will be done in terms of simple kinematic variables. Labelling the component of momentum along the collision axis as p_l and the perpendicular component as p_t we define the Feynman X variable and the rapidity as

$$x_f = p_l/p^*, \quad \text{and}$$

$$y = \frac{1}{2}\ln\left\{\frac{E+p_l}{E-p_l}\right\}.$$

Here p^* is the initial state momentum of each particle in the center of mass and E is the particle energy calculated from measurements by $E^2 = p^2 + m^2$. By its nature x_f is defined in terms of quantities in the center of mass. We will in the following consider the rapidity exclussively in terms of center of mass variables as well.

A simple cut will be used in order to eliminate the effects of the diffractive component of the hadronic interaction. Unless it is stated otherwise the distributions which follow have been obtained excluding the two and four prong events.

In figure 7.14 we see the x_f distribution for all particles. At $x_f = -1$ we see a narrow spike resulting from target diffraction. The momentum resolution is particularly good here as the recoil protons are reconstructed from their range in the liquid hydrogen. The corresponding diffractive peak in the forward hemisphere has been smeared out by the poor angular resolution which the bubble chamber has for the most energetic tracks. We note the symmetry of this distribution in the central region. Figure 7.15 shows the x_f distribution with the diffractive topologies removed. Here the symmetry persists over the entire range of x_f.

The rapidity distribution is shown in figure 7.16. Note that the maximum allowed values for rapidity in E570 are 5.0, 3.7, and 3.1 units for the pion, kaon, and proton respectively.

As a final check on the global properties of the data we examine the transverse momentum distribution (figure 7.17). We have determined $\langle p_t \rangle = 374 \pm 1\,\mathrm{MeV/c}$. Further, fits have been done to the p_t^2 spectra in the form of $dN/dp_t^2 = a\exp\{-bp_t^2\}$. We find the exponential slope to be $b = -9.8 \pm 0.1(\mathrm{GeV/c})^{-2}$ for a fit domain of $0 \le p_t^2 \le 0.2(\mathrm{GeV/c})^{-2}$ and $b = -8.1 \pm 0.1(\mathrm{GeV/c})^{-2}$ for $0 \le p_t^2 \le 0.4(\mathrm{GeV/c})^{-2}$. The first value agrees within errors with that found by Kafka, et. al.[8] of $10.2 \pm 0.4(\mathrm{GeV/c})^{-2}$ over the same range in p_t^2 for pp collisions at 205 GeV/c.

7.4 THE STRONG INTERACTION

[8] T. Kafka, et. al., "One-, two-, and three-particle distributions in pp collisions at 205 GeV/c," Phys. Rev. D16 (1977) 1261.

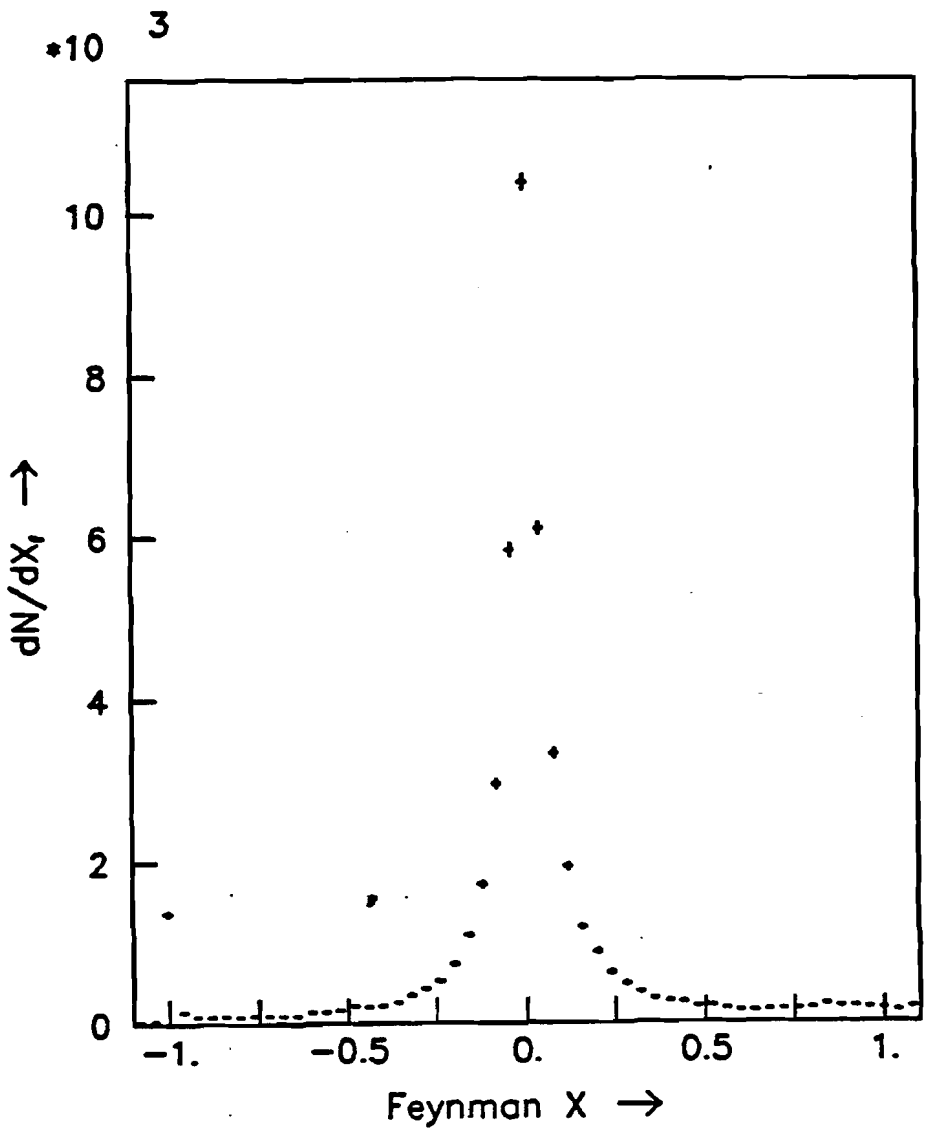

Figure 7.14 Feynman X distribution for all particles.

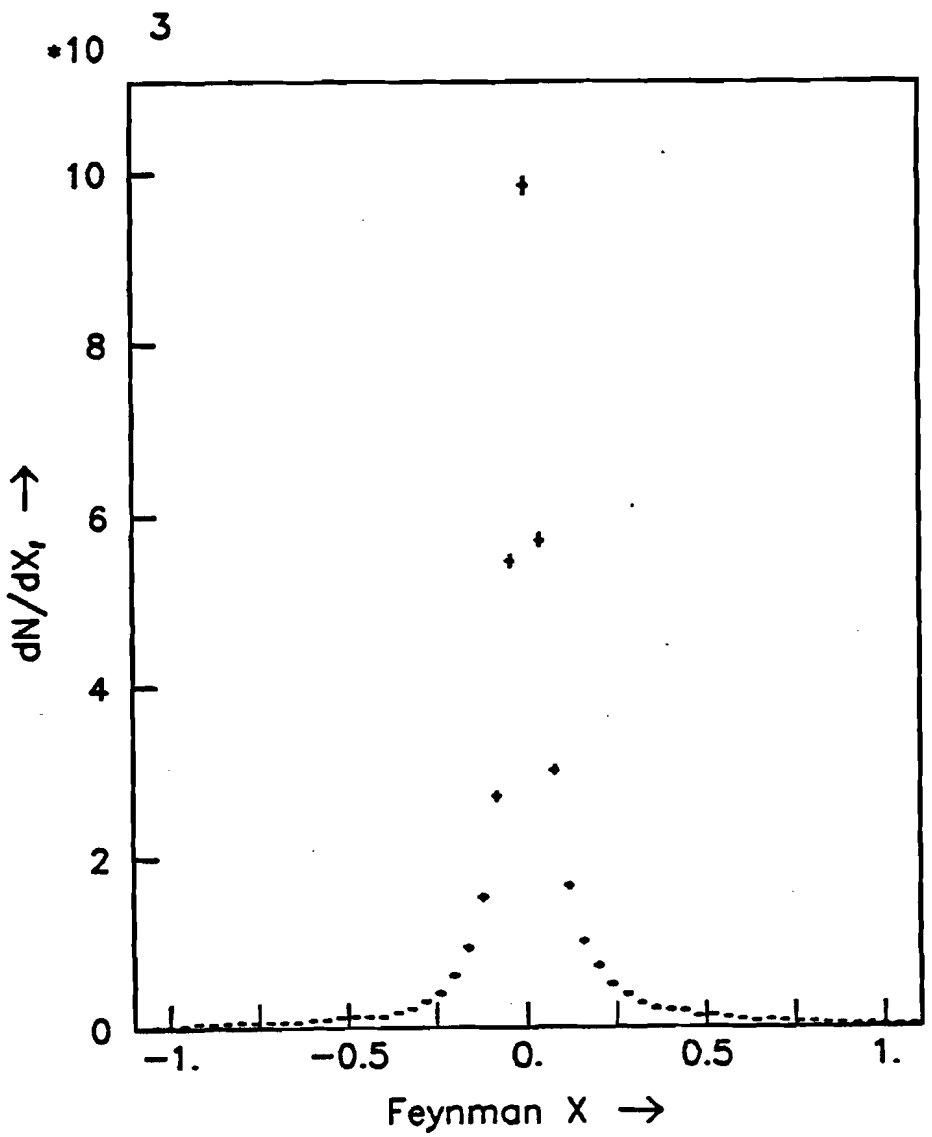

Figure 7.15 Non-diffractive Feynman X distribution.

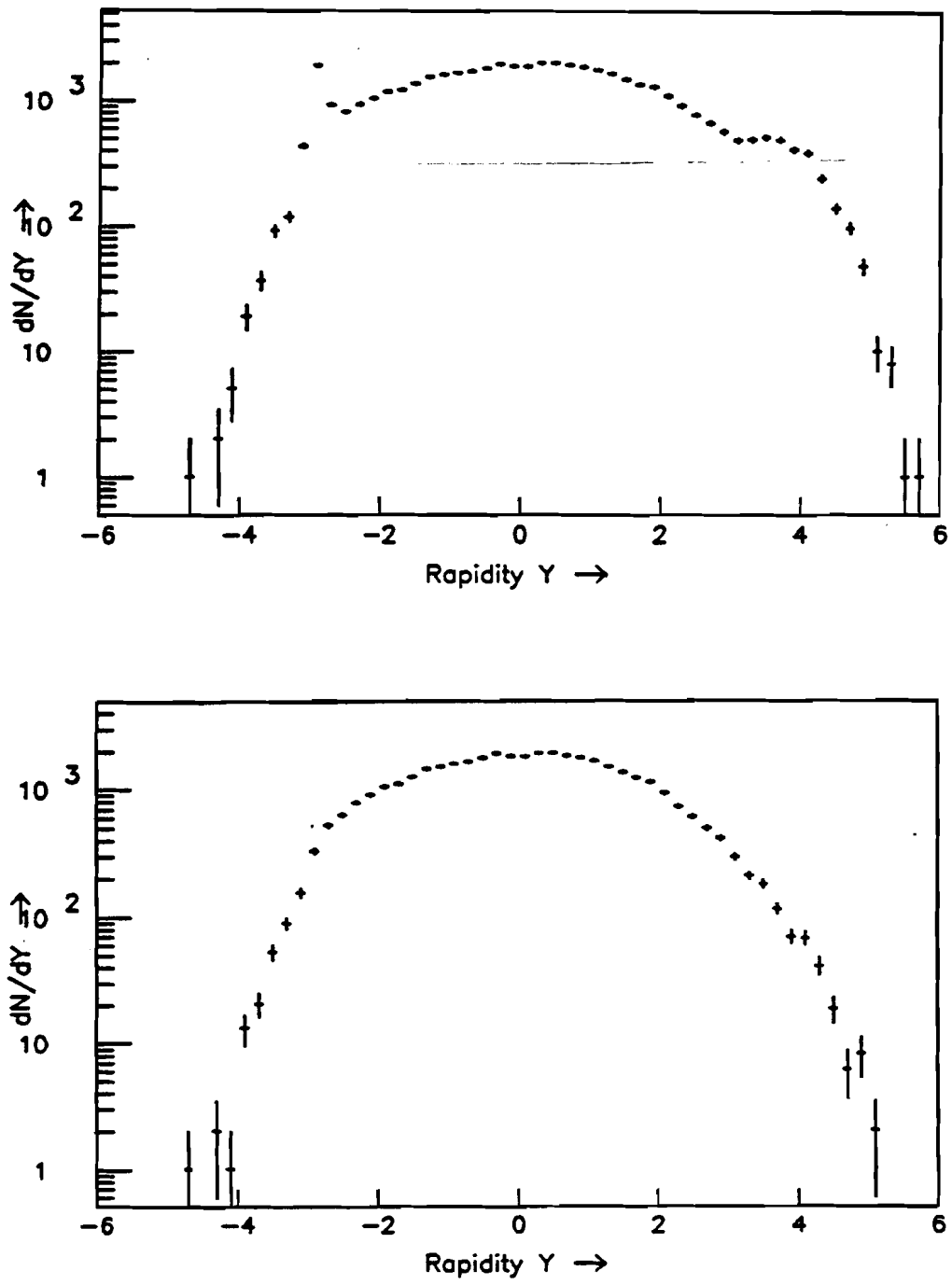

Figure 7.16 The upper plot is the center of mass rapidity distribution for all particles, while the lower plot is the rapidity for non-diffractive events.

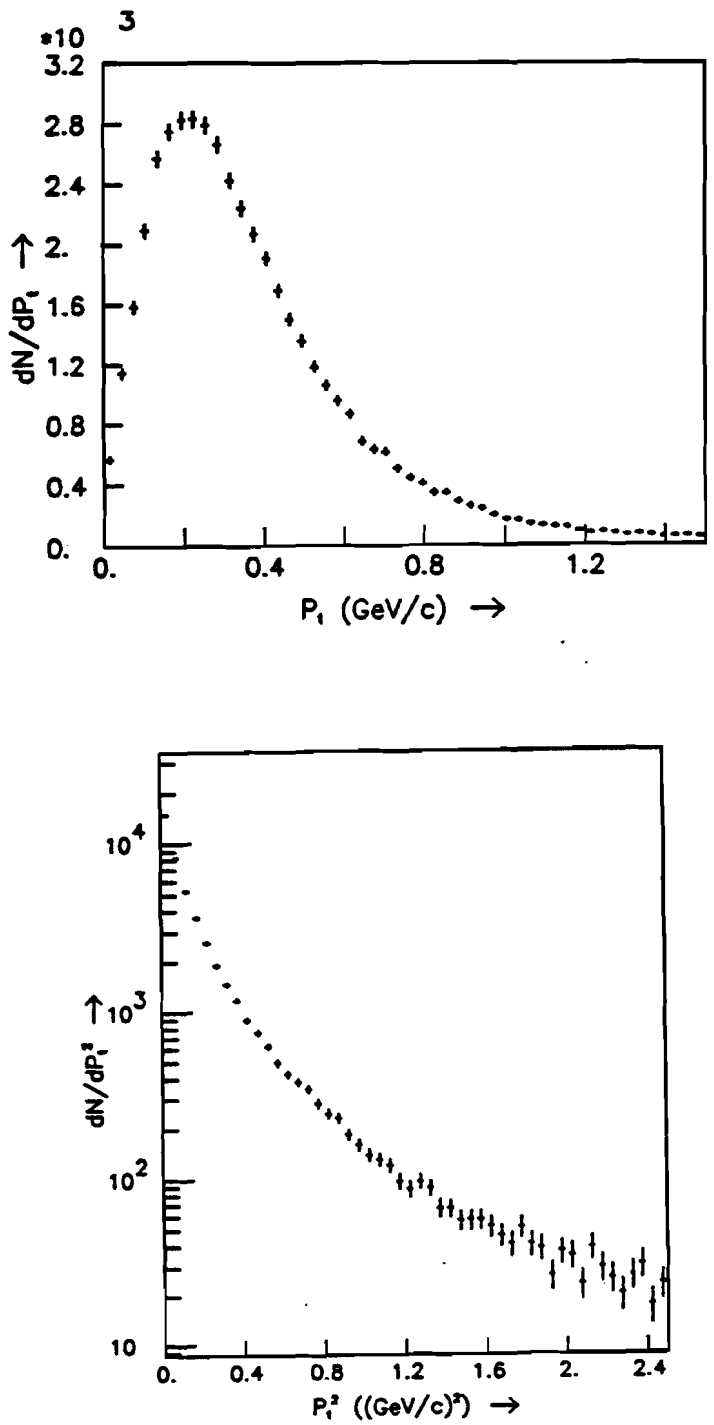

Figure 7.17 The upper plot is the distribution of transverse momentum for all particles. The lower plot is the distribution of the square of the transeverse momentum.

Prior to presenting our results we would like to establish a conceptual basis for their interpretation. As we lack a calculable theory of low momentum transfer hadronic interactions we will content ourselves with the examination of certain models. Each of the models make assumptions regarding the transformation of an initial state wave function into its final state. Although soft hadronic interactions take place within a macroscopic volume of space-time attempts have centered on understanding it in terms of discrete, factorized processes. The simplicity of the assumed strong interaction is typically compensated for by ascribing a large part of the dynamics to the particular mechanism employed to affect confinement.

In the case of hard quark-quark scattering (i.e. high p_t collisions) the validity of seperating the collision process into distinct steps seems more clear cut. Due to the short length scale we can well imagine the description of the initial state in terms of independent constituents. The hard scatter takes place under a distinct transition matrix and involves a specific set of constituents. After the scatter the constituents enter a phase whereby they materialize into final state particles. This interpretation is not specificly justified in soft scattering, but it is nonetheless often applied.

Since we are at a loss to calculate the transition matrix its explicit contribution is generally overlooked in favor of finding a simple description of the gross dynamical features. We therefore picture the process in terms of initial state constituents which ultimately decay into final state hadrons. More specificly the initial constituents (q) are distributed within hadrons (h) according to $f_q^h(x)$. Where x refers to the fraction of momentum carried by q in h. The functions $f_q^h(x)$ could for example be determined by deep inelastic scattering experiments. The constituents are then thought to evolve into hadrons via the decay functions $D_q^h(z)$ familiar from e^+e^- physics. Here z is the fraction of the initial quark's momentum carried off by the produced hadron h. Thus we may write the cross section for a hadron h to fragment into h' as

$$\frac{1}{\sigma}\frac{d\sigma}{dx_f}^{h\to h'} = \sum_q \int dxdz f_q^h(x) D_q^{h'} \delta(xz - x_f).$$

Goldberg[9] and independently Ochs[10] deduced that the fastest constituents in the initial state would have to be reflected in fast mesons in the final state. In essence they asserted that the initial state distribution of constituents would determine the assymptotic x_f behavior in non-leading reactions. That is to say the fast constituents do not take part in the interaction. For example in the reaction $pp \to \pi X$ a fast π^+ could only come from the combination of a fast valence u quark with a $\bar{d}$ quark from the sea. As the electromagnetic structure function describes the probability of finding a u quark within a proton

[9] H. Goldberg, "Predictions for Inclusive Reactions Based on a Parton Structure of Hadrons," Nucl. Phys. B44 (1972) 149.

[10] W. Ochs, "Hadron Fragmentation at High Energies and Quark Constituents," Nucl. Phys. B118 (1977) 397.

as $x \rightarrow 1$ we expect

$$x\frac{d\sigma}{dx} \approx \nu W_{2p}(x).$$

These ideas were made more concrete by Das and Hwa[11] who proposed a specific mechanism for the recombination of quarks into mesons. Rather than the quark decay process mentioned briefly above these authors stress that the formation of hadrons via quark recombination is the dominant process.

Andersson, et. al.[12] have propossed a quite different model based on the observed similarity between the quark fragmentation distribution measured in leptoproduction and the single particle specta in hadroproduction. They ascribe this behavior to the fragmentation of the fast valence quarks. As in the recombination model these authors assume that the fast valence quarks pass through the interaction untouched. In contrast to the recombination model, however, they stress the decay of the leading quarks. Futher they disregard the initial state distribution of quarks in order that the analogy to leptoproduction be reinforced. In leptoproduction the electro-weak probe kicks a single quark out of the target. One is led to a picture in which the struck quark produces a shower of mesons as it receeds from the target remnant. So too in the case of hadron-hadron collisions. Here the so called wee or interacting quarks in each hadron are assumed to partake in the strong interaction while the fast or leading quarks do not participate. The similarity in the spectra of the produced particles is then explained by noting that the leading quark receeds from the interacting quark just as the struck quark receeds from the remnant.

This simple analogy forms the basis for the Lund model. To be more specific the non-diffractive fragmentation distributions in hadronic interactions are assumed to derive from interactions in which one valence quark is essentially stopped in the central region, while the other takes up almost all of the momentum of the initial hadron. This is referred to as a stripping reaction as the interacting quark is stripped out of the hadron. The model is equivalent to assuming $f_q^h(x)$ to be a delta function at $x_f = 1$ for the leading quark, and thus that the fragmentation mechanism contains all of the dynamics.

A semi-classical model was developed in order to investigate the soft hadronization process under the above assumptions.[13] A restoring force is imagined to extend between the interacting and leading quarks. This colored force may be considered to be generated by a massless relativistic string with string constant 1 GeV/fm. The linearly rising potential thus generated ensures confinement and allows

---

[11] K. P. Das and R. C. Hwa, "Quark-Antiquark Recombination in the Fragmentation Region," Phys. Lett. 68B (1977) 459.

[12] B. Andersson, et. al., "A Quark Parton Model for Hadronic Fragmentation Distributions," Phys. Lett. 71B (1977) 337.
B. Andersson, et. al. "The Relationship Between the Meson, Baryon, Photon, and Quark Fragmentation Distributions," Phys. Lett. 69B (1977) 221.

[13] Of particular interest to the present application is B. Andersson, et. al. "A Model for the Reaction Mechanism and the Baryon Fragmentation Distributions in Low p_t Hadronic Interactions," Nucl. Phys. B178 (1981) 242.

for the production of $q\bar{q}$ pairs by breaking the string stochasticly as it is stretched by the receeding endpoint quarks. This model is equivalent to the Schwinger model on one space and one time dimension in QED.[14]

7.5 SINGLE PARTICLE SPECTRA

In considering the various single particle spectra we will chose to emphasize the power law behavior of the invariant differential cross section, viz.

$$E \cdot \frac{d\sigma}{dx_f}^{h^+p \to h'X} \propto (1 - |x_f|)^n.$$

It is the power n which will allow comparison of our data with dissociation model and counting rule predictions as well as with the many existing measurements. When displaying the invariant distributions we will therefore use log-log axis in order to explicitly show the power law behavior.

Recall that the initial states available in E570 are π^+p, K^+p, and pp. Using the statistical identification algorithm we are able to examine the produce spectra of $\pi^\pm$, $K^\pm$, and $p/\bar{p}$. As an introduction to the data we plot in figure 7.18 the invariant distributions

$$E \cdot \frac{dN}{dx_f}^{h^+p \to h'X}$$

were h and h' are chosen from the combinations of π, K, and p. Each individual plot represents the three final state channels produced by a single incident beam type. Note that because the abscissa in each of the plots is $1 - |x_f|$ the fragmentation region appears at the left and the central region at the right.

Along with the E570 measurements are plotted the predictions of the Lund model for each of the appropriate channels. For each beam type the total area of the Lund curves has been normalized to the total number of secondaries in the data. We observe that the Lund distribtutions follow the data well. This is particularly evident in the relative rates of production in the central region.

Along with the distributions for the various beam fragments we have plotted the distributions measured in the target hemisphere. Recall that in the backward hemisphere only pions and protons are identified, and only in the MIT measured data. As the bubble chamber ionization becomes ineffective in identifying protons with $x_f > -0.3$ units we are not suprised by the rapid fall off in the proton curve as x_f approaches zero from below. The forward and backward $p \to \pi$ data disagree as $x_f \to 1$. We speculate that this is due to protons being misidentified in the backward hemisphere. Only positive stopping tracks were taken to be protons. Hence if a stopping track was wrongly flagged as negative due to indeterminacy owing to its short length it would be identified as a pion. We note that otherwise the forward hemisphere $pp \to hX$ and the backward hemishpere $h^+p \to h'X$ data are in quite good

[14] J. Schwinger, "On Gauge Invariance and Vacuum Polarization," Phys. Rev. 82 (1950) 664.

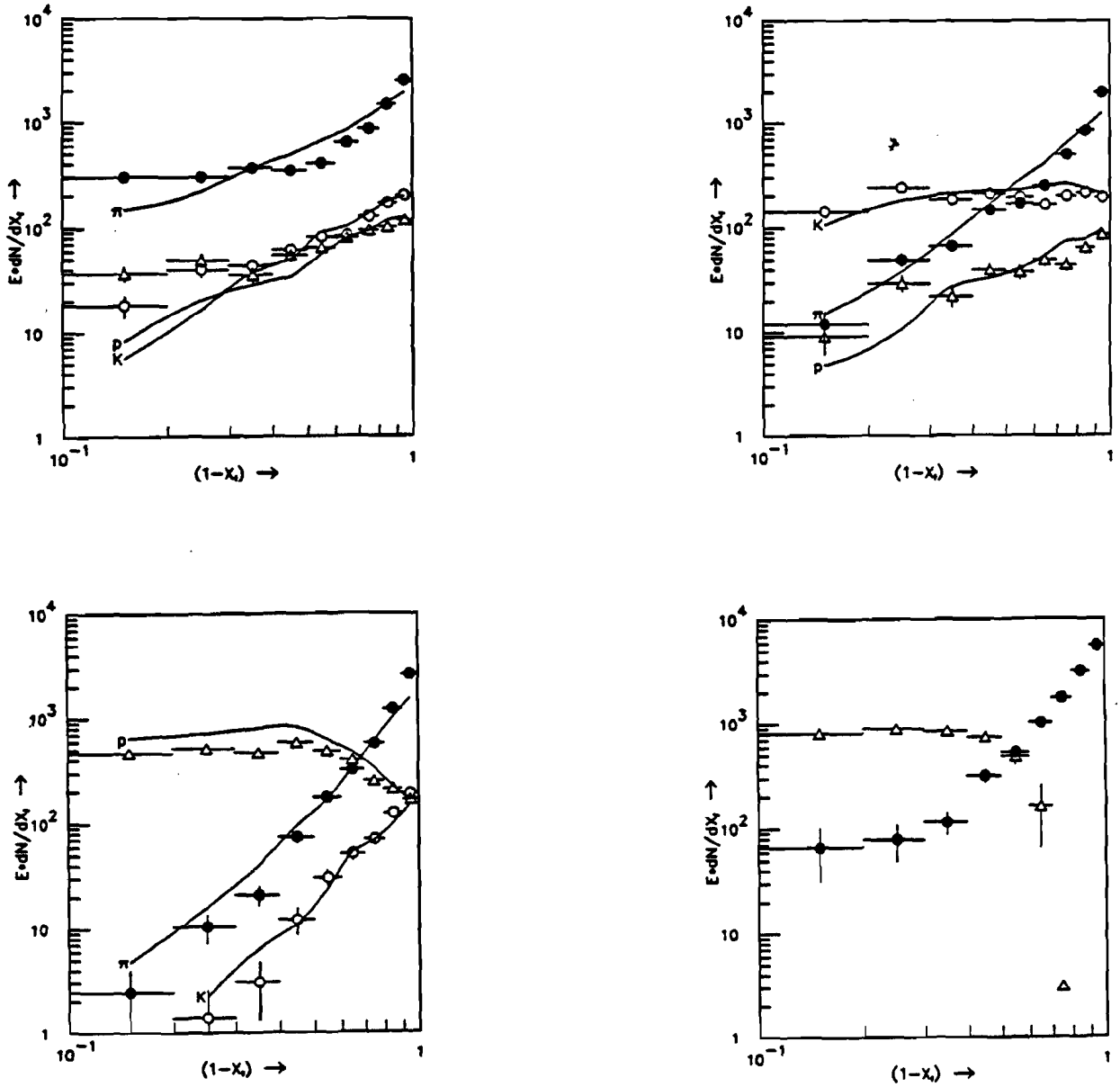

Figure 7.18 The invariant differential $1 - |x_f|$ distributions plotted by beam type. Upper left: pion beams, upper right: kaon beams, lower left: proton beams, and lower right: target protons. Each of the plots shows the measured distributions for produced ○ π, ○ K, and △ p. Note that the first three distributions were arrived at via the statistical weighting scheme devised for the DPI data. Plotted along with the data are predictions made using the Lund model.

agreement. This is particularly significant due to the fact that the forward data were derived using the DPI and statistical mass assignments while the backward data were obtained using unique mass assignments from the bubble chamber ionization.

In figure 7.19 we compare the $p \rightarrow \pi^+$ channel in the forward and backward hemispheres. Recall that the backward data include π and K induced events as well as the pp events which comprise the forward data. This explains the different number of total tracks. It is important to point out that at a beam momentum of 200 GeV/c the fragmentation of a proton is essentially independent of its partner in the hadronic interaction.[15] That is to say the fragmentation depends only on the structure of the proton. We have fit the power n for both distributions and find for the forward data $n = 3.8 \pm 0.2$ and in excellent agreement for the backward data $n = 3.9 \pm 0.1$.

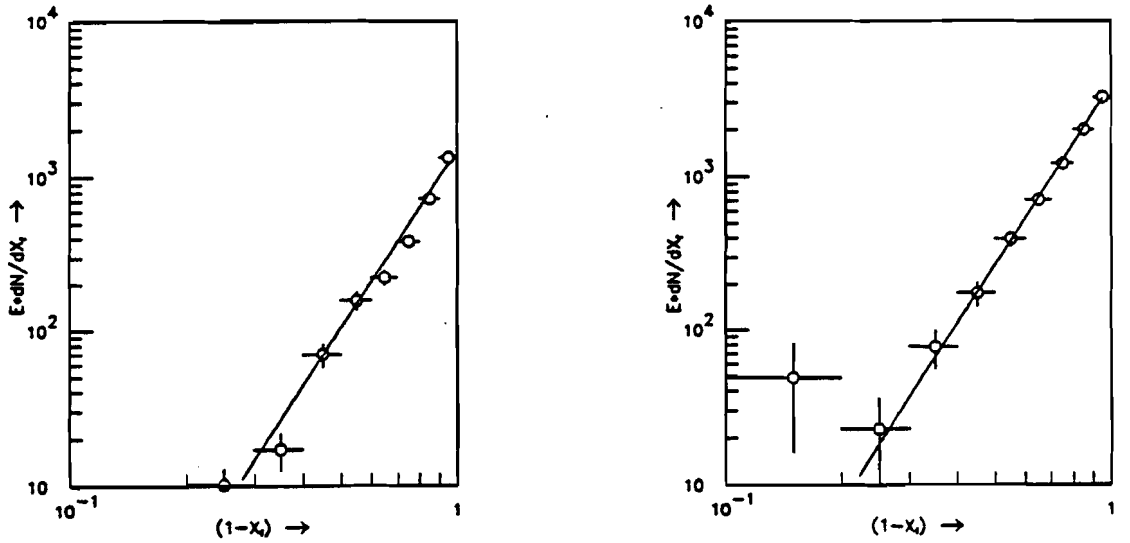

Figure 7.19 At left the invariant $1 - x_f$ distribution for $pp \rightarrow \pi^+ X$ in the forward hemisphere. At right the invariant $1 + x_f$ distribution for $h^+ p \rightarrow \pi^+ X$ in the backward hemisphere.

The errors quoted for the power law fits are due to statistical and systematic sources. In order to estimate the systematic error introduced by the spectrometer we have convolved the resolution function with hypothetical x_f distributions. Assuming $\sigma_p/p^2 = 1.25 \cdot 10^{-3}$ and n in the range of 1 to 5 we have smeared the $(1 - x_f)^n$ behavior and fit the resulting distribution to $(1 - x_f)^{n'}$. In no case was $|n - n'| > 0.1$. We have therefore assigned the error on n to be the statistical error added linearly to 0.1 in order to reflect our uncertainty in the systematic error. The backward result quotes statistical errors only.

[15] D. Brick, et. al., "Approach to Scaling in Inclusive π^+/π^- Ratios at 147 GeV/c," Z. Phys. C13 (1982) 11.

An interesting pair of channels with respect to flavor flow is $K^+p \to \pi^+X$ and $\pi^+p \to K^+X$. We say this because the valence structure of $K^+ = |u\bar{s}\rangle$ and $\pi^+ = |u\bar{d}\rangle$. Hence these particles differ only in a single valence quark. In terms of flavor flow we expect $\pi^+ \to K^+$ and $K^+ \to \pi^+$ to be dominated by the initial state distribution functions for the u quark, $u^{\pi^+}(x)$ and $u^{K^+}(x)$ respectively.

In relating the quark distribution functions to the invariant differential cross section Goldberg predicted that for $\pi^+ \to K^+$ $n = 1$.[16] Figure 7.20 shows the E570 measurement of the π^+/K^+ channels. We find $n = 1.0 \pm 0.2$ for $\pi^+ \to K^+$ and interestingly for $K^+ \to \pi^+$ we find $n = 2.8 \pm 0.2$. This indicates that the u quark within the kaon tends to carry a smaller momentum fraction than the u quark within a pion. Conversely the $\bar{s}$ of the kaon carries a greater momentum fraction than does the $\bar{d}$ of the pion. $\bar{s}^{K^+}(x)$ has been previously commented on in a valon model analysis.[17]

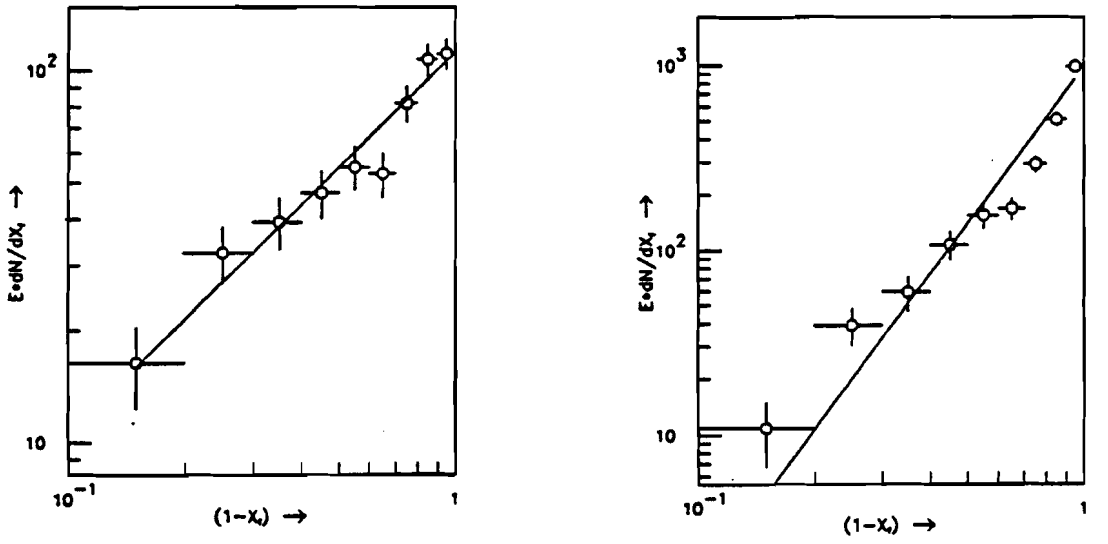

Figure 7.20 At left the invariant $1 - x_f$ distribution for $\pi^+p \to K^+X$ and at right the related channel $K^+p \to \pi^+X$.

The applicability of the hadron dissociation model has been studied by the FSAS[18] and CHLM[19] Rather than repeat their analysis we simply quote our results in terms of the power n in table 7.1.

---

[16] H. Goldberg, op. cit.

[17] L. Gatignon, et. al., "Quark Distributions in the Kaon: A Study of Hadron Structure by Low-p_t Reactions," Phys. Lett. 115B (1982) 329.

[18] W. Aitkenhead, et. al., "Determination of the Pion and Kaon Structure Functions," Phys. Rev. Lett. 45 (1980) 157.

[19] J. Singh, et. al., "Production of High Momentum Mesons at Small Angles at a CM Energy of 45 GeV at the CERN ISR," Nucl. Phys. B140 (1978) 189.

Along with the measurements are listed the average values of other measurements as summarized by Fialkowski and Kittel[20]

TABLE 7.1			
POWER LAW FITS			
channel	E570	world†	c. r.†
$p \rightarrow \pi^+$	3.9 ± 0.2‡	3.4 ± 0.1	3
$p \rightarrow \pi^-$	4.6 ± 0.2‡	4.0 ± 0.1	4
$p \rightarrow \pi^+$	3.8 ± 0.2	3.4 ± 0.1	3
$p \rightarrow \pi^-$	6.7 ± 0.3	4.0 ± 0.1	4
$p \rightarrow K^+$	2.9 ± 0.3	2.9 ± 0.2	3
$p \rightarrow K^-$	5.5 ± 0.4	5.8 ± 0.2	5
$p \rightarrow \bar{p}$	4.4 ± 0.2**	7.6 ± 0.6	5
$K^+ \rightarrow \pi^+$	2.8 ± 0.2	2.3 ± 0.3	1
$K^+ \rightarrow \pi^-$	4.9 ± 0.3	3.0 ± 0.4	3
$K^+ \rightarrow p$	0.9 ± 0.2	2.7 ± 1.3	2
$K^+ \rightarrow \bar{p}$	1.0 ± 0.4**	-	-
$K^+ \rightarrow K^-$	5.1 ± 0.5*	3.4 ± 1.5	3
$\pi^+ \rightarrow p$	2.8 ± 0.2*	2.8 ± 0.1	2
$\pi^+ \rightarrow \bar{p}$	1.8 ± 0.3	2.9 ± 0.3	3
$\pi^+ \rightarrow K^+$	1.0 ± 0.2	1.2 ± 0.1	1
$\pi^+ \rightarrow K^-$	2.2 ± 0.3	2.4 ± 0.3	3
$\pi^+ \rightarrow \pi^-$	2.7 ± 0.2	3.3 ± 0.3	3

†World avg. and counting rule from ref. 20.

‡Target hemisphere data.

* Fit on domain $0 < x_f < 0.7$.

** Poor fit to data.

7.6 CONCLUSION

We have examined the single particle spectra both from the point of view of a fragmentation type model and that of hadron dissociation. We find evidence in support of both ideas.

[20] K. Fialkowski and W. Kittel, "Parton Models of Low Momentum Transfer Processes," Univ. of Nijmegen preprint HEN 82-226, published in Rep. on Prog. in Phys.

Differentiation between the models lies beyond the consideration of flavor flow. Further investigation into the correlations among the final state particles is therefore necessary.

Appendix A

CALCULATION OF THE ELECTROSTATIC POTENTIAL

This appendix is concerned with the problem of calculating the electrostatic potential inside a drift chamber cell. The solution is in general dictated by the geometry of the chamber. Planar drift chambers possess a natural symmetry due to the periodic structure of the cells. In addition the IHSC drift chambers had an additional symmetry in that they were fabricated with conducting windows. As a result each of the wires in the cell had an infinity of *mirror images* in the pair of conducting planes. The ensuing pole structure of the potential function dictates the solution proposed by Tomitani.[1]

We may recall that complex functions satisfy the two dimensional Laplace equation $\nabla^2\Phi = 0$. Consider a line charge (of linear charge density λ) within a conductor of rectangular cross section. The use of a conformal mapping under the Jacobian elliptic function $sn(z)$ transforms the surface of the conductor in z space into a plane in ω space as seen bellow.

The Jacobian elliptic function finds its definition in $sn(z) = u$, where

$$z = \int_0^u [(1-t^2)(1-k^2t^2)]^{1/2}dt.$$

---

[1] T. Tomitani, NIM 100 (1972) 179

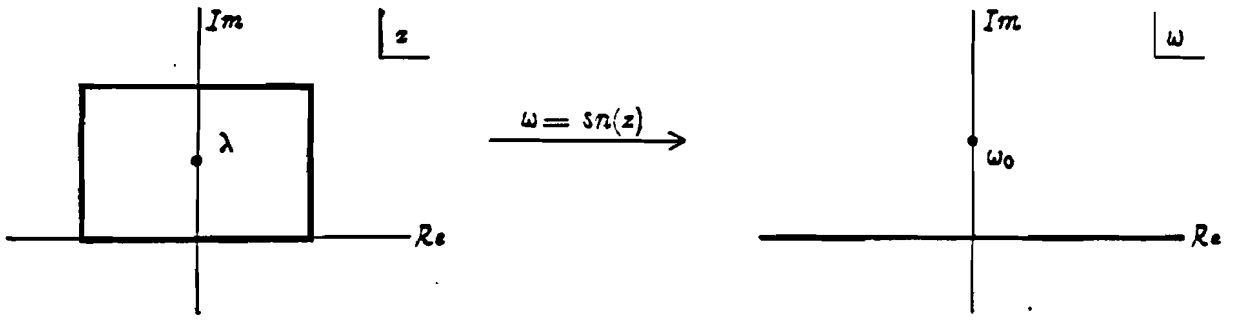

The modulus k is in this case determined by the aspect ratio of the rectangular cross section.

It is now a simple matter to evaluate $\Phi(\omega)$. First we calculate the field due to a line charge:

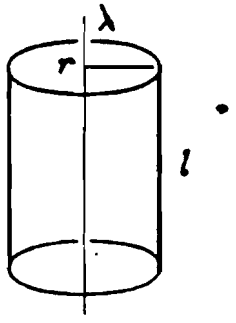

$$\nabla \cdot \vec{E} = 4\pi\rho$$

$$\int \nabla \cdot \vec{E} dv = \int \vec{E} \cdot d\vec{a} = 4\pi q$$

$$2\pi r l E = 4\pi\lambda l$$

$$E = \frac{2\lambda}{r}$$

$$\vec{E} = -\nabla\Phi, \text{hence}$$

$$\Phi = -2\lambda \ln r$$

and, by superposition the field due to the line charge and its image in the conductor:

$$\Phi(\omega) = -2\lambda \ln(\omega - i\omega_0) + 2\lambda \ln(\omega + i\omega_0).$$

Using the inverse transform we obtain the solution

$$\Phi(z) = -2\lambda \ln \frac{sn(z) - i\omega_0}{sn(z) + i\omega_0}$$

and finally the scalar potential $\phi(z) = \Re\{\Phi(z)\}$.

This argument is only slightly changed when considering a periodic grid of wires. Here there are only two conducting planes and a series of like charged wires. Thus we wish to change the boundary conditions such that the scalar potential is zero on two of the opposing faces of the rectangle while the electric field is zero on the other two faces In particular the configuration in z space is rearranged so that each of the identical anodes is mapped to the same point in the ω plane. The resulting potential is

$$\Phi(z) = -2\lambda \ln \frac{sn(z) - \omega_0}{sn(z) + \omega_0}.$$

Having found the solution for a single wire we use superposition to evaluate the field due to an array of n wires held at various fixed voltages. We may express this in the matrix equation $V = C^{-1}Q$,

where the C_{ij}^{-1} represent the potential at wire i due to a charge Q_j residing on wire j. The matrix C is made up of the mutual capacitances of the wires and as usual is derived strictly from the geometry of the system. Given the voltages, locations, and radii of the various wires we are able to invert the matrix C^{-1} and obtain the charges λ_i induced on each wire due to the impressed voltages.

The scalar potential at any point z' is then evaluated by a superposition of these charges in the form

$$\phi(z') = \sum_{i=1}^{n} \lambda_i \phi(z' - z_i).$$

Appendix B

TRACK FITTING IN THE CHEBYSHEV NORM

As we have seen in §4.3 track fitting in wire chambers can be done in the χ^2 sense. This proceedure, however, involves a quite unphysical assumption with regard to proportional wire chambers in as much as the residuals are considered to be normally distributed about the wires. Considering the structure of a PWC we would expect, to the contrary, the residuals would be uniformly distributed about the wires. This is so because any track passing within a half wire spacing of a sense wire will cause it to register a hit. Affects such as track inclination and the firing of adjacent wires for a single track will inevitably distort this distribution, but the result will still be far from Gaussian.

We see therefore that tracks in wire chambers may be more aptly described by a trajectory which is merely required to pass somewhere within a half wire spacing of each of the struck wires. Since such a trajectory is in general not unique we will presently focus our attention on that trajectory which *also* minimizes the largest deviation of the track fit from the wire hits. The trajectory just described is the Chebyshev solution to an overdertermined system of equations.

This appendix is intened to introduce the reader to parameter estimation in the Chebyshev norm.

B.1 THE L_p NORM

Consider a set of n measurements y_i and a linear relationship to m parameters x_i describing these

measurements, viz.

$$y_i = \sum_{j=1}^{n} a_{ij} x_j .$$

In the case that the system of equations is overdetermined (ie. $n > m$) we are faced with the choice of a *measure of the residuals* which gives the *best* solution to our problem. This can be made more concrete by requiring the solution to be the set of parameters $\mathbf{x}^{(p)}$ which obtains the minimum in the L_p norm[1]

$$y - ax_p = \left\{ \sum_{i=1}^{n} \left| y_i - \sum_{j=1}^{m} a_{ij} x_j^{(p)} \right|^p \right\}^{\frac{1}{p}} .$$

The power p may take on any value in the range $0 < p < \infty$ although in practice there are only a few L_p norms which find widespread use. The solution vector $\mathbf{x}^{(p)}$ has an explicit dependence on the *choice* of p. We recognize for $p = 2$ that the L_2 solution is in fact the χ^2 solution. What we must also recognize is that the distribution of random fluctuations in the data influence the effectiveness of the various L_p norms.

The L_2 estimator is known to be the most efficient estimator for fluctuations governed by the normal distribution. The variance of the parameter estimates is given by the familiar $\sigma^2 = 1/n$ for large samples. For the uniform distribution the L_2 norm is no longer the most efficient it being superceeded by the L_∞ (or Chebyshev) norm. In fact (and again for large samples) $\sigma^2_{L_\infty} = 1/2n^2$ while $\sigma^2_{L_2} = 1/12n$.[2] Hence the Chebyshev result is expected to be superior for $n > 6$.

Refering to the expression above we see that the power $p = \infty$ implies the desired solution minimizes the maximum deviation. That is the largest term in the sum dominates as $p \to \infty$.

An overdetermined system of equatinos may be solved in the Chebyshev sense via the familiar Jordan elimination. But because the Chebyshev problem can be reduced to the linear programming problem more sophisticated algorithms are available.[3] In the following a modified version of the simplex method will be used to evaluate solutions.[4]

B.2 THE TRACK FITTING PROBLEM

The determination of track parameters in free space is specified by the solution to the system of equations

---

[1] See for example J. R. Rice and J. S. White, "Norms for Smoothing and Estimation," SIAM Review 6 (1964) 243.

[2] H. Cramér, "Mathematical Methods of Statistics," (Princeton: Princeton University Press, 1946).

[3] E. Stiefel, "Note on Jordan Elimination, Linear Programming, and Tchebycheff Approximation," Numerische Mathematik 2 (1960) 1.

[4] I. Barrodale and C. Phillips, "Algorithm 495: Solution of a Overdetermined System of Linear Equations in the Chebyshev Norm," ACM TOMS 1 (1975) 264.

discussed in §4.3.3, which we repeat presently.

$$\rho = \mathbf{B}\eta$$

$$\begin{pmatrix} \rho_1 \\ \vdots \\ \rho_i \\ \vdots \\ \rho_n \end{pmatrix} = \begin{pmatrix} \vdots & \vdots & \vdots & \vdots \\ -\sin\alpha_i & -x_i\sin\alpha_i & \cos\alpha_i & x_i\cos\alpha_i \\ \vdots & \vdots & \vdots & \vdots \end{pmatrix} \begin{pmatrix} y_0 \\ a_y \\ z_0 \\ a_z \end{pmatrix}.$$

Again the ρ_i are measured track impact parameters in planes at fixed x_i and orientation α_i. The solution vector η describes the track's intercepts and slopes.

Referring to the individual fit residuals as r_i we seek the Chebyshev solution η which yields

$$\min_{\eta} \left\{ c(\eta) = \max_{1 \le i \le n} \left| \frac{r_i(\eta)}{\delta_i} \right| \right\},$$

the δ_i representing the *interval* of measurement y_i. Although it represents a strict limit we can imagine the interval δ to be on the same plane as the more familiar standard error σ.

For a perfect wire chamber δ_i would be half the wire spacing and only tracks which had $c(\eta) < 1$ would be physically possible. We observe that $c(\eta)$ can therefore be usefull in track finding by rejecting *impossible* tracks with $c(\eta) > 1$. For if $c(\eta)$ were to exceed unity a different wire would have been struck!

As was already mentioned parameter estimates are made by solving the overdetermined system of n equations (one for each wire plane) in $m = 4$ unknowns using a technique from linear programming. This proceedure carries out roughly as many $n \times m$ matrix inversions as there are parameters.

The problem of interval estimation has been addressed by James[5] who proceeds as follows. The track is always required to fall within strict limits of the hit wire in each plane. Any deviation from these limits causes the track to be classified unphysical. Hence interval estimates are found by *forcing* the solution to deviate as much as is possible from the best solution and yet still remain a track. The tollerable limits for parameter η_k are found by the addition of a single constraint equation to the system (B.3)

$$\begin{pmatrix} \vdots \\ \vdots \\ \rho_{n+1} \end{pmatrix} = \begin{pmatrix} \vdots & \vdots & \vdots \\ \vdots & \vdots & \vdots \\ 0 & \cdots \mp\epsilon_k \cdots & 0 \end{pmatrix} \begin{pmatrix} \vdots \\ \eta_k \\ \vdots \end{pmatrix}.$$

The negative (positive) sign of ϵ_k causes η_k to shrink (grow) until the maximum residual reaches ρ_{n+1} (provided no other is larger). This gives a lower (upper) bound on η_k. The choice $\rho_{n+1} = \delta$ makes

[5] F. James, "Fitting Tracks in Wire Chambers Using the Chebyshev Norm Instead of Least Squares," CERN DD/82/14, Sept. 1982. (submitted to NIM)

the maximum residual δ per force. And by choosing $\epsilon_k \eta_k \ll \delta$ the new solution is not biased significantly by the introduction of ϵ_k.

The reader may imagine the process of translating or rotating the best track fit in space until it runs into a boundary in some plane. By varying each parameter independently the full range of permissable errors are found.

Appendix C

IONIZATION LOSS OF CHARGED PARTICLES

The numerical realization of a theory of ionization loss of relativistic particles is described. Calculation of the energy loss distribution in gasseous detectors is discussed. By the inclussion of a seperate density effect term predictions are made regarding the relativistic rise in ionization. Results are compared to existing data.

Contributions to this field have been made by several authors. The present work benefits from many of the major conclusions of the past, but exclussively so through an analytic formulation achieved by Talman.[1] This theory is a generalization of Landau's and extends a valid description of ionization loss to the current generation of dE/dX detectors.

C.1 TALMAN'S THEORY

The interested reader is refered to Talman's paper for the details of his theory of ionization loss. In the following we describe only the basic elements.

One may consider the energy loss problem in terms the energy lost in an infinitesimal path length element. This yields a convolution integral in terms of the energy loss distribution and the atomic scattering cross section. Talman solves the convolution integral via a Laplace transform. This is done

---

[1] Richard Talman, "On the Statistics of Particle Identification Using Ionization," NIM 159 (1979) 189

using a simple approximation for the scattering cross section. The measured atomic photo-ionization cross section is used to determine the binding energies ϵ_s and oscillator strengths f_s for the atomic electrons.

In the following we follow the notation of Talman. x is the product of the depth of penetration in the gas and the gas pressure P. Δ is the total energy loss up to the distance x. We note that

$$\xi = \frac{2\pi N_e^4 \rho Z}{mc^2 A}\left(\frac{x}{P}\right),$$

and that P_s represents the mean number of excitations (discrete plus continuous) of level s.

C.2 NUMERICAL IMPLEMENTATION

The problem at hand is the evaluation of the joint probability distribution function

$$f(x,\Delta) = \frac{1}{\pi\xi}\int_0^\infty \exp\left\{\sum_s f_s y si\left(\frac{\epsilon_s y}{\xi}\right) - \sum_s P_s\left(1-\cos\left(\frac{\epsilon_s y}{\xi}\right)\right)\right\}$$
$$\times \cos\left\{\frac{y\Delta}{\xi} + \sum_s f_s y Ci\left(\frac{\epsilon_s y}{\xi}\right) - \sum_s P_s \sin\left(\frac{\epsilon_s y}{\xi}\right)\right\} dy.$$

$Si(x)$ and $Ci(x)$ are respectively the sine and cosine integrals. They are defined by

$$Si(x) = \int_0^\infty \frac{\sin t}{t} dt = si(x) + \pi$$

and

$$Ci(x) = \gamma + \ln x + \int_0^\infty \frac{\cos t - 1}{t} dt.$$

These functions may be approximated on two seperate domains[2]. For $x < 1$ the series expansions

$$Si(x) = \sum_{n=0}^{\infty} \frac{(-1)^n x^{2n+1}}{(2n+1)(2n+1)!}$$

and

$$Ci(x) = \gamma + \ln x + \sum_{n=1}^{\infty} \frac{(-1)^n x^{2n}}{2n(2n)!}$$

have been used up to and including $n = 5$. For $1 \leq x < \infty$ the integrals were evaluated by rational approximation of their auxillary functions $f(x)$ and $g(x)$.

$$Si(x) = \frac{\pi}{2} + f(x)\cos x - g(x)\sin x$$

$$Ci(x) = f(x)\sin x - g(x)cosx$$

Both $f(x)$ and $g(x)$ were obtained after Hastings[3] as the ratio of five term polynomials.

---

[2] M. Abramowitz and I Stegun, "Handbook of Mathematical Functions," (New York: Dover, 1972) pp. 231-233.

[3] C. Hastings, Jr., "Approximations for Digital Computers," (Princeton: Princeton University Press, 1955).

We observe that the integrand in the equation for $f(x,\Delta)$ is the product of an exponential and a cosine in y, viz.

$$K(x) = \exp\{h_1(y)\} \times \cos\{h_2(y)\}.$$

The damped oscillitory behavior of the kernal $K(x)$ works to effectively restrict the range of integration. The scale of this damping is governed by the number of discrete and continuous excitations $P = \sum_s P_s$. From the point of view of energy loss (Δ) the dependance appears more or less as a frequency in the cosine term. It is in fact this frequency which governs the total area under the curve. Very long wave lengths are damped immediately. When the half wave length reaches the damping constant the area is maximal. And very short wave lengths produce oscillations whose area tend to cancel.

Numerically then one need only be concerned first about the selected range of integration and second that the integration technique used is sufficiently sensitive to the higher frequency oscillations. Integration was accomplished using 32-point Gaussian quadriture [4]. This technique will integrate exactly any polynomial of order up to 63. Tests were carried out to investigate the precision of the integration. The domain of integration was divided into four regions of integration. Summing the results of integrating over the subdivisions produced results which agreed with the single integration to better than 0.01%. For this reason it was decided to use a single integration on a domain determined by observing the behavior of $K(x)$.

In his paper Talman expresses concern over the exact treatment of the most tightly bound electrons. To investigate this the Argon K-shell electrons have been treated continuously and then as discrete excitations. The resulting energy loss distributions were essentially the same. Clearly the numerical superiority of the present treatment alleviates the concern expressed by Talman.

As this theory does not explicitly take into account the density effect we have added to the formula for the enegy loss Sternheimer's correction.[5]

C.3 COMPARISON WITH DATA

In order to test both the model for ionization loss and the current numerical implementation we have made comparison with existing data. Figure C.1 shows the energy loss distribution calculated for 3 GeV/c electrons in 1.5 cm samples of an 80/20 mix of Ar/CO_2. This is compared with the data of Harris, et. al.[6] The measured data was taken in a gas mixture of 93% argon and 7% methane. The theoretical

[4] See for example V. I. Krylov. "Approximate Calculation of Integrals," (New York: Macmillan, 1962)

[5] R. M. Sternheimer, et. al., "The Density Effect for the Ionization Loss of Charged Particles in Various Substances," BNL 31435.

[6] F. Harris, et. al., "The Experimental Identification of Individual Particles by the Observation of Transition Radiation in the X-ray Region," NIM 107 (1973) 413.

curve has been normalized to the peak of the experimental data. We see that the two are in quite good agreement.

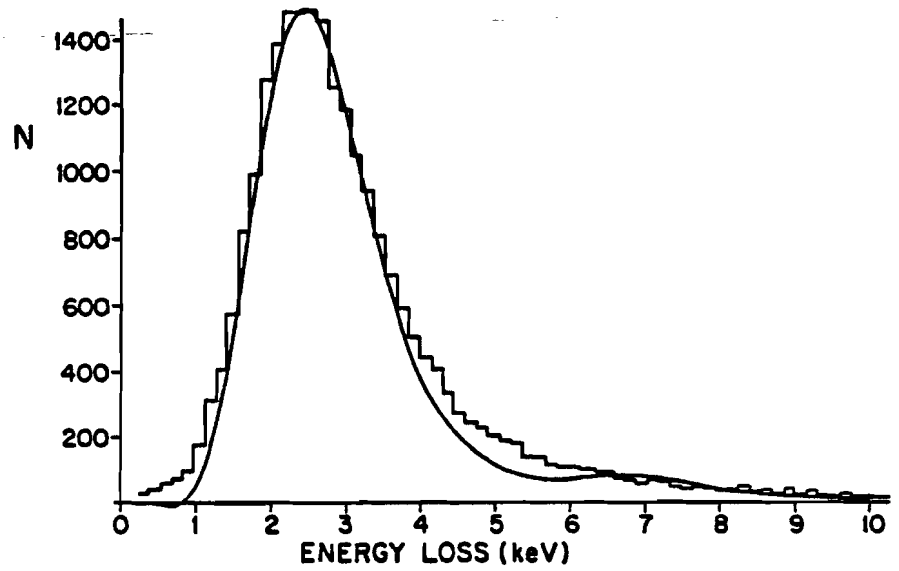

Figure C.1 Prediction of Talman's theory for the energy loss distribution resulting from 1.5 cm samples of 3 GeV/c electrons in Ar/CO_2. This is compared with measurements made by Harris, et. al. (see ref. 6).

In addition we have compared predictions with measurements of the relativistic rise. In figure C.2 we show the data of Lehraus, et. al.[7] for the ionization loss of protons, pions, and electrons for various momenta within the relativistic rise. The two experimental data sets are slightly out of agreement. A 1.2% correction has been applied to the earlier data to bring them into agreement with the later measurements. These data were taken using a mixture of 95% Ar and 5% CH_4. Plotted along with the measurements is our prediction for the ionization loss in Ar/CO_2. This curve was obtained by numerically integrating the 70% truncated mean ionization from the predicted energy loss distribution for a given momentum. Again the agreement with data is more than satisfactory.

[7] I. Lehraus, et. al., "Performance of a Large Scale Multilayer Ionization Detector and Its Use for Measurements of the Relativistic Rise in the Momentum Range of 20–110 GeV/c," NIM 153 (1978) 347.
I. Lehraus, et. al., "Particle Identification by dE/dx Sampling in High Pressure Drift Detectors," NIM 196 (1982) 361.

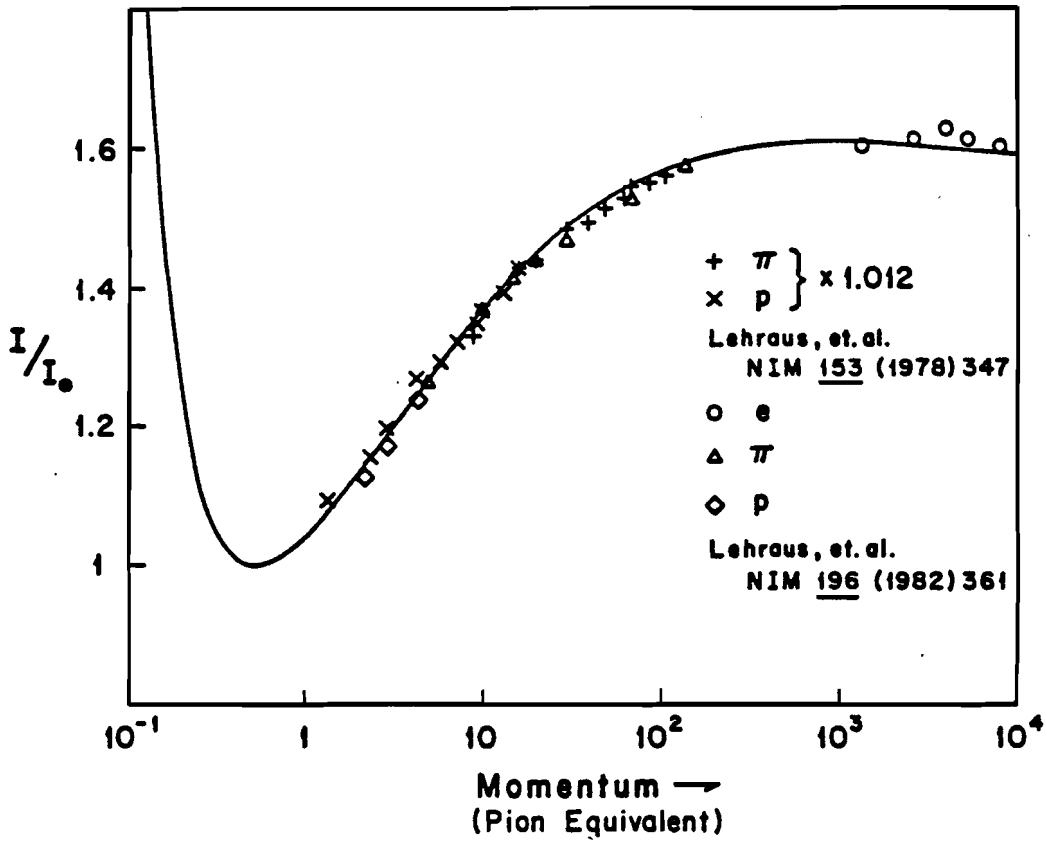

Figure C.2 The predicted relative ionization of a pion as a function of the pion's momentum. Also plotted are measurements of the ionization over most of the relativistic rise. Note that the electron and proton points are plotted at pion momenta with equivalent $\beta\gamma$.